DISSERTATION

Advanced methods in electron energy loss spectrometry and energy filtered transmission electron microscopy: Application to the Aluminium Induced Layer Exchange in Si thin film solar cells

ausgeführt zum Zwecke der Erlangung des akademischen Grades eines Doktor der technischen Naturwissenschaften unter der Leitung von

Univ. Prof. Peter Schattschneider

E138
Institut für Festkörperphysik

eingereicht an der Technischen Universität Wien
Fakultät für Physik

von

Dipl.-Ing. Michael Stöger-Pollach

[redacted]

Wien, am 15. September 2004

Acknowledgements

This work has been made possible by the support of some persons, which I want to say "Thank you" for their engagement and action. First af all I have to thank Prof. Peter Schattschneider, whose support and international scientific contacts have mainly contributed that this work has been an interesting contribution to research in the field of EELS.

A special thank is worth to Prof. Bernard Jouffrey from the Ecole Centrale de Paris for providing access to the PHILIPS CM-20 TEM and PEELS during the developement of the ELNES separation method.

I'm indebted to Prof. Henny W. Zandbergen, Sorin Lazar, Frans D. Tichelaar, Meng-Yue Wu and Tom R. de Kruijff from the National Center for High Resolution Electron Microscopy of TU Delft, The Netherlands, where I stayed for half a year during my PhD. I was allowed to use the monochromator TEM which was unique at this time. Furthermore I'm indebted to Prof. Ferdinand Hofer and Werner Grogger from FELMI, TU Graz, for using their monochromator TEM a year later for further bandgap measurements.

Moreover I have to thank Dr. Cécile Hébert from our Institute for her support and Dipl.-Ing. Sylvain Clair from the Ecole Polytechnique Federale Lausanne for many fertile discussions.

Last but not least I want to thank my wife Judit for her support during the whole PhD and her confidence within the last years. I want to thank my mother for her confidence during all my studies and also my in-laws for their support.

Now there is to mention, that this work has been supported by the project PHY14038-P of the Fond zur Förderung der wissenschaftlichen Forschung (FWF) and by METEOR of the European Commission, contract nr. ENK5-CT-2001-00543.

The investigated specimens were produced by HMI Berlin, Germany, and IMEC in Leuven, Belgium.

Finally I want to say, that this work is dedicated to my father, who has been a physicist, too, but died in Jannuary 1989.

Michael Stöger-Pollach

Summary

The present work should help to understand the physics behind the phenomenon of aluminium induced layer exchange (ALILE), a phenomenon used for growth of seeding layers for silicon thin film solar cell production. For this purpose the work contains besides a short introduction into the used analytical methods, especially transmission electron microscopy (TEM), energy filtered TEM (EFTEM) and electron energy loss spectrometry (EELS) and an overview about the principle of solar cells.

Apart from the introduction into the analytical instrumentation used, this theses consists of two main parts. The first one - including chapers 2 and 3 - deals with the improvement of the analytical methods and explorations of the physical limits in electron microscopy. The second part of this work - chapters 4 and 5 - deals with the ALILE process and the further epitaxial thickening of the seed layer. The experiences from the former chapters are used for practical investigations on micro- and nano-structures.

In part one an introduction into the ELNES separation method is given, because it was developed for investigations of chemical bondings at interfaces and surfaces and is used for determination of the oxidation states of Silicon and Aluminium at the seedlayer - membrane interface in the present work. Usually one has a superposition of energy loss signal in the detector, therefore it is essential to separate the ELNESes to get qualitative and quantitative information on chemical compositions. I present the method mathematically and experimentally for Chromium, Copper, Aluminium and Silicon. Main topic is of course the ELNES separation at the Si-membrane interface of the ALILE specimens.

Moreover I give a short outline of direct measurements of the bandgap by means of EELS, theoretically and experimentally. The experimental efforts for this part of my work are the use of a pre-specimen monochromator, that is available at the National Center for High Resolution Electron Microscopy at TU Delft, The Netherlands, and at Forschungszentrum für Elektronenmikroskopie at TU Graz, Austria. I also show that even shifts of the ionisation edge onset due to changes in bond lengths can be detected by EELS in a monochromated TEM.

The most exciting reults from the microscopists point of view are summed up in the subsection "nano analysis" where I present my EELS measurements on atomic scale.

Part two deals with the influences of variations in different parameters on the seedlayer growth. Two of them are Aluminium grain size and aluimina membrane thickness. The further epitaxial growth is also part of characterisations by means of TEM imaging, electron diffraction and electron energy loss spectrometry.

All collected experience is summed up in a model for the layer exchange process, including mathematical and experimental descriptions. The so found characteristics are discussed with respect to thin film production.

I hope that this work is an exciting contribution to EELS as well as to research on the ALILE process.

Contents

Chapter 1

Rationale

The present work is based on two research projects: "Improvement of ELNES interpretation" and on the European Solar Cell Project "METEOR". The former dealt with the development and refinement of methods for the study of the chemical and electronic structure in EELS and EFTEM whereas the latter is an ongoing project on developing a new technology for low cost production of polycrystalline silicon solar cells. The second project profited a great deal from the first one in as much as advanced methods of EELS and EFTEM were already available for the investigation of the solar cell structures. As a consequence this theses consists of two parts. This shall also be denoted in the title which is rather long due to this fact.
It took effort to separate the methodical part from the application because they are sometimes connected very strongly. The indulgent reader will understand that this goal was not always achieved.
The following methodical problems were dealt with:

1. separation of ELNES (see chapter 2.1)
2. surface contamination (see chapers 2.1.2, 2.2.3 and 2.2.4)
3. ELNES measurements on interfaces (see chapter 2.1.4)
4. ZLP subtraction (see chapters 2.2 and 2.3)
5. delocalization (see chapter 3)

These problems are discussed - and solved to a large extent - in the following. When it appears reasonable, I describe the development of the method in combination of its application to ALILE which, from a systematic point of view, rather belongs to the methodical part. This is the case for the investigations on the metal-induced gap states at the Al-Si contact.

1.1 Specifications of the Instruments used for Analysis

For optimising the Aluminium Induced Layer Exchange (ALILE) process many different analytical methods were applied. Many of them - as secondary electron microscope (SEM) and electron backscattering diffraction (EBSD) for orientation determination - were done at the Hahn Meitner Institut Berlin , Sektion 1 "Photovoltaik", Kekuléestr. 5, 12489 Berlin, Germany. But for chemical composition and spatial chemical distributions electron energy loss spectrometry (EELS) and energy filtered transmission electron microscopy (EFTEM) had to be done. This part of the analytical results was presented at some conferences [1, 2, 3, 4, 5] as papers and is summarised briefly in this thesis.

The main advantage of TEM investigations combined with EELS or EFTEM is the high spatial resolution of analysis. For example, the membrane thickness was only 2.8 - 12 nm in most cases. Questions like "is some silcon oxide formed at the Al_2O_3 membrane / Si interface ?" or "Are some glass ingredients diffusing into the seed layer ?" had to be answered.

In the following three subsections an introduction into the advantages of TEM, EELS, EFTEM and STEM are given. It is not the intention of this work to give a course for these techniques. Only the necessary details for understanding the experiments and results are given here. More detailed information can be found in technical literature.

1.1.1 TEM

For TEM investigations a FEI TECNAI F20 ST was used equipped with a field emission gun and operated at 200kV acceleration voltage. Its point resolution was proven to be better than 2.26 Å(this is the projected distance of atoms in the Si crystal in (111) orientation). Nevertheless, specimen tilting of 45° can be performed with this microscope. More detailed information about the TECNAI can be found in the internet (`http://www.feicompany.com` or `http://www.ustem.tuwien.ac.at`). The field emission gun (FEG) has a natural energy spread of approximately 0.6 eV but taking all disturbing influences into account, like electromagnetic stray fields, mechanical vibrations of the building, and lens abberations the best elastic peak in the energy loss spectrum has a full width at half maximum (FWHM) of 0.7 eV.

With this setup all kind of electron diffraction and high resolution analyses could be performed. EELS and EFTEM can be done with satisfying energy resolution for energy loss near edge structure (ELNES) and bandgap analysis (see Sections 2.1 and 2.3).

1.1.2 EELS

For detailed bandgap investigations the FEI TECNAI F20 mono of Technische Universiteit Delft (TU Delft) equipped with a pre-specimen monochromator was used. The monochromator filters out all electrons faster or slower than the selected voltage. Voltage selection can be performed by positioning the selector slit. The energy spread of the beam can be reduced in this way to 0.11 eV (without a specimen) or 0.12 eV (with specimen), respectively. More details on EELS can be found in textbooks like [6] or in diploma theses [7, 8].

1.1.3 EFTEM

Energy filtered TEM is a very comfortable technique to get elemental maps of a region of interest in the specimen. For this purpose the energy filter selects all electrons that have lost a specific energy for forming an image. For generation of elemental maps two modes can be chosen, the jump ratio method or the three window method. In both cases one gets rid of the spectral background which would falsify the image if only one acquisition at the selected energy range would be done. In the jump ratio method energy windows below and at the ionisation edge of interest are chosen and the ratio of both images is computed whereas the three windows method needs two pre-edge windows for background fitting. The extrapolated background is then subtracted from the post-edge image, as illustrated in fig. 1.1. The

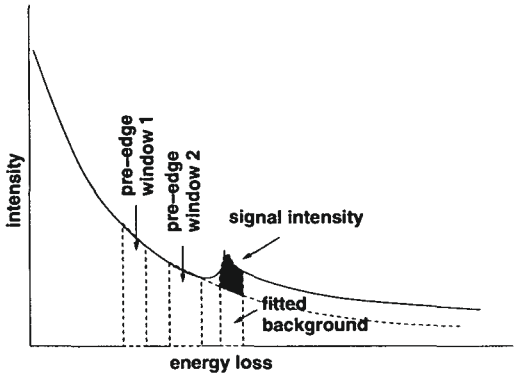

Figure 1.1: Schematic representation for the need of a background removing correction in EFTEM. The three windows for applying the three window method are plotted.

distance from the edge onset and width of the pre-edge windows depend on the chemical composition and the shape of the ionisation edge. In the ALILE case EFTEM at the Si-L edge is not trivial, because the Al-L and Si-L edge are overlapping. In energy filtered HRTEM at Al_2O_3 membrane / Si interfaces the Si map cannot be used for quantification. At positions, where no Al containing material can be detected, quantification is no problem again.
But not only elemental maps can be recorded via EFTEM. Plasmon maps can also be acquired. The advantage of plasmon maps compared to elemental maps is that in the low loss regime much more intensity is available. Therefore acquisition times can be much lower (typically 0.1 to 1 seconds). Moreover the energy window need not neccessarily be set directly into the plasmon peak. As shown in [9] better chemical contrast can be reached if the windows are set even at higher energies with respect to the EELS spectrum. On the other hand, spatial resolution is worse due to the delocalization effect, which is dependent on the energy loss and decreases with increasing losses (see chapter 3).

1.1.4 STEM

When working in STEM mode (scanning transmission electron microscope) or with a dedicated STEM such as produced by Vacuum Generators (VG) imaging is done using an annular dark field (ADF) detector or an high angle ADF (HAADF) detector. Figure 1.2 shows the principle of STEM. The electron beam is scanned across the specimen. The magnification of the image is therefore not driven

by the excitation of the objective lens of the microscope but by size of the scanned area. The smaller the scanned area is, the larger is the magnification of the image. Due to the fact that scattering

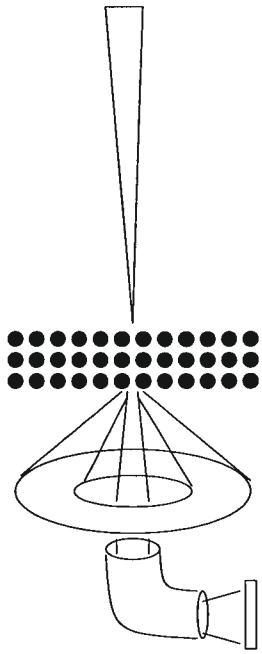

Figure 1.2: Schematic representation of the STEM. The beam is scanned across the sample. The forward scattered electrons can be used for EELS investigations whereas the high angle scattered electrons are used for imaging.

of electrons is due to Rutherford scattering, the positions of bright peaks in the HAADF image can directly be correlated to the atomic column positions. Furthermore elastic scattering is dominated by the atomic number Z. The heavier an atom, the more intense would be the HAADF signal (see for example [10]). The spatial reolution is limited by the dimension of the beam which itself is limited by the spherical abberation of the condenser lens system described by the coefficient C_s. Eq. (1.1) shows the correlation between C_s and the beam diameter d.

$$d = C_s \cdot \alpha^3 \tag{1.1}$$

With α as the convergence angle of the beam. In the TECNAI F20 $C_s = 1.2$ mm and α can be set to be 5 mrad. This gives a beam diameter of 1.5 Å.

1.2 Photovoltaics

The history of the use of solar energy is very long. The Greeks used large mirrors to bundle sunlight and set fire to Roman warships in 212 b.c. Also the Olympic Flame at the temple of Delphi was candled this way. But for power generation by using sun light it was neccessary to invent electricity first. This happened in the 17th century.

In the year 1839 Alexandre Edmond Becquerel found that batteries are more effective under illumination with solar light. 1873 the photo conductivity of Selenium was found and ten years later the first "classical" solar cell was made out of Selenium, too. But it took again ten more years until the first solar cell for power generation was produced.

The german physicist Phillip Lenard found and explained in 1894 that elecrons can be beaten out of metals by light. This effect is now-a-days well known as the photoelectric effect. Besides this he recieved the nobel prize in 1905 for his scientific work on the transmission of cathode rays through matter - the genesis of electron energy loss spectrometry.

In 1949 W. Shockley found the crystal rectifier. Therewith all requirements for solar cell production were fulfilled. But again accident helped mankind: M. Price from Bell Telephone Laboratories found with his team that rectifiers made of Silicon produce more electric power when illuminated by sunlight. Rapidly the benefit of this invention was found in a support of the telephone network on countryside which was done by batteries before.

The big breakthrough came in 1958 when the american satellite Vanguard I was the first to be equipped with solar cells. The solar cells were more effective as technicians thought but were only used for recharging accumulators on board the satellite. People were very surprised when they recieved signals from their machine for eight years instead of five years as they expected. Then the satellite got damaged by cosmic rays.

In the 70ies the efficiency of solar cells was enhanced by increase of the reflexivity in the back surface field for minority carriers and a decrease of the reflexivity for light at the solar cell surface. In the meantime the effectivity of solar cells is about 20% in laboratories and 16% in production.

But still solar energy is expensive in comparison with conventional power generation, therefore new techniques are searched for reduction of production costs. When producing high quality solar cells Silicon crystals are cut into wafers of 300 - 500 μm thickness. During sawing about 50% of very pure Silicon gets lost. Therefore one is looking for producing thin film solar cells. Less material is used but the effectivity is still not satisfying. This is because expensive substrates are needed for a good crystal growth which is neccessary for high conversion rates.

The approach for thin film solar cell production investigated in recent work, that is part of the METEOR project of the European Commission, is to put a high quality seeding layer onto a cheap substrate like window glass. The thin film solar cell can be grown onto the seeding layer afterwards.

In the folowing chapter we will discuss the principle of solar cells in detail and an introduction to the construction of ALuminium Induced Layer Exchange- (ALILE-) based solar cells is given. We will jump back to the year 1905 later on, when we discuss electron energy loss spectrometry and its efforts

for the investigations on the way to understand the ALILE process.

1.2.1 The Principle of Solar Cells

The conversion of photons into electric power is based on the inner photoelectric effect, where photons with an energy $E = h\nu$ larger that the bandgap of the semiconductor (for Silicon: $E_g = 1.12eV$) can release an electron from the valence band into the conduction band. Therefore the wavelength λ of the light must be (c_0 is the velocity of light in vacuum):

$$\lambda \geq \frac{E_g}{h \cdot c_0} \tag{1.2}$$

Therefore the spectral sensity of Si-solar cells has its maximum (with respect to its crystallinity) at 820 nm, which corresponds to red light. The generation of electron-hole pairs by means of photo absorption

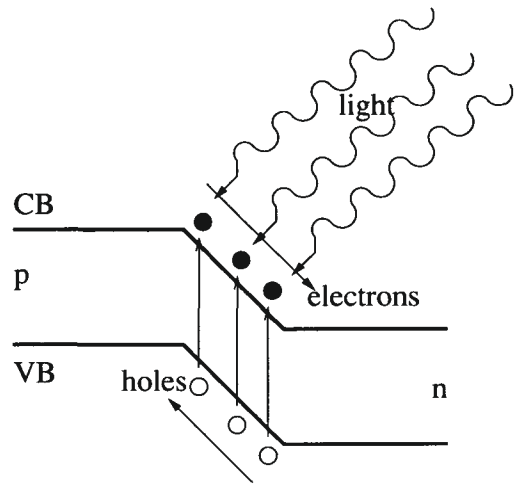

Figure 1.3: Schematic illustration of the photo effect on a pn-junction.

at a pn-junction, as it can be realized by doping of semiconductors, leads to build-up of the so called photovoltage. If the electric circuit is closed a photocurrent appears. Figure 1.3 shows a schematic representation of all events at the junction. Even the minority carriers generated less than a diffusion length away from the junction contribute to the current.

Under illumination conditions an additional current I_L is generated at a pn-junction if the electric circuit is opend. This leads to a build-up of the photovoltage U_p in such a way that we can write

$$I_L = I_0 \cdot (e^{\frac{eU_p}{kT}} - 1) \tag{1.3}$$

and

$$U_p = \frac{k \cdot T}{e} ln(1 + \frac{I_L}{I_0}) \tag{1.4}$$

where I_0 is the whole current, i.e. the sum of all generation currents flowing without illumination (a material and temperature dependent constant). For solar cells the effective voltage U_{eff} is reduced by

the bulkresistance R_S of Silicon. We find

$$U_{eff} = U_p - R_S \cdot I_{eff}. \tag{1.5}$$

A reduction of R_S would increase the effective output of solar cells. This can be achived by a reduction of the solar cell thickness, which impliss the production of thin film solar cells. Widely commercial are amorphous Silicon solar cells but their efficiency is below 7% and decreases with aging due to the fact that hydrogen, which is incorporated in amorphous Si during the production process, diffuses out of the Silicon and leads to a degradation of the solar cell. Dangling bonds are left behind after hydrogen escape that trap electrons. Therefore crystalline structures are essential even for thin film solar cells. In figure 1.4 the theoretical efficiency of several crystalline materials under bright sunlight illumination is given. A high efficiency for conversion requires a compromise between high photo voltage (that

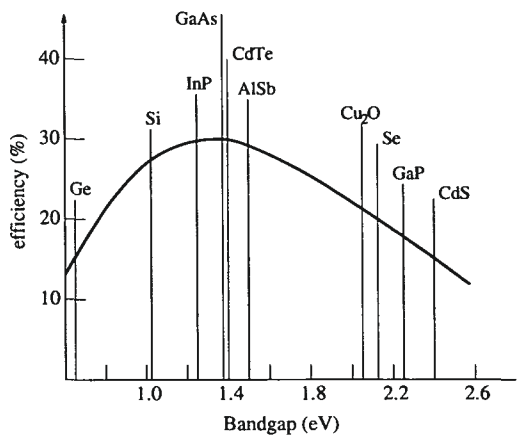

Figure 1.4: Theoretical kurve of conversion efficiencies for a 1.7 cm^2 solar cells in bright sunlight as a function of bandgaps.

means large bandgaps) and high photo current which is correlated to good absorption over a large spectral range (that means small bandgaps). The maximum of sunlight is at 2.5 eV, so a bandgap of half this value gives the optimum width (1.0 - 1.5 eV). Si and GaAs are in this region and efficiencies of 16% are reached in production with these materials [11].

1.2.2 Thin Film Solar Cells

Thin film silicon solar cells seem to be the way out of an eventual power shortage of the future world. In the previous two sections the advantages like low material loss and a reduction of the bulk resistance have been mentioned. Silicon thin film solar cells have many more advantages compared to products using other materials. Silicon is non-toxic and the most abundant element on the earth's crust [12]. Until recently, it was believed that crystalline silicon (c-Si) solar cells ought to be at least 10 μm in thickness to achieve reasonable efficiencies (> 10%) due to the fact that c-Si is an indirect semiconductor with weak light absorption [13]. But clever light trapping schemes open the way to thinner films and still maintain high efficiencies [14]. Efficiencies as high as 10.1% have been reported for 2.0 μm thick microcrystalline Si solar cells [15].

The main obstacle that hampers the development of crystalline silicon solar cells is the difficulty of producing crystalline silicon layers onto foreign substrates. To reach efficiencies in the range of 15% large grained polycrystalline (pc) silicon films seem to be mandatory [16]. The deposition of silicon on foreign substrates is most commonly performed by chemical vapour deposition (CVD) techniques. However, these types of deposition directly onto amorphous substrates (like glass) leads to polycrystalline films with grain sizes in the range of some tens of nanometers [8, 16].

The growth of monocrystalline silicon films can be achieved on silicon wafers, detached after growth and attached to any other substrate. This can be done because the wafer/film interface is either oxidized or porous. Even if the material loss is reduced this way - the wafer can be used many times - the technique is very expensive and cost reduction therefore very small.

Instead of depositing crystalline silicon directly onto the amorphous substrate, research has recently focussed on seed layer growth, which is one topic of the METEOR-project. This can be obtaind by deposition of amorphous Si with subsequent recrystallisation. Here again several possibilities are available: laser induced recrystallisation or metal induced recrystallisation. In this work only specimens using metal induced recrystallisation were investigated. Furthermore this type of seed layer growth can be subdivided into two categories: high and low temperature crystallisation. The process temperature dictates what kind of substrate can be used and influence the substrate cost predominantly.

The METEOR project aims at the development of fast and simple film formation techniques which can deliver thin crystalline Si layers with sufficient structural and electronic quality. A two step process is used in which a large-grained seed layer is created by metal-induced crystallization which subsequently serves as template for an epitaxial growth process. By combining a potentially fast process and an inexpensive substrate it is hoped that this approach will deliver a scheme to produce efficient, low cost crystalline silicon thin-film solar cells with a cost potentially below 1 Euro/Watt.

1.2.3 The Aluminium Induced Layer Exchange Process (ALILE)

When the metal induced (re)crystallisation is the method of choice, several metals can be taken into account. Aluminium seems to be the most attractive one due to the fact that no Aluminium-Silicide can be formed. Other materials used for metal induced crystallisation (MIC) are Antimony (Sb) and Bismuth (Bi) [17]. The presented studies deal only with systems using Al.

The principle for the MIC process is very simple. A polycrystalline Al thin film is deposited onto a glass substrate. Al grows polycrystalline under room temperature conditions. No special efforts are needed for this step under vacuum conditions. After depositing a few dozens of nanometers of Al, the reactor is vented and the thin film is oxidized for a few minutes forming a thin membrane of Al_2O_3. Afterwards the reactor is re-evacuated and a Si thin film is deposited. This film is usually amorphous. However, when heating the system, the Al and Si layers change place leaving the Al_2O_3 membrane stable, as shown in Fig. 1.5. The amorphous Al_2O_3 membrane crystallizes during the heat treatment but it seems that this does not influence the layer exchange. The influence of the membrane is discussed in detail in section 5.1.2. After tempering the layer system can be found as illustrated in Fig. 1.6. The ALILE process has the great advantage that the seed layer is automatically Al-doped. No extra doping is needed. The main disadvantage is that the polycrystalline structure is containing crystals of

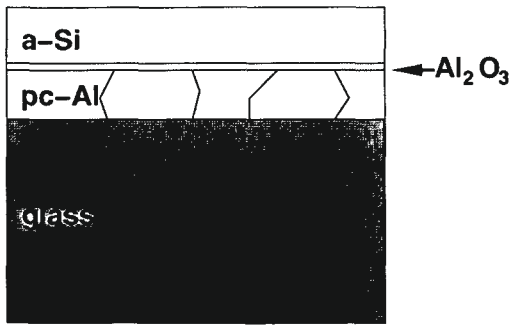

Figure 1.5: Layer system as deposited. The thickness ratio of the Al and Si layer is of utmost significance.

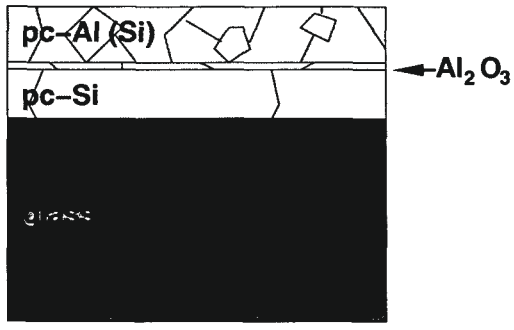

Figure 1.6: After heat treatment the Al and Si layers change their places. The Al_2O_3 membrane keeps stable but crystallizes.

different orientations.

The next step of solar cell production is to remove the polycrystalline (pc)-Al(Si) layer by etching. Depending on the etch, the Al_2O_3 membrane is removed, too. Then the Si islands are removed by using a chemical-mechanical-polishing (CMP) routine. This step is followed depositing a thick Si layer using plasma enhanced chemical vapor deposition (PE CVD). Detailed investigation of the PE CVD grown layer is given in section 5.2.

After thickening an amorphous Phosphorous doped Si layer is deposited capped by a ZnO layer and Al contacts. The ZnO is a conducting transparent oxide and is used as a diffusion barrier to prevent the Si layer to get doped with Al, too, from the contact side. Otherwise the efficiency would be reduced enormously.

Chapter 2

Advanced Methods

2.1 ELNES Separation for surface layers and on interfaces

In this section, a method to separate surface from volume contributions in the fine structure of ionization edges in electron energy loss spectrometry (EELS) is discussed. It is based on spectra taken at two positions with different surface-to-volume ratios. Contrary to the similar spatial difference method [18] it uses well defined scaling factors, allowing an estimate of the errors propagated into the result.

2.1.1 Information limits in ELNES separation method

The question of how to remove surface related contributions from an energy loss spectrum has recently attracted considerable interest in the context of energy loss near edge structure (ELNES). Owning to the fact that the fine structure of ionization edges depend on the chemical environment of the ionized atom surface layers such as oxides, amorphous damage layers or adsorbates may distort the ELNES. In order to suppress double scattering (which would change the ELNES) very thin specimens with a thickness of 0.3 to 0.5 mean free paths for inelastic scattering are regularly used. Thus amorphous or oxidic suface layers may contribute considerably to the signal. In view of this fact a method to remove this contribution is of paramount importance. It should be noted here that a related problem, namely the removal of the bulk contribution is a subject of current debate (e. g. [19]) in the context of extracting faint signals of an interface by the spatial difference method [20, 21, 22, 18, 23].

The intuitive method commences with two spectra with different surface/bulk atomic ratio. Since the spectral intensity is proportional to the respective number of atoms illuminated by the beam, measuring this ratio in two regions (e.g. by chemical microanalysis of oxygen for an oxide layer) allows to scale the two spectra to the same surface layer thickness and subtract one from the other in order to remove the surface layer contribution *a posteriori*. As will be shown below, this intuitive reasoning is correct only in the limit of infinitely thin specimens.

In the following, the different inelastic interactions (background or ELNES of the bulk or the surface) giving rise to the measured spectrum are discussed. It is found that the surface contribution to the

ELNES may in fact be removed under quite general conditions, by use of proper scaling factors for the subtraction of spectra.

When a beam of fast electrons traverses a specimen of thickness d and interacts only inelastically (which means, it travels alon a straight line path) the energy loss spectrum of the probe electrons is a weighted superposition of n- fold scattering probability distributions[24]:

$$p(E) = e^{-d/\lambda} \sum_{n=0}^{\infty} \frac{(d/\lambda)^n}{n!} f^{(n)}$$

where $f^{(n)}$ is the n-fold convolution of the normalized single scattering probability $f(E)$ ($\int f(E)dE = 1$). λ is the inelastic mean free path (MFP) of the probe electrons. Observing that the Fourier transform of the n-fold self-convolution of a function $f(E)$ is the n-th power of its Fourier transform $\tilde{f}(t)$ eq. 1 can be written

$$\tilde{p}(t) = \sum_{n=0}^{\infty} e^{-d/\lambda} \frac{(d/\lambda)^n}{n!} [\tilde{f}(t)]^n = e^{d/\lambda(\tilde{f}(t)-1)}. \tag{2.1}$$

What is the meaning of the dimensionless quantity d/λ? Since $\lambda = 1/n\sigma$, with n the number density of scattering centres and σ the average cross section of the inelastic processes, we find

$$d/\lambda = \hat{N}\sigma = N \tag{2.2}$$

where $\hat{N}$ is the surface projected number of scattering centres per unit surface area, and N is a pure number, signifying the number of scattering centres within the area σ.

Eq. 2.1 is valid irrespective of the nature of the scattering process. It follows that we can replace all m *physically* distinct processes occurring in a specimen (such as plasmon, intra- or interband excitations, or ionizations) by a single *average* inelastic process. It can be shown [25, 26] that for this average process

$$\begin{aligned} N &= \textstyle\sum_{j=1}^{m} N_j \\ f &= \frac{\sum_{j=1}^{N} N_j f_j}{N} \end{aligned} \tag{2.3}$$

This can be understood by observing that the total scattering probability is the convolution of the probabilities related to the separate processes, hence its Fourier transform is

$$\tilde{p}(t) = \prod_j e^{N_j(\tilde{f}_j - 1)} = e^{\sum N_j(\tilde{f}_j - 1)}. \tag{2.4}$$

It should be noted that the position in the specimen where the j-th process takes place is irrelevant. (Formally this is because the convolution of functions is commutative). Thus the specimen can be homogeneous or inhomogeneous (e.g. consisting of sandwiched layers or showing surface contamination) with a variety of inelastic processes acting.

We aim at a particular ionization edge (and its ELNES) given by N_i. All other inelastic processes are considered as background given by N_b. Eq. 2.4, separated into background and ionization processes is now

$$\tilde{p}(t) = e^{N_b(\tilde{f}_b - 1)} e^{N_i(\tilde{f}_i - 1)}. \tag{2.5}$$

Since in general $N_b = d/\lambda_b < 1$ and $p(E) \propto E^{-r}$ with r between 2 and 6, taking the plasmon loss as the dominant background loss and an ionization edge at several 100 eV, $N_b/N_i \approx 10^r$, it follows that $N_i << 1$. Therefore, the second exponential in eq. 2.5 can safely be linearized

$$\tilde{p}(t) \doteq e^{-N}(\underbrace{e^{N_b \tilde{f}_b}}_{\text{background } p_b} + e^{N_b \tilde{f}_b} N_i \tilde{f}_i). \tag{2.6}$$

The first term is the background, including the low loss. The single scattering distribution for ionization is obtained from Eq. 2.6 as

$$N_i \tilde{f}_i = \frac{\tilde{p} \cdot e^N - \tilde{p}_b}{\tilde{p}_b} := \tilde{p}^{(1)} e^N. \tag{2.7}$$

After Fourier transform, this amounts to 1) scaling the total scattering probability to e^N; 2) subtracting the background beyond the edge; and 3) deconvolving with the low-loss. (When the EL/P software is used, background subtraction and subsequent Fourier-ratio deconvolution yields

$$\begin{aligned} I_0 p^{(1)} &= I_0(p - p_b - p_{plural}) = \\ &= I_0 e^{-N}(N_i f_i + \underbrace{N_i^2 f_i^{(2)}/2 + N_i^3 f_i^{(3)}/6 + ...}_{plural scatt.} - p_{plural}) \\ &= I_0 e^{-N} N_i f_i \end{aligned} \tag{2.8}$$

which is, apart of the exponential and the normalizing factor I_0, the correct result. Thus, using EL/P, one needs only to multiply the result with e^N).

We note in passing that Eq. 2.7 reduces to the intuitive approach in the limit of small N, i. e. infinitely thin specimens.

The left hand side of Eq. 2.7 can be replaced, according to Eq. 2.3, by the sum over surface and volume contributions

$$N_s f_s + N_v f_v = p^{(1)} e^N. \tag{2.9}$$

This is the basic equation relating the unknown ELNES f_s of the surface layer and f_v of the volume ("bulk") to the experiment $p^{(1)}$. Note that it is important to multiply the measured edges with the factor e^N. The intuitive approach would have neglected the exponential factor. Experimentally, the Ns are between 0.2 and 0.8. Neglect of the exponential factors can change the scaling factor by more than 50 % [27].

Let us briefly consider what is going on here. f and p are functions of energy; N's are pure numbers denoting how much of the surface and volume contribute. To solve for the unknowns $N_{sA,B}$ and $N_{vA,B}$ measured at the positions A and B, we seem to need two equations of type 2.9 with four known Ns. Taking advantage of the fact that the functions f are normalized to one, the unknowns may be defined as

$$\mathbf{x} = \begin{pmatrix} x_1 \\ x_2 \end{pmatrix} := \begin{pmatrix} N_{sA} f_s \\ N_{vA} f_v \end{pmatrix}. \tag{2.10}$$

For later use, we define the matrix $\mathbf{A}$

$$\mathbf{A} := \begin{pmatrix} 1 & 1 \\ s & v \end{pmatrix}$$

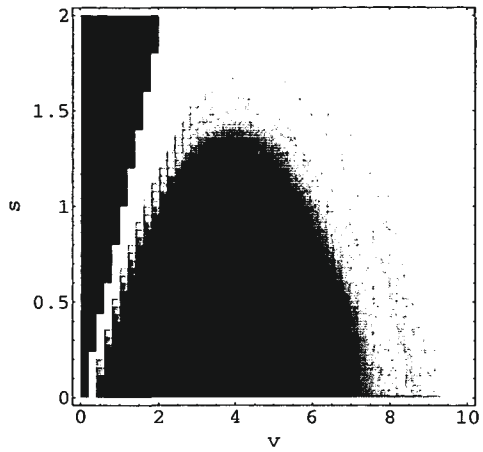

Figure 2.1: Condition number of the matrix $\mathbf{A}$ as a function of v and s ($v > s$) for a realistic range of parameters. Darker colors denote lower values. The optimum bulk ratio v is between 2 and 5.

with $s = N_{\mathrm{sB}}/N_{\mathrm{sA}}$ and $v = N_{\mathrm{vB}}/N_{\mathrm{vA}}$ the ratios of the surface and volume contributions at two positions A and B in the specimen. The system of the two linear equations $\mathbf{A} \cdot \mathbf{x} = \mathbf{c}$ can be solved if and only if the determinant of the matrix of coefficients does not vanish. i. e. $s \neq v$ or, likewise, the surface to volume ratio at the two positions must be different.

Instead of the four numbers N only the two ratios ($N_{\mathrm{sA}}/N_{\mathrm{sB}}$ and $N_{\mathrm{vA}}/N_{\mathrm{vB}}$) need to be known.

The advantage of this formulation is that the ratio is independent of the inelastic scattering cross sections. Any errors in σ disappear in the ratio. Once x_1, x_2 are determined, the Ns and the single scattering functions $f_{\mathrm{s,v}}$ can be obtained from the normalization condition. Furthermore we have from Eq. 2.9

$$N_{\mathrm{s}} + N_{\mathrm{v}} = \int_{E_i}^{E_i+\Delta E} p^{(1)}(E) dE e^{N}.$$

This is an interesting side result: the energy integral of the measured single scattering probability for ionization multiplied with e^N is the number of ionized atoms in the specimen projecting onto an area of σ.[1]

The occurrence of the inverse matrix $\mathbf{A^{-1}}$ on the solution may amplify the stochastic or systematic errors especially when the matrix is ill-conditioned. An estimate for the induced error is

$$\frac{\|\mathbf{dx}\|}{\|\mathbf{x}\|} \leq \mathrm{cond}(\mathbf{A}) \left(\frac{\|\mathbf{dc}\|}{\|\mathbf{c}\|} + \frac{\|\mathbf{dA}\|}{\|\mathbf{A}\|} \right) \tag{2.11}$$

where $\|\ldots\|$ is any norm defined in the same sense for vectors and matrices. The condition number $\mathrm{cond}(\mathbf{A})$ is the ratio of the largest to the smallest singular value of the matrix. (When the matrix is singular, this ratio diverges.) From a general point of view, the optimum values for s, v are those minimizing *cond*$(\mathbf{A})$. A simple calculation shows that they are in the range 0.5 to 2.

[1] The σs for surface and volume scattering are almost equal for reasonable integration windows ΔE.

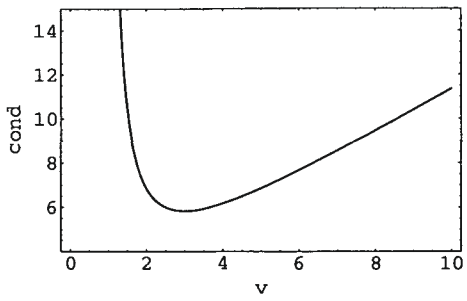

Figure 2.2: Condition number of the matrix as a function of v for $s = 1$. Best results are obtained for $v \approx 3$ with an upper limit for error amplification of cond($\mathbf{A}$)=5.8

In practice, it is recommended to simulate the errors directly in order to obtain more realistic values for the upper limit. In doing so, we use standard deviations (rms values) for the errors dc_1, dc_2 in the measured spectra and ds, dv in the matrix elements, induced by quantification, drift, intensity variations of the incident beam, and the like. The resulting standard deviation is a function of the input errors, of the spectra c_1, c_2 and of the matrix elements s, v.

$$\begin{aligned} \frac{dx_1}{x_1} &\leq \frac{1}{|c_2 - v\,c_1|}\sqrt{v^2\,dc_1^2 + dc_2^2 + \frac{(c_2 - v\,c_1)^2 ds^2 + (c_2 - s\,c_1)^2\,dv^2}{(s-v)^2}} \\ \frac{dx_2}{x_2} &\leq \frac{1}{|c_2 - s\,c_1|}\sqrt{s^2\,dc_1^2 + dc_2^2 + \frac{(c_2 - v\,c_1)^2\,ds^2 + (c_2 - s\,c_1)^2 dv^2}{(s-v)^2}} \end{aligned} \tag{2.12}$$

Eq.2.12 allows to simulate realistic situations. In the following, we assume $s = 1$, amounting to a constant surface layer thickness, see later. Fig.2.3 shows the error amplification factor, i. e. the increase in the relative error of the result with respect to the original spectra, as a function of v. We set $N_{vA} = 0.5\,N_{sA}$ and $ds/s = dv/v$. The parameter is ds/s, ranging from 1 to 20 %. The error amplification tends to a limit of ca. 3 for the volume contribution. This result indicates that Eq.2.11 overestimates the errors in the result. When the ratios s, v are reasonably chosen, the error in the result is amplified by a factor of 3-5.

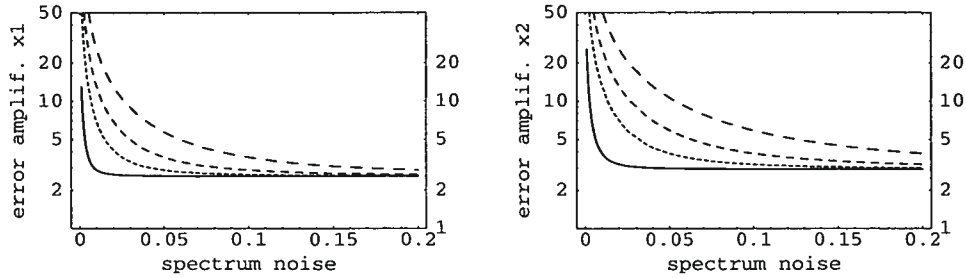

Figure 2.4: Error amplification for the surface (left) and the volume spectrum (right) as a function of the noise in the experimental spectra, $dc_1/c_1 = dc_2/c_2$. The parameter is the relative error in the matrix element $ds/s = dv/v = 0.01,\ 0.05,\ 0.1,\ 0.2$. $N_{vA} = 0.5\, N_{sA}$ and $s = 1$, $v = 3$.

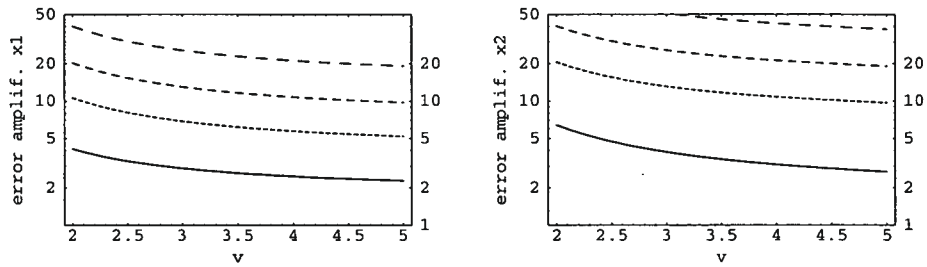

Figure 2.3: Error amplification for the surface (left) and the volume spectrum (right) as a function of the matrix element v. The parameter is the relative error in the matrix element $ds/s = dv/v = 0.01,\ 0.05,\ 0.1,\ 0.2$. $N_{vA} = 0.5\, N_{sA}$ and $s = 1$.

Fig.2.4 shows the asymptotic behaviour more clearly. Here we plot the amplification factor as a function of the relative error $dc_1/c_1 = dc_2/c_2$ in the measured spectra, for the same parameters as before. The optimum value is approached when $dc_1/c_1 \approx dv/v$, suggesting that it does not make sense to push the noise in the spectra to lesser values than the uncertainty in the matrix elements v, s.

When we set the same upper limits dN/N to the quantification results at the two positions, a little algebra shows that

$$\frac{ds}{s} = \sqrt{2}\,\frac{dN_s}{N_s}, \qquad \frac{dv}{v} = \sqrt{2}\,\frac{dN_v}{N_v} \tag{2.13}$$

The table shows the final relative noise in the volume spectrum for a range of input spectrum noise dc_1/c_1 and quantification noise dN/N. Parameters were $s = 1$, $v = 3$, $N_{vA} = 0.5\, N_{vB}$. When we restrict the acceptable final noise to 15 % we need to have less than 5 % noise in the experiment and 1 % in the quantification, or 1 % in the experiment and 4 % in the quantification. Errors surpassing these critical values render the spatial difference method unreliable.

Removal of surface induced contributions from ELNES is feasible by linear combination of two experimental spectra, under not very stringent conditions. Knowledge of the exponential factors and of

dc/c	0.01	0.03	0.05	0.07	0.09
0.01	0.05	0.09	0.15	0.21	0.26
0.02	0.08	0.11	0.16	0.22	0.27
0.03	0.11	0.14	0.18	0.23	0.28
0.04	0.15	0.17	0.21	0.25	0.3
0.05	0.18	0.2	0.23	0.27	0.32

Table 2.1: Final rms noise in the volume spectrum for input errors dc/c (horizontal entry) and dN/N (vertical) in the relative quantification. Parameters are $s = 1$, $v = 3$, $N_{vA} = 0.5\, N_{vB}$.

the ratio of surface contribution at two positions allows to explicitely calculate the bulk ELNES, thus circumventing the problems with uncertainties in the scaling factors inherent in the spatial difference method [28]. The errors propagated into the result remain below $\approx 15\%$ when the ratios s and v are well chosen, and the sum of the input errors (noise in the spectra and uncertainty in quantification) is below $\approx 6\%$.

Application of the method to EXELFS appears feasible although the surface poses a less serious problem there since thicker specimens can be used. Several extensions can be envisaged: The measured ELNES need not stem from the bulk and the surface; a combination of fine structure from a mixture of two phases can likewise be disentangled. A typical case would be a precipitate completely embedded in the matrix. Furthermore, the method may be extended to more unknowns. It remains to be seen if and when the system of equations remains sufficiently well conditioned. It is also tempting to adapt the approach to the spatial difference method applied for extraction of interface signals in the edge-on geometry.

2.1.2 Results of ELNES separation on Cu and Cr

When applying the "difference spectrum method" to our task, scaling factors F_v and F_s must be calculated as described in [29] for the extraction of volume and surface signal, respectively. These scaling factors normalize the EEL spectrum to the intensity of the ionisation edge of the influencing material, which was oxygen in the metals and aluminium in the intermetallic alloy, respectively. All data needed are calculated by the EL/P program. Building on Eq. 14 in [29] with respect to

$$p_\mathrm{A}^{(1)}(E) - F_\mathrm{v} \cdot p_\mathrm{B}^{(1)}(E) = c_\mathrm{v}\, f_\mathrm{v}(E) \tag{2.14}$$

where $p_\mathrm{A,B}^{(1)}(E)$ are the measured ELNES spectra after multiple scattering deconvolution, as e.g. done by the EL/P software. The left hand side of Eq. 2.14 is the ELNES f_v of the bulk atoms with the normalisation factor

$$c_\mathrm{v} = \left(N_\mathrm{vA} - \frac{1}{s} N_\mathrm{vB} \right) e^{-N_\mathrm{A}}$$

containing the ratio $1/s = N_\mathrm{sA}/N_\mathrm{sB}$, which need not be calculated explicitely since defined by [29], $\int f_\mathrm{v}(E)\, dE = 0$. The scaling factor F_v is

$$F_\mathrm{v} = \frac{1}{s} e^{N_\mathrm{B} - N_\mathrm{A}} = \frac{N_\mathrm{sA}}{N_\mathrm{sB}} \frac{e^{d_\mathrm{B}/\lambda_\mathrm{B}}}{e^{d_\mathrm{A}/\lambda_\mathrm{A}}} = \frac{I_\mathrm{A}^{Ox}(d_A)}{I_\mathrm{B}^{Ox}(d_B)}. \tag{2.15}$$

$N_{sA,B}$ and $N_{vA,B}$ are the numbers of scatterers of the surface and bulk layers which also represent their thicknesses at the positions of measurement A and B, d is the thickness, λ is the inelastic MFP, and $I^{Ox}(d)$ is the intensity in the oxygen edge. When separating the ELNES of an oxidic surface layer, the intensities in the O-K edges can be taken for the calculation of the scaling factor[2], as shown in Eq. 2.15. One can assume, that the ratio of oxidized atoms in both positions is the same as the ratio of the oxygen atoms themselves.
The right hand side of Eq. 2.14 contains only the bulk signal depending on f_v, N_{vA}, and N_{vB} which are only bulk contributions. f_v is the single scattering probability for the bulk material, N_{vA}, and N_{vB} are the numbers of scatterers of the bulk layer.
In the calculation of the scaling factors F_s for the ELNES extraction of the oxidized atoms, N_{sA} and N_{sB} must be replaced by N_{vA} and N_{vB}.

$$F_s = \frac{N_{vA}}{N_{vB}} e^{N_B - N_A} \tag{2.16}$$

N_{vA}/N_{vB} can be calculated from quantification results provided by the EL/P program and the information of the stoichiometry of the surface oxide. In general, the first few monolayers of the surface oxide won't be stoichiometric and therefore a small error is introduced into this technique. $e^{N_B - N_A}$ is the thickness correction factor which only depends on the total thicknesses and therefore is not altered when calculating F_s. This thickness correction factor is explained in detail in section three.

The accuracy of this technique can by tested either by comparison of the separated ELNES with band-structure calculations or by applying this method not only to the ELNES signal but to the whole EEL spectrum. In the second case a quantification of a spectrum calculated in this way gives pure bulk material or the assumed composition of the oxide. [3]

Neglect of the thickness correctrion factor of eq. 2.15 in difference spectrum techniques has often led to large errors in the scaling factors. An explicit discussion can be found in Schattschneider *et al.* [29]. In this paper we only want to present the importance of the thickness correction by means of a quantitative analysis of some features of the ELNES. The importance of the specimen thickness to the signal in the EEL spectrum is not only because of its influence on the signal background and plural scattering but it has a bearing on the intensity of the ionisation edge itself [6]:

$$I(d) = N \cdot \sigma \cdot I_0 \cdot e^{-d/\lambda} \tag{2.17}$$

I(d) is the intensity of the ionisation edge in a specimen of thickness d, N is the number of detected atoms/nm^2 corresponding to the ionisation edge, σ is the inelastic cross section, I_0 is the total incoming intensity, and λ is the inelastic mean free path (MFP). For a demonstration we neglect the influence of the thickness and calculate the uncorrected scaling factor F_u

$$F_u = \frac{N_{sA}}{N_{sB}} \tag{2.18}$$

which represents a scaling only with respect to the thicknesses of the oxide layers in A and B but not taking into account the total specimen thickness. When neglecting the thickness correction factor the

[2]Usually one never has exactly the same total incoming intensities during two measurements. Therfore the spectra should be divided by the total incoming intensity before any further treatment.

[3]Such a spectrum corresponds to a specimen thickness without any physical significance. This virtual thickness of difference spectra has been explicitly discussed in [30].

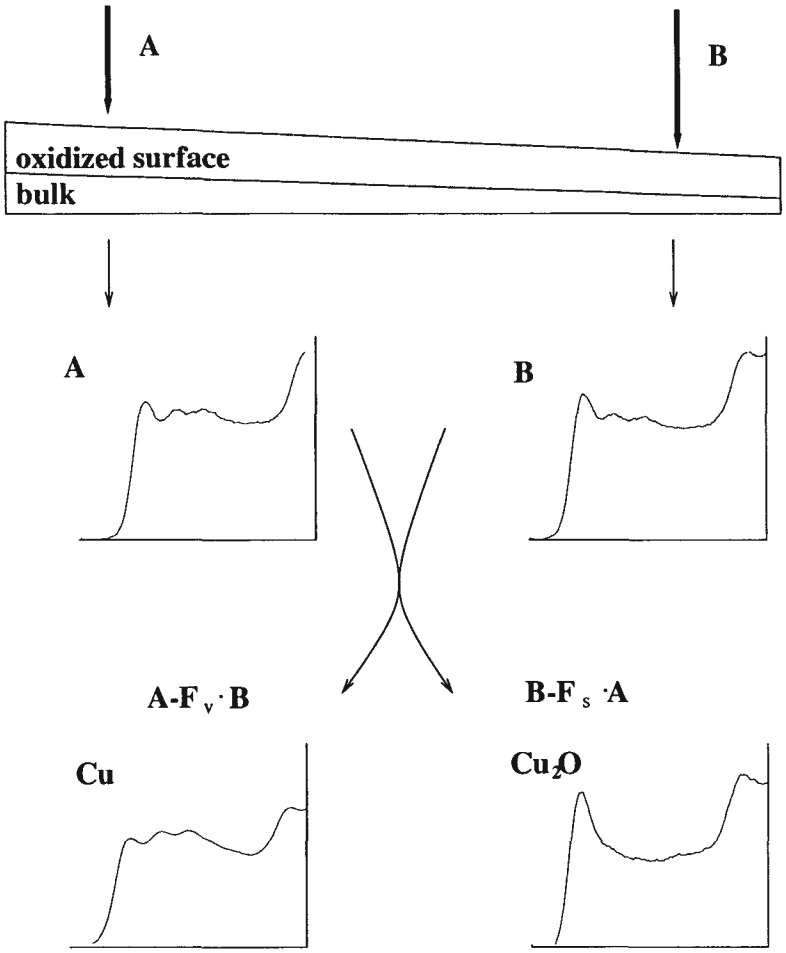

Figure 2.5: Schematic representation of the ELNES seperation of pure "bulk signal" and oxidized "surface signal" in the Cu-L3 edge. Spectra A and B contain both, surface and bulk signal, with different proportions. F_v and F_s can directly be calculated from quantification data of the EL/P programme.

error obviously depends on the difference between the thicknesses in A and B (in units of MFP). This means, the larger the thickness difference the bigger is the error. This is demonstrated in fig. 2.6 for the Cu-L_3 edge.

As described in [22] difference methods are very sensitive to the scaling factors. Even in our simpler case a bad choice of the scaling factor has an enormous influence on the signal. The difference spectrum taken from two positions with a thickness difference of 0.136 MFP gives an error of 13 % to the scaling factor. The other difference spectrum with 0.319 MFP thickness variation induces an error to the scaling factor of 28 %. The consequence is a weak "energy shift" of the first fine structure feature which is extremly sensitive because of the rapid increase at the ionisation edge onset. The height of the first feature is also wrong (Fig. 2.6). Only the correct scaling factor gives a unique result for all cases. In this context we note that one has to be cautious when comparing band structure

calculations with experiments as the case of Cu shows [31]. The core-hole strength can be "tuned" so as to obtain various spectra, even wrong ones. Due to the fact that there can't be any correspondence between specimen thickness and core-hole effect, this can be seen as a further proof that neglect of the thickness correction factor is not justified.

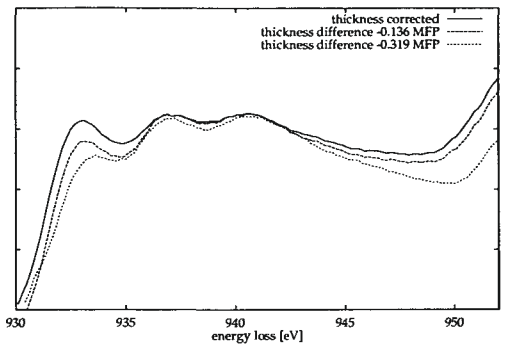

Figure 2.6: Dependence of the fine structure in the Cu-L_3 edge on the scaling factor. The influence of the thickness correction on the scaling factor is 13 % and 28 %, respectivly, due to neglect of the exponential factor s. The upper spectrum is the correct one. The larger the error, the lower the first feature and the threshold energy of the ionisation edge. Steep rises and sharp features are very sensitive to the scaling factor.

When the thickness varies within the illuminated area, the deconvolution procedure still works approximately. The integral over the collected spectrum $p(x)$ normalized by the area F in Fourier representation can be written as

$$\frac{1}{F}\int \tilde{p}(x)\,dF = \frac{1}{F}e^{\bar{N}(\tilde{f}-1)}\cdot\int e^{\delta N(x)(\tilde{f}-1)}\,dF \tag{2.19}$$

with $\delta N(x) = N(x) - \bar{N}$.
$\bar{N}$ is the mean value of $N(x)$ within the illuminated area of the specimen with varying thickness. The integral is of order $O(\delta N^2)$, hence a thickness variation of $\pm$ 5 % causes errors of $\approx$ 0.2 % in the deconvoluted ELNES. This general problem in EELS has no influence on the scaling factor.

Copper and Copper Oxide

Two copper specimens were produced in the same way as Al. One of them was oxidized at 150°C for 1.5 hours in wet atmosphere, the other one was exposed to air at room temperature for 15 minutes. For accurate investigations ELNES separation was not only done with the positions A and B on one specimen only, but the spectra from both specimens were combined, too. This is possible when investigations are done with the same experimental conditions. The results were compared with *ab initio* bandstucture calculations done by means of the WIEN97 code [32]. Some copper spectra are presented in Fig. 2.5, but more detailed information is given in Fig. 2.7. When comparing the separated ELNES of pure bulk copper with 0.5 core-hole simulations [31] one immediately sees good correspondence of the measured and simulated spectra.

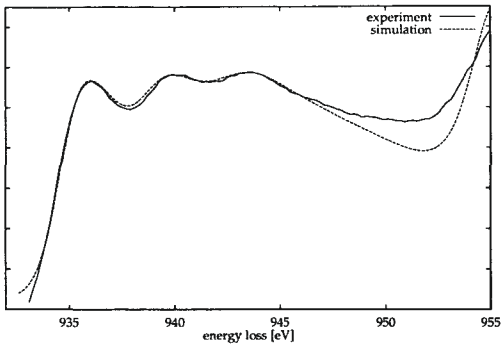

Figure 2.7: Intensity (arb.u.) vs. energy loss for Cu. Separated Cu-L_3 edge (full line) compared with a band structure simulation (dashed line) supposing half a core hole [31]. The simulation was broadened with the spectrometer resolution (1.8 eV FWHM in the zero-loss peak) to get a realistic comparison between simulation and experiment.

Chromium and Chromium Oxide

The ELNES separation method was proved on chromium, too, because the white lines of Cr_2O_3 have many fine structure features. In figure 2.8 spectra acquired with the monochromator TEM of TU Delft are shown. For comparison a spectrum of the Cr-$L_{2,3}$ edge of Cr_2O_3 is added. The separated spectrum of the oxide layer reproduces the fine structure quite well, even if the signal-to-noise ratio is not excellent. All fine structure peaks (1-4 in fig. 2.8) can be observed.

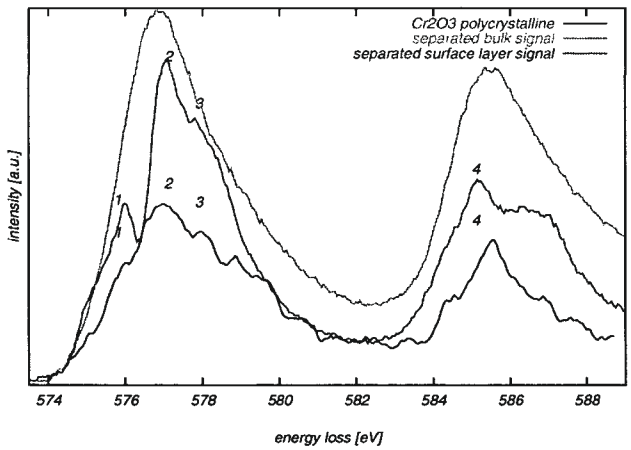

Figure 2.8: Intensity (arb.u.) vs. energy loss for Cr. Separated Cr-$L_{2,3}$ edges of a polycrystalline Cr_2O_3 specimen acquired with the monochromator TECNAI of TU Delft, and the separated spectra from an oxidized polycrystalline chromium specimen.

Another experimental proof for ELNES separation is shown in figure 2.9. Here two spectra of the Cr-L edge from positions with the same oxygen-to-chromium ratio of an oxidized chromium specimen are compared. ELNES separation is leading to noise in this case.

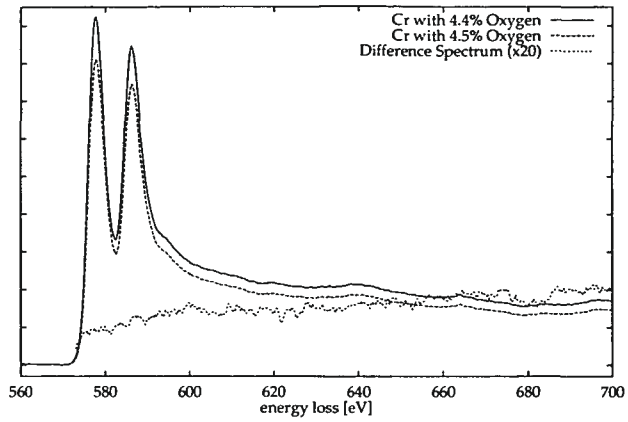

Figure 2.9: Intensity (arb.u.) vs. energy loss for Cr. Separated Cr-$L_{2,3}$ edges of two spectra with same oxygen content. The separated spectrum is only noise.

2.1.3 The Virtual Thickness of ELNES Separation Spectra

The total intensity of a spectrum after traversing the specimen in the TEM is given by

$$I_0 = I_{ZLP} \cdot e^{d/\lambda} \tag{2.20}$$

where I_{ZLP} is the zero-loss intensity, d is the specimen thickness and λ is the inelastic mean free path. This equation is only valid for small d/λ.

When taking the difference between two spectra recorded at positions of varying atomic concentrations as required for the ELNES separation method [27], the resulting spectrum can be associated to a virtual thickness x. x can be calculated as shown below, with F as the scaling factor needed in the ELNES separation method.

$$I_0^{Diff} = I_0^A - F \cdot I_0^B \tag{2.21}$$

I_0^{Diff} is the total intensity of the difference spectrum, I_0^A and I_0^B are the total intensities of the positions of measurement A and B. For the zero-loss intesity of the difference spectrum we get in analogy to Eq. 2.21

$$I_{ZLP}^{Diff} = I_{ZLP}^A - F \cdot I_{ZLP}^B. \tag{2.22}$$

When replacing $I_{ZLP}^A \cdot e^{d_A/\lambda_A - d_B/\lambda_B} = I_{ZLP}^B$ under the assumption of a constant I_0

$$I_0 = I_{ZLP}^A \cdot e^{d_A/\lambda_A} = I_{ZLP}^B \cdot e^{d_B/\lambda_B}. \tag{2.23}$$

we find when using Z for the thickness ratio of the oxide layers at positions A and B, e^A and e^B as shortcut for e^{d_A/λ_A} and e^{d_B/λ_B}, $I_0^A = I_{ZLP}^A e^A$

$$I_{ZLP}^{Diff} = I_{ZLP}^A \cdot (1 - Z) \tag{2.24}$$

$$I_0^{Diff} = I_{ZLP}^A \cdot (e^A - Ze^B) \tag{2.25}$$

With respect to Eq. (2.20) we now find (with λ_M as the mean free path in the bulk material)

$$\underbrace{I^A_{ZLP} \cdot (e^A - Ze^B)}_{I_0^{Diff}} = \underbrace{I^A_{ZLP} \cdot (1 - Z)}_{I_{ZLP}^{Diff}} \cdot e^{x/\lambda_M} \tag{2.26}$$

Solving Eq. (2.26) one easily finds

$$e^{x/\lambda_M} = \frac{e^A - Ze^B}{1 - Z} = e^A \cdot \frac{1 - Ze^{B-A}}{1 - Z}. \tag{2.27}$$

The thickness can be calculated as

$$\frac{x}{\lambda_M} = A + ln\{1 - Ze^{B-A}\} - ln\{1 - Z\}. \tag{2.28}$$

This result gives us two restrictions for the ELNES separation. Both must be fullfilled otherwise the ELNES separation is impossible.

1. $Z < 1$, which means, that the thickness of the oxide layer of position B must be larger than of position A, and

2. $Z < e^{A-B}$.

When substracting two spectra of same relative thicknesses (in units of MFP) and $Z \neq 1$, the difference spectrum has the same virtual thickness as the initial spectra.

$$\frac{x}{\lambda_M} = d_A/\lambda_A \quad (= d_B/\lambda_B) \tag{2.29}$$

This can be easily understood, because the ratio of I_0/I_{ZLP} is the same for both initial spectra and therefore constant for the difference spectrum due to the fact that only a linear combination of both was done.

Concluding can state that the virtual thickness of a difference spectrum has no physical significance. One must notice, that the difference usually is taken from background and plural scattering removed ELNES spectra. The neccessarity of these removals points out the independence of the ELNES concerning thicknesses. Only the signal's intensity but not its structure is influenced when measuring at positions of different thicknesses.

Nevertheless this discussion provides understanding and information of the restrictions which must be fullfilled if one wants the ELNES separation to work properly.

2.1.4 ELNES separation on interfaces

In this case we change the geometry from surface to interface ELNES separation. With this set-up we try to find out if Si is present in its oxidised state at the Al_2O_3 membrane / Si interface. The experiment is schematically shown in Fig. 2.10 where A represents Si and B represents Al.

To find out the chemical composition of the thin membrane we use ELNES separation and the fingerprint method. The positions of measurements are shown in figure 2.11. Our aim is to extract the ELNES from the Al bound in the membrane and compare it with an Al L-edge from Al_2O_3. It

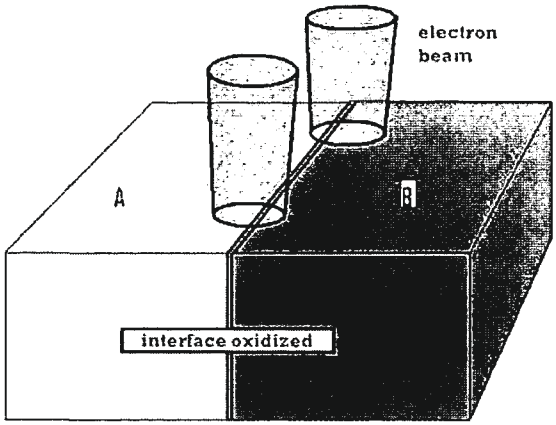

Figure 2.10: Schematic representation of the ELNES separation experiment in edge-on symmetry

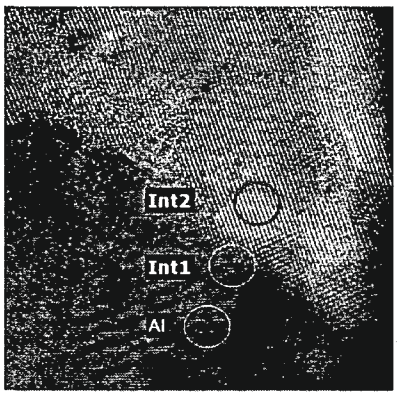

Figure 2.11: HRTEM image of the positions of measurements.

is found that the membrane consists of Al_2O_3 (see figures 2.12 and 2.13). The marked intensities are used for ELNES separation, as described in [33]. It is important to choose an energy interval before the energy threshold of the Al-L edge in Al_2O_3.

Another topic of interest was the oxidation state of Si at the Al_2O_3 - Si interface. For this purpose we chose two positions with different volume ratios of the Si/Al_2O_3-membrane. Again we use ELNES separation (figures 2.14 and 2.15) and find no peak at 108 eV energy loss which would be typical for SiO_2. We conclude that Si is not influenced by oxygen from the membrane.

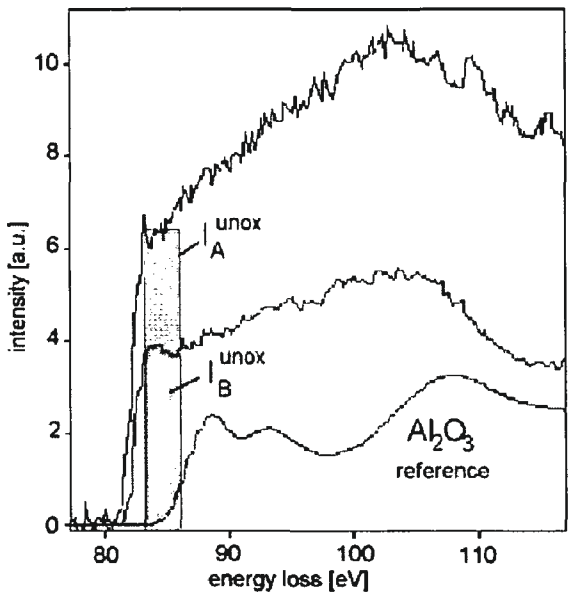

Figure 2.12: The two spectra for ELNES separation and a reference spectrum. The blue spectrum is from the membrane-Al interface, the green one from the Al crystal.

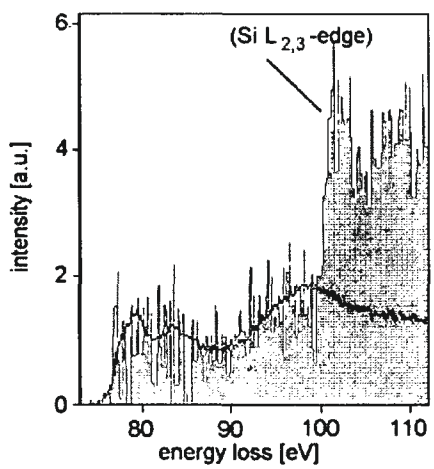

Figure 2.13: Subtratcting the two spectra we find that the resulting ELNES fits very well the reference spectrum. The membrane consitst of mainly of stoichiometric Al_2O_3.

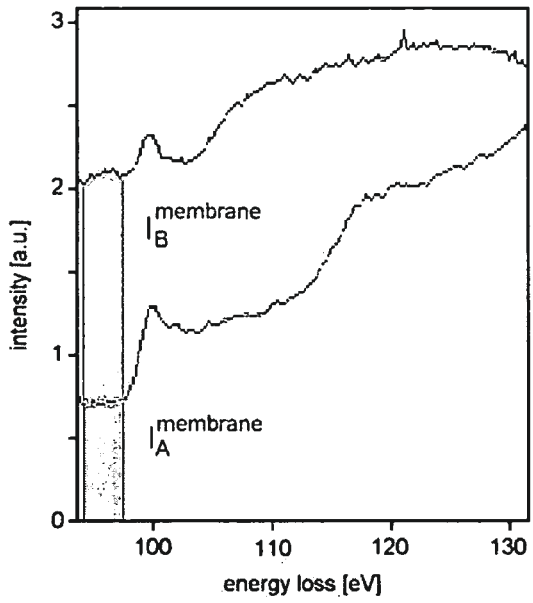

Figure 2.14: The blue spectrum corresponds to position *Int2* in the HRTEM image, the red one is from *Int1*. The intensities for ELNES separation are shown, too.

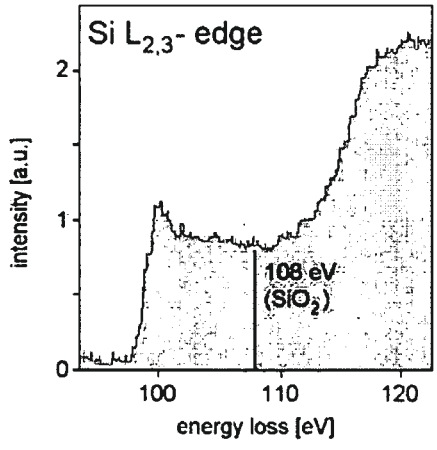

Figure 2.15: The resulting ELNES shows no peak at 108 eV energy loss. The Si stays uninfluenced by oxygen from the membrane.

2.2 The Zero-Loss Peak Problem for Bandgap Measurements

Since energy resolution of electron sources and spectrometers have been significantly improve recently, direct bandgap measurements by means of electron energy loss spectrometry (EELS) can nowadays be performed.
We discuss influences of data processing in the low loss region such as different methods to get rid of the tails in the bandgap signal coming from the inelastic peak of the EELS spectrum. We deal with influences coming from oxidised surfaces and show that the bandgap signal is dependent on the specimen thicknes.
For our investigations we use a transmission electron microscope (TEM) with a field emitter which has a natural energy width of 0.6 eV. For improving the energy resolution a Wien-type pre-specimen energy filter reduces the energy width down to 0.12 eV full width at half maximum (FWHM) in the inelastic peak. A high resolution post specimen energy filter (GATAN image filter - GIF) with an extremely small point spread function and aberration corrections up to 4th order is used for spectrum acquisition.

Bandgap measurements are not easy to perform. There are a few issues which should be taken care of. The predominant point is the specimen thickness. As a rule of thumbs there is to say that the thicker the specimen, the better is the signal in the post bandgap region. Thickness of up to three hundred nanometers can be used.
All presented measurements were performed in diffraction mode. The central spot was used for signal acquisition which gives an integral over all momenta. This is of no importance because the elementary cell of Si is isotropic. But the acquisition times can be very short with this setup.
For bandgap measurements the spectrometer dispersion was set to 0.02 eV/channel and in additional a complete energy loss spectrum with a dispersion of 0.2 eV was acquired up to an energy loss of 600 eV to investigate impurities in the specimen such as contamination or surface oxidation. A spectrum in image mode was acquired determine the thickness of the specimen at the probed area using the standard formula given in [6]. The accuracy of the thickness values is about 10 %. The monochromator of the TECNAI F20 at TU Delft was used so that the FWHM in the inelastic peak was 0.18 eV. Bandgap spectra were acquired in two steps, first a spectrum starting roughly at 0.3 eV was collected which includes the first plasmon peak. The intensity was chosen to be as high as possible so that no damage to the CCD was done. In a second step, a spectrum including the ZLP and the first plasmon peak was taken but with lower intensity. A lower intensity is obtained by shifting the electron beam in the monochromator. This of course leads to the effect that the electrons traversing the specimen have a lower or higher energy depending of the direction of the shift. Due to the fact that both spectra contain the first plasmon peak, an alignment of them is simple. Setting the maximum of the inelastic peak to zero on the energy scale, one can achieve a calibration of the spliced spectra. This method ensures that both parts of the spectra have the same spectral resolution because of same integration times and highest possible signal-to-noise ratio (SNR).

A detailed understanding of the electronic properties of semiconducting materials requires the determination of the joint density of states (JDOS) and the dielectric constant with high spatial resolution. Low electron energy loss spectrometry (EELS) provides a continous spectrum which represents all

electronic excitations with energies starting in the bandgap. This is one of two advantages compared with optical methods. So not only the loss function *Im(1/-ϵ)* contains more information, but also Kramers-Kronig Analysis (KKA) can be performed more accurately. Moreover, by means of angle resolved measurements in diffraction mode of the TEM one has access to the k-dependent dielectric function, whereas optical methods are, in principle, restricted to $\epsilon(0,\omega)$.
Since TEMs equipped with a cold field emitter or a pre-specimen energy filter are available, energy resolutions of less than 0.15 eV can be obtained. This improves the resolution of loss functions and dielectric properties to 1.5 eV [34] or even better. But analysis of EELS data and especially the extraction of the zero loss peak (ZLP) from the raw data gets critical at very low energies. Furthermore surface plasmon and oxidation state contributions must be eliminated precisely before performing KKA.

An approach to describe the interaction of a transmitted beam with the entire solid can be done in terms of a dielectric response function $\epsilon(q,\omega)$ [6]. Because the same response function describes the interaction of photons with a solid, this formalism allows energy-loss data to be correlated and compared with the results of optical measurements.
The energy loss function that is reproduced in the low loss signal of the EEL spectrum after ZLP subtraction (or deconvolution) is related to the dielectric function in the following way:

$$SSD(E)\ \alpha\ \frac{1}{q(E)^2}\cdot Im\left[\frac{1}{-\epsilon(\omega)}\right] \tag{2.30}$$

where $SSD(E)$ is the single scattering distribution (the spectrum after multiple scattering deconvolution), the term $\frac{1}{q(E)^2}$ is the kinematic contribution [35] and $Im(\frac{1}{-\epsilon(\omega)})$ is the energy loss function, which is defined in [6]. $q(E)$ is the momentum transfer of the inelastic scattering process and is shown schematically in Figure 2.16, where it is denoted as $\mathbf{q}$.

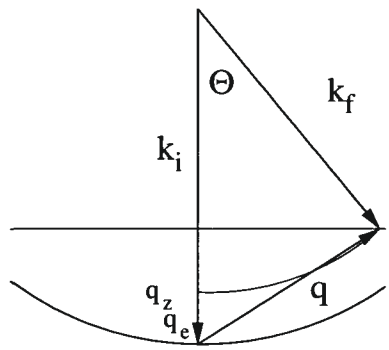

Figure 2.16: Scattering geometry for inelastic processes. k_i and k_f are the initial and final wave vectors, and q represents the momentum transfer.

Figure 2.17 shows the real and imaginary parts ϵ_1 and ϵ_2 of the dielectric function of Si in the range of 0 to 11.3 eV energy loss. The calculation was done by the *WIEN2k* code, which is based on the full potential augmented linear plane wave model. With this code, optical properties can be calculated using the package "OPTIC". For these calculations a dense mesh of 10000 eigenvalues and the corresponding eigenvectors are required. Then the imaginary part of the complex dielectric tensor is

computed. Using eq. 2.30, the EELS spectrum can be calculated as shown in fig. 2.18.
In figure 2.19 the real and imaginary part of the dielectric function of SiO_2 also is shown calculated with the *WIEN2k* code. Because of the fact that a native oxide layer covering Si has a thickness of only 70 Å, quantum size effects play an essential role simulating the low loss spectrum. Using only eq. 2.30 no satisfying spectrum will result. Lifetime broadening will be the dominant effect up to a thickness of 100 Å [36]. Therefore the spectrum must be broadened with a Gaussian function by some eV. We find that for a thickness of 70 Å a broadening of 0.5 eV gives the best fit to the experiment. Differently broadened spectra are shown in fig. 2.20.

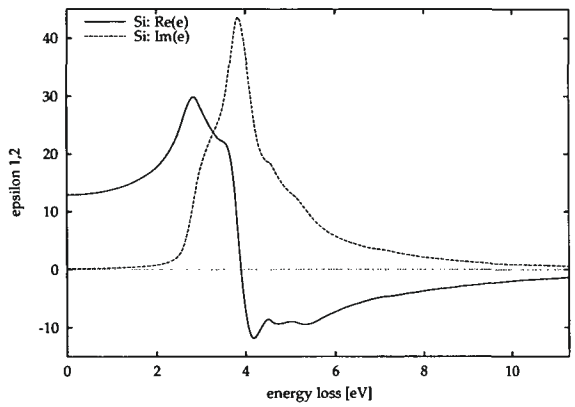

Figure 2.17: Simulation of the real and imaginary parts ϵ_1 and ϵ_2 of the dielectric function by use of the utility package "OPTIC" of the *WIEN2k* code for crystalline Si in the energy range of [0:11.3] eV.

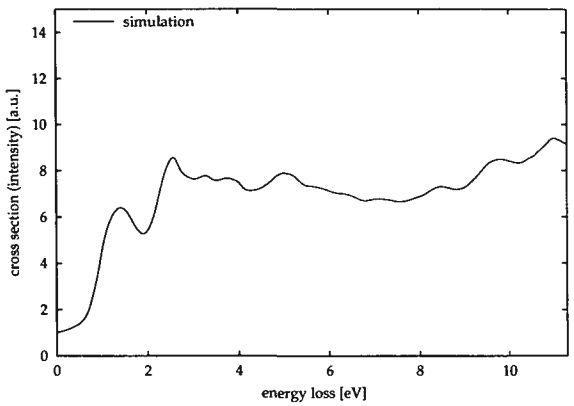

Figure 2.18: Simulation of the low loss of Si using eq. 2.30.

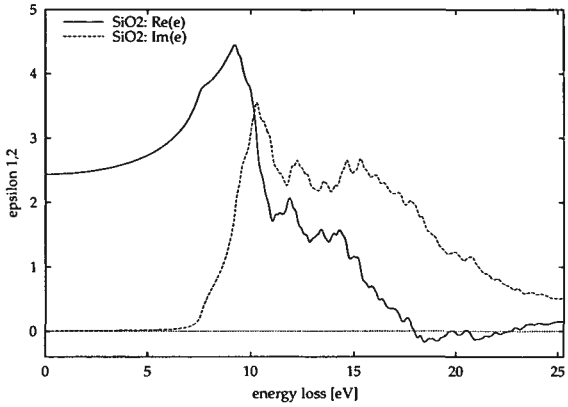

Figure 2.19: Real and imaginary part of the dielectic function of SiO_2 calculated with the *WIEN2k* code in the energy range of [0:24] eV.

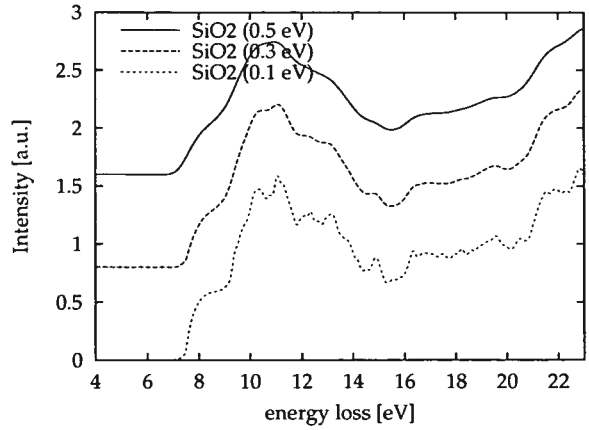

Figure 2.20: Simulation of the low loss of crystalline SiO_2 performed with the *WIEN2k* code. Different values for life time broadening were used (0.1, 0.3 and 0.5 eV) because it is not negligible due to the fact that the thickness of the oxide films is only 70 Å.

2.2.1 Different Methods for ZLP Subtraction and Deconvolution

The basic problem is to separate the tail of the zero loss peak from the low loss spectrum. To perform this, four procedures can be used. The mathematical one is the deconvolution of all signals coming from the ZLP. Another one would be a simple subtraction of the ZLP - either the mirrored left-hand side or the vacuum ZLP - from the low loss spectrum and one possibility is a power law background fit close before the edge onset.

subtraction of the left-hand tail of the inelastic peak

The second possibility is to subtract the ZLP [37],[38]. This is not easy to do because the right hand side tails of the ZLP are hidden in the signal. Therefore the left hand side tail of the ZLP is flapped to the right hand side and than the subtraction can be done. This of course presumes a symmetric ZLP. The symmetry of the ZLP in modern TEMs is dependent on the gun tilt and the gun lens settings. In reality one never has a symmetric ZLP and therefore the simple subtraction of the inelastic peak is only a compromise. The peak heights of the post bandgap region are extremely sensitive to the subtraction of the tail of the ZLP. Here an error might be introduced.
A further disadvantage is that the tail is very noisy and when performing the subtraction more noise will be added to the final spectrum. This makes it difficult again to find out the proper width of the band gap.

subtraction of a vacuum ZLP

Better than mirroring the left-hand side of the ZLP to the right-hand side when working with a FEG equipped TEM is to acquire serarately a vacuum ZLP under exactly the same conditions. The only difficulty is that the specimen broadens the ZLP and therefore the vacuum ZLP would be narrower than the one of the spectrum. Nevertheless, when defocussing the spectrometer a little bit, excellent results can be obtained. The SNR is good and can be even improved when adding many vacuum ZLPs with same FWHM.

power law background fit at very low energies

A good power law fit of the tail can be a solution, too. The width of the bandgap can be found easily with this method. Noise is not added as it is done with the other methods. The big disadvantage is that the tails of the ZLP are not obeying a power law. The fit rapidly gets wrong after only one or two electron volts. This means, that the peak heights in the post bandgap region are wrong. Quantitative statements arre therefore not possible. Best results can be obtained if the vacuum ZLP is fitted by a power law in the interesting energy region. This fit can afterwards be subtracted from the spectrum.

deconvolution of the spectrum with an "instrument function"

The mathemathical correct version would be the deconvolution of the instrument function, which includes the δ-shaped ZLP convoluted with the broadening of the electron source, lens abberations and all other influences causing a broadening of the ZLP [39]. The advantage of deconvolution is that the spectrum can be used for Kramers-Kronig analysis (KKA) without introducing too much error since the spectrum usually is flattened by a Gaussian function. A further advantage is that the left-hand tail of the ZLP is removed, too, which is not the case when subtracting the ZLP, as mentioned above.

2.2.2 Mathematical Aspects of ZLP Deconvolution

Above it was shown that getting rid of the ZLP and its tails is the main difficulty in bandgap measurements by means of EELS. In section 2.2.1 different solutions for this problem are pointed out. In the following section the mathematical aspects are specified.

In following it is never dealt with the subtraction of the left-hand side tail of the ZLP , because there is no physical reason why this should give an exact bandgap position. The ZLP of a FEG is never symmetric as mentioned in many papers and shown in much more measurements. This method seems to be the worst one. Therfore focus is set on the *deconvolution of the spectrum with an "instrumental function"*. For better illustration figure 2.21 shows a typical assymmetric ZLP produced by a FEG.

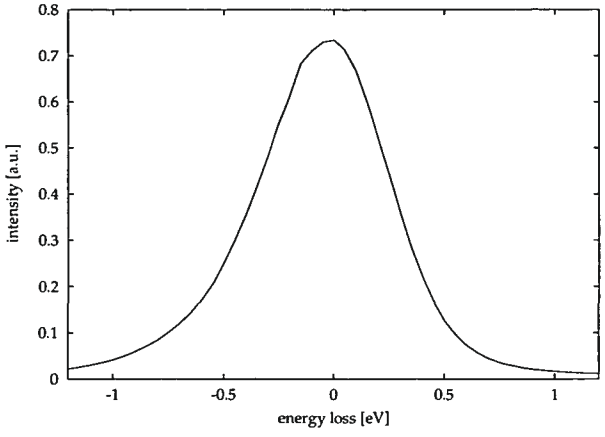

Figure 2.21: ZLP produced by a FEG. It usually is very assymetric which prohibits using the left-hand side for ZLP subtraction when trying to define the width of a bandgap.

Similar to the *Fourier Ratio* method suggested by Egerton for multiple scattering deconvolution, the energy loss spectrum is divided into two regions. The zero loss (ZL) spectrum and the plasmon (PL) spectrum containing anything except the ZLP. We assume the ZLP to be a perfect δ-peak at 0 eV energy loss broadened with an "instrumental function". This instrumental function can contain any phenomenon contributing to the broadening of the ZLP, such as different escape lengths for the electrons in the emitting tip (FEG), broadening due to temperature gradients on the tips surface, broadening effects occuring when traversing the specimen and leading to all kinds of aberrations in the analyser and spectrum forming lens system.
In order to justify such a procedure let $K_p(E)$ be an ideal "plasmon loss single scattering distribution". When the electrons transmit a specimen and are recorded by a spectrometer and TEM system having an instrumental function $R(E)$, the whole low loss intensity $J_l(E)$ will be

$$J_l(E) = \{K_p(E) + \delta(E) \cdot I_0\} * R(E) \tag{2.31}$$

Now the *Fourier coefficient* of the plasmon loss can be written as

$$k_p(\nu) = \frac{j_l(\nu)}{I_0 r(\nu)} - const. \tag{2.32}$$

Performing an *inverse Fourier Transform* gives the plasmon loss single scattering distribution unbroadened by the instrumental function of the TEM-spectrometer system without the ZLP. However, as discussed in [40] and [41], such a complete deconvolution is feasable only if the spectrum was acquired with infinite precission, that means without noise. Such a noise extends to high frequencies ν in the power spectrum and the noise free component of $k_p(\nu)$ falls towards zero as ν increases. As a result, the fractional noise content in $k_p(\nu)$ increases with ν, and at high frequencies $k_p(\nu)$ is usually dominated by noise. Since $r(\nu)$ also falls with increasing ν, the high-frequency noise content of $k_p(\nu)$ is preferentially amplified when divided by $r(\nu)$, as in eq. 2.32, and the inverse transform $K_p(E)$ is submerged in high-frequency noise. To avoid this effect, the Fourier coefficients ratio is multiplied with

the Fourier transform of a Gaussian function. We obtain

$$k'_p(\nu) = I_0 e^{-\pi^2\sigma^2\nu^2} \frac{j_l(\nu)}{I_0 r(\nu)} - c \cdot I_0 e^{-\pi^2\sigma^2\nu^2}. \tag{2.33}$$

If $\sigma = \Delta E/1.665$, where ΔE is the experimental energy resolution (FWHM of the ZLP). The inverse transform has a noise content less than the original data. $I_0 e^{-\pi^2\sigma^2\nu^2}$ is the Gaussian shaped replaced ZLP which is subtracted immedeately.
Experimental results will be discussed in section 2.3. Figure 2.22 shows the difference spectrum between a carefully ZLP subtracted and deconvolved low loss spectrum. The difference is only noise, but this requires an extremely careful acquisition.

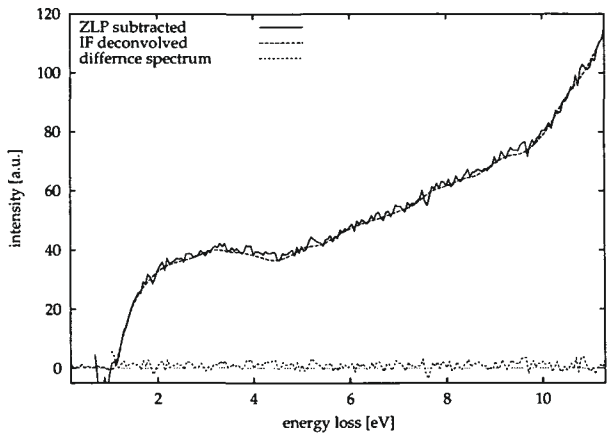

Figure 2.22: Difference between a ZLP subtracted and deconvolved spectrum. When acquiring the ZL spectrum very carefully, the difference can be reduced to noise, which is suppressed by a Gaussian smoothing fuction in the deconvolution method.

2.2.3 Influence of Surface Plasmons

Analogous to volume plasmons there exist longitudinal waves which travel along surfaces or interfaces. In the free-electron appriximation the surface oscillation is resonant at $\omega_s = \omega_p/\sqrt{2}$.
The position of the plasmon peak in Si is at 16.7 eV. The means that the surface plasmon is expected at 11.8 eV. Experiments show that it can be found at 8 eV (see fig. 2.23).

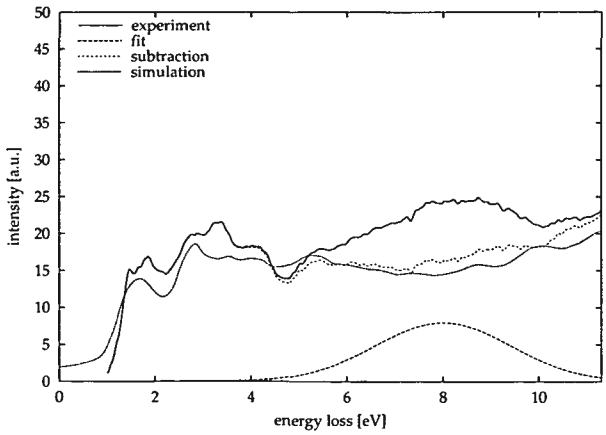

Figure 2.23: The surface plasmon can be fitted with a Gaussian function and be subtracted from the experimental spectrum. No influence on the first few eV of the spectrum can be observed. Still a difference between simulation and experiment can be found from 7 eV upwards (see next subsection).

The reason for this damping can be explained by a surface contamination, i.e. a thin oxide layer.

2.2.4 Influence of Surface Oxide on the post bandgap signal

The investigated specimen was oxidised in air for several days so that a thin amorphous SiO_2 layer was formed covering the surfaces. This enabled us to investigate even very confined bulk volumes without the risk of losing the thinnest parts of the Si-specimen during insertation into the TEM. On the other hand, energy loss signal of SiO_2 would not affect the post bandgap signal of Si below 4 eV because the bandgap of SiO_2 has a width of 8 eV. But due to lifetime broadening in confined volumes [36],[42] we find an influence of the SiO_2 bandgap signal from 4 eV upwards.
The thickness of the SiO_2 layer can be calculated using the thickness dependencies of the ZLP and the volume plasmon of Si (eq. 2.34 and 2.35)

$$I_{ZLP} = I_0 \cdot exp(-\frac{d}{\lambda}) \tag{2.34}$$

$$I_{plasmon} = C \cdot exp(-\frac{d}{\lambda}) \cdot \frac{d}{\lambda} \tag{2.35}$$

where I_0 is the intensity of the incoming electron beam, d is the specimen thickness in nm and λ is the inelastic mean free path (MFP) for electrons at 200 keV in the specimen. Using these relations the intensities of the plasmons can be normalised depending on the intensities in the elastic peak. Furthermore the thickness of the oxide layer can be calculated from the measurements. Figure 2.24 shows the relations of the intensities in the ZLP and the first volume plasmon of Si considering of the fact that Si and SiO_2 have different λ's.

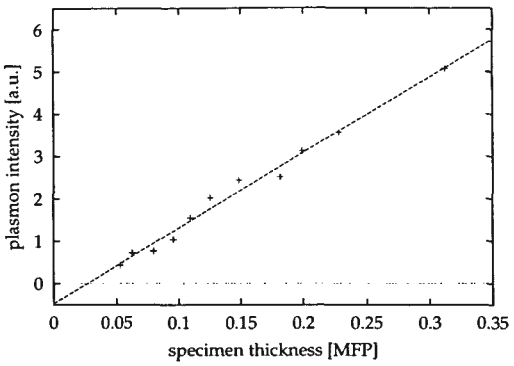

Figure 2.24: Normalised plasmon intensities vs specimen thickness in units of MFP for $\beta = 0.18\,mrad$. The zero-value of the fitted line gives the thickness of the surface oxide. It is 14 nm which is in excellent agreement with [43], where the thickness of natural SiO_2 on Si is given with 7 nm (for each side of the specimen).

For these measurements one has to take into account that the collection angle $\beta = 0.18\,mrad$ and therefore the MFP in SiO_2 is 526.162 nm. For the fitting curve we find the zero-value at 0.027 MFP which corresponds to a thickness of 14 nm. Therefore this is the thickness of both oxide layers, on the top and the bottom side of the specimen.
Figure 2.25 shows a ZLP subtracted and multiple scattering deconvolved spectrum acquired at a 216 nm thick position. Remarkable is the maximum at 8 eV coming from the SiO_2 surface layer which is the post-bandgap energy region of silicon. When subtracting the simulated SiO_2 signal from the experimental data a broadening parameter with respect to life time broadening of 0.5 eV is required to reproduce the simulation for the Si bandgap very well.

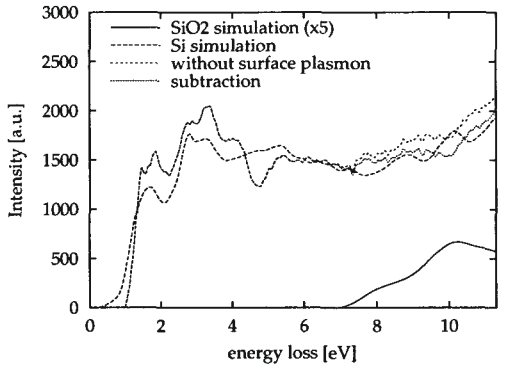

Figure 2.25: The subtraction of the simulated low loss of SiO_2 from the measured spectrum fits quite well to the simulation of the bulk Si post bandgap region. However, the first features of the Si signal cannot be influenced by the presence of SiO_2 becuase these states are lying in the bandgap of the insulating oxide.

2.2.5 Influence of Thickness

Figure 2.26 shows spectra from positions of the wafer with different thicknesses due to specimen preparation. Remarkable is the evolution of some features and that only the one from the thickest position fits the simulation already shown in fig. 2.25. The maximum at 3.15 eV and the minimum at 4.36 eV keeps constant through all thicknesses. The maximum comes from the transition of the upper most valence band to the second conduction band in the Brillouin Zone (BZ) center, which is the $\Gamma_{25'}$-$\Gamma_{2'}$ transition. This transition is visible for all thicknesses except for the smallest one. The minimum at 4.36 eV is followed by a maximm at 5.14 eV that corresponds to the X_4-X_{1c} transition. This is in good agreement with different kinds of calculations and experiments [44],[45],[46] and [47].
It seems that the transitions to Γ_{15} and along the Δ direction of the BZ get more pronunced with increasing thickness.

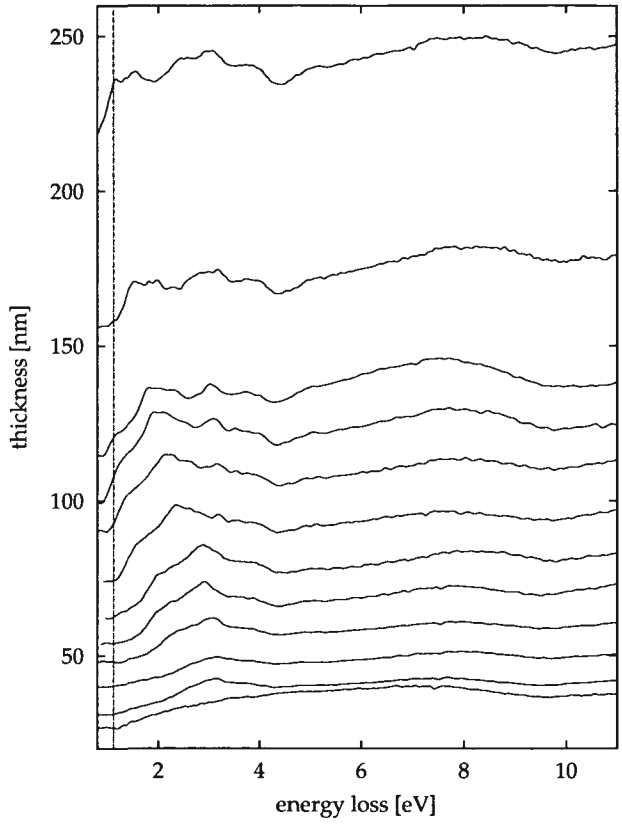

Figure 2.26: Si post bandgap spectra after subtraction of the fitted plasmon. Remarkable is the dependence on the specimen thickness. The thickness were 25, 31, 40, 48, 54, 62, 74, 90, 99, 114, 155 and 216 nm. The dashed line shows the 1.12 eV known from literature as the Si bandgap.

Completely different from all others is the one acquired at 26 nm thickness. It reminds one of the quantum size effect of the Si-L edge described in [36]. When taking into account the thickness of the oxide layers on both sides of the specimen, a bulk thickness of Si of 12 nm is found. This is

approximately the order of magnitude, where quantum size effects still appear.

2.3 Direct Measurements of the Si Bandgap without a Monochromated TEM

In the last section we learned about the difficulties occuring when trying to measure the bandgap of semiconductors. The same can be done with a conventional TEM but it is much more difficult to obtain good spectra. In the following few paragraphs the prefered method is explained.
Under the aspect of a much broader ZLP than available in a monochromated TEM (usually 0.7 eV and 0.14 eV, respectively) one must take into account that the tail of the ZLP has still nearly 1.7% of the ZLP's height at an energy loss of 1.12 eV. With a monochromated TEM this value is only 0.0025% of the maximum intensity (whereas a Gaussian function has only 0.0081% of its maximum value at this point). This would be an improvement by a factor of 680! Nevertheless deconvolution can be successful if a vacuum ZLP has been acquired under exactly the same conditions. The ZLP need not neccessarily be symmetric or even very beautiful, it can also be foozled as the one shown in fig. 2.21. But careful acquisition is indispensable either for deconvolution or for subtraction of the ZLP, as described in chaper 2.2.1.
The disadvantage is of course that no finestructure of transitions from the valence to conduction band can be separated any more.

2.3.1 Precision of bandgap determination without monochromator

Due to the fact that the first few eV of a low loss spectrum are a convolution of the ZLP with the scattering distribution of interband transition from valence to conduction band, the limiting factor for bandgap determination is the signal-to-noise ratio (SNR). The experimental conditions should be chosen in that way, that the specimen thickness is not too low, because this would give a decrease of effective scattering cross-sections. In figs. 2.27 and 2.28 two measurements for crystalline and amorphous Silicon are shown. Because the resulting spectrum from the deconvolution method was shown in section 2.2.1, the subtraction method was applied this time to prove the accuracy of this method. We will get back to these methods in chapter 4.1, when the screening model for a Si solution in Al is investigated.

Table 2.2: Several bandgaps determined by this method [48].

material	experiment	literature	reference
c-Si	1.15 eV	1.12 eV	[11]
a-Si	1.70 eV	1.70 eV	[11]
SiO_2	8.50 eV	8.50 eV	[49]
Al_2O_3	8.30 eV	8.00 eV	[49]

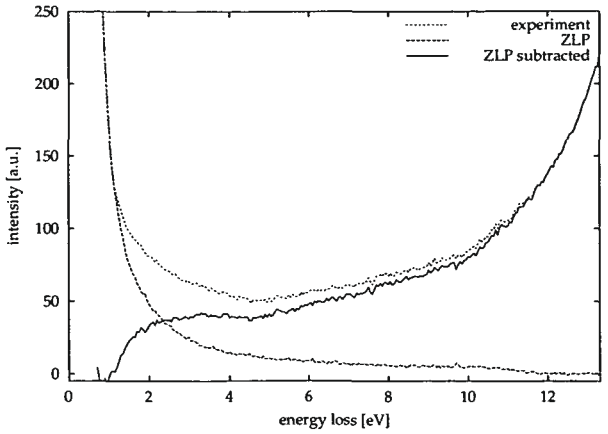

Figure 2.27: Bandgap measurement of crystalline Silicon via EELS performed at the TECNAI at Vienna University of Technology. The signal threshold gives the width of the bandgap and is found to be 1.15 eV. The spectrometer dispersion was set to 0.05 eV/channel.

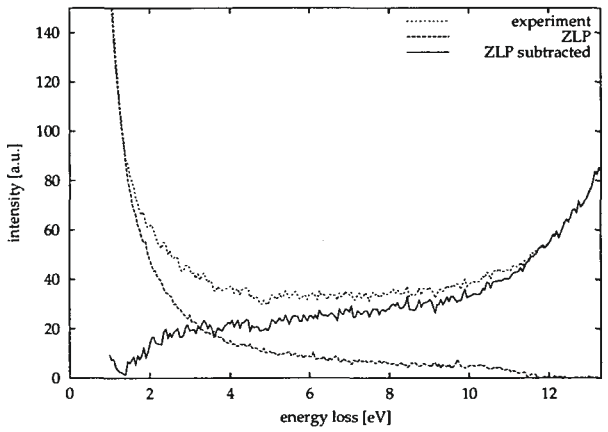

Figure 2.28: Bandgap measurement of amorphous Silicon via EELS performed at the TECNAI at Vienna University of Technology. The signal threshold gives the width of the bandgap and is found to be 1.7 eV. The spectrometer dispersion was set to 0.05 eV/channel.

Chapter 3

Delocalization in EELS Nano-Analysis

In this chapter the ultimate possibilities which can be derived by means of EELS analysis are discussed. This should be expressed in the word "Nano-Analysis". Since today's world developpements go into the direction of nanoscale technologies, nanocharacterisation plays a more and more important role. This section gives an outlook over today's possibilities and limitations.
Latest results in nanoscale characterisation of semiconductor materials focus on resolving single atoms in the elastic and inelastic image of a scanning transmission electron microscope (STEM). With developments of C_s-correctors, elastic imaging has tremendously been improved, because the spherical abberation of the objective lens can be reduced by an order of magnitude. In this section we deal with the question what effects could be observed even without the help of a C_s corrector and demonstrate simulations and present their experimental confirmation of the parity conservation effect under consideration of localization in the Si-$L_{2,3}$ edge. But before the limitations of "Nano-Analysis" are discussed in detail, including recent theoretical and experimental results of the EELS community. First the delocalization of energy losses is explained and it is continued with the delocalization of a focussed probe when penetrating though a specimen. Last but not least, as mentioned above, my own results are shown.

3.1 Delocalization of Energy Losses

"How delocalized is an EELS signal?", with these words starts a work done by Dave Muller and John Silcox [50] dealing with delocalization in inelastic scattering. Niels Bohr [51] offered a classical explanation leading to the adiabatic criterion for a cutoff impact parameter $b_{max} = v/\omega$, for a fast electron, velocity v, and an energy loss of frequency ω.
Classically the energy loss of a swift electron passing a bound electron at impact parameter b is given in the impulse approximation as [51]

$$\Delta E(b) = \frac{2e^4}{mv^2} \cdot \frac{1}{b^2}. \tag{3.1}$$

This expression is valid provided the colission time b/v is short compared to the restoring period of the bound electron $1/\omega$ (i.e. the electric field generated by the swift electron is above the resonance

frequency of the bound electron). When the collision time is longer, the bound electron can follow the time varying field and remains bound so the interaction is adiabatic. The cross-over at $b_{max} = v/\omega$ is Bohr's cutoff beyond which the target is dynamically screened. This screening arises from the more slowly varying field seen at large distances, rather than any property of the intervening medium and so will be expected in free space as well.
For a 200 keV swift electron the impact parameter is (with E as the energy loss in eV)

$$b_{max} = \frac{1.3678^{-7}[\mathrm{m/eV}]}{E[\mathrm{eV}]}. \tag{3.2}$$

Table 3.1 gives some impact parameters of specific energy losses, which are used within this theses.

	energy loss [eV]	b_{max} [Å]
(Al-surface plasmon)	7	(195)
Al-plasmon loss	15	91.2
Si-plasmon loss	16.7	81.9
Al-L edge	72	19.0
Sl-L edge	99	13.8
O-K edge	531	2.6
La $M_{4,5}$ edge	851	1.6
Al-K edge	1560	0.8
Si-K edge	1839	0.7

Table 3.1: Impact parameters for some energy losses

When locating the detector far enough off axis so that it no longer overlaps with the objective aperture and $\beta^2 >> \Theta_0^2$ then [50] inelastic scattering is just as localized as the incident probe intensity, independent from the energy loss.

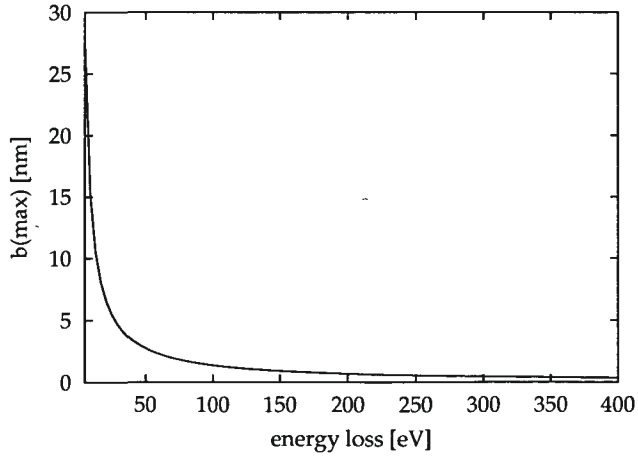

Figure 3.1: Impact parameter vs. energy loss for 200 keV electrons.

3.1.1 Experimental Proof of Delocalization

In this section an experimental proof of delocalization is given. Both using STEM and conventional TEM (CTEM). The specimen used was grinded and ionmilled. Finally a hole was "burned" in-situ into an Al-grain using the focussed electron beam of the TEM. This prevented the edge from oxidizing. Figure 3.2 shows an HRTEM image of the hole inside the Al grain. The line denotes the EELS line spectrum acquisition using STEM.

Figure 3.2: HRTEM image of the in-situ prepared hole in an Al grain.

3.1.2 Experimental Results using STEM

As described above, STEM is one possibility to observe delocalization phenomenon of energy losses. If an EELS line scan is performed from the hole into the specimen, no beam broadening can appear in the vacuum. This means that all losses observed before the focussed beam hits the specimen are due to delocalization. In figure 3.3 the spectrum image of this experiment is shown. The brightness in the image reproduces the intensity in the EELS spectrum. Each nanometer a spectrum was acquired using a 2Å spot. Figure 3.6 shows the line profile version of the specrta starting 22 nm inside the hole. The arrows indicate a) the damped surface plasmon of Al at 4.5 eV energy loss. This damping is due to oxidation on the top and bottom surface of the specimen. b) denotes the not damped surface plasmon stemming from the in-situ prepared edge and c) points at the 2^{nd} bulk plasmon at 30 eV energy loss which is due to plural scattering and has therefore the same delocalization width as the first bulk plasmon at 15 eV. From the spectrum image (SI) the delocalization width of the energy losses can be measured. But one must take care for background subtraction. For the surface plasmon of the in-situ prepared edge of the specimen a line trace is drawn at 7±0.3 eV energy loss and the background signal was chosen at 10±0.3 eV.

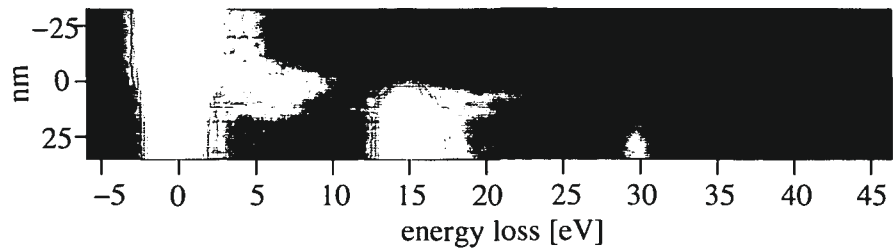

Figure 3.3: Spectrum image of the EELS line scan from the position shown in fig. 3.2. Note the double peaked surface plasmon at 5 eV and 7 eV energy loss.

Then the intensities from both traces were normalized deep inside the hole. Then a simple subtraction was performed. The result is shown in figure 3.4. The surface plasmon is very symmetric with respect to the interface due to fact that the in-situ prepared surface is parallel to the electron beam. Because the signal for the undamped surface plasmon is very weak, the delocalization width can only be measured up to ± 10 nm (on both sides).

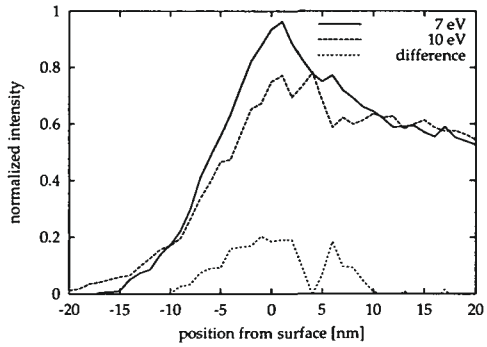

Figure 3.4: Measured delocalization of the weak surface plasmon at 7 eV.

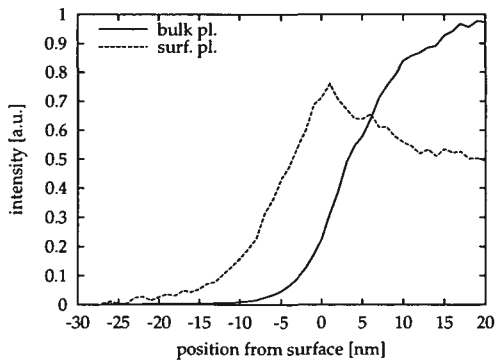

Figure 3.5: Measured delocalization of the surface plasmon at 4.5 eV compared with the bulk plasmon at 15 eV.

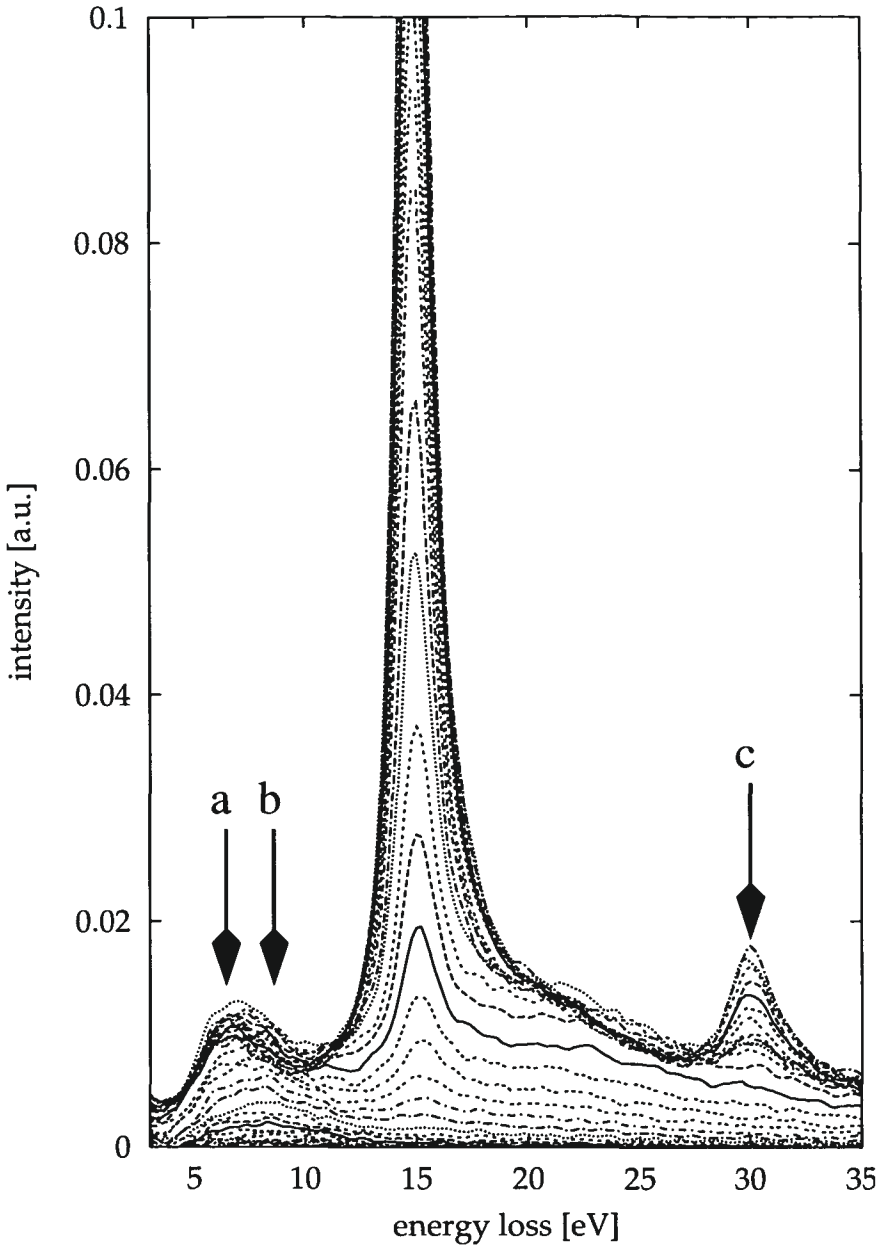

Figure 3.6: Line plot version of some EELS spectra from 3.6 after removal of the ZLP. The lowest spectrum was acquired 22nm away from the rim of the hole (position -22 nm). The lateral distance between two spectra was 1 nm, spot size was 0.2 nm.

The width of delocalization can be measured for the plasmon using STEM mode of the TEM. But for the Al-L edge it is not so easy, for several reasons. One of them is the instability of the ZLP position. Therefore the ZLP is needed to realign the spectra. This means that the ZLP and the Al-L edge at 72 eV must be on one and the same spectrum. This has a further advantage, the number of the spectrum at the surface cannot differ. If a separate ZLP spectrum and core-loss spectrum are acquired, specimen

drift causes some incertainty concerning the position of the surface. But on the other hand the SNR at the Al core edge is very bad. The CCD must not be damaged by too high intensity in the ZLP. Figure 3.5 shows the intensity profile of the bulk and the surface plasmon. Delocalization is very high (comparable with the impact parameter b_{max}. On the other hand, figure 3.7 shows the jump ratio profile from the Al-L edge. For comparison, the plasmon intensity profile is also shown. All negative values in the jump ratio were set to zero, since a negative value means, that the background just follows its power law and no ionisation edge can be found.

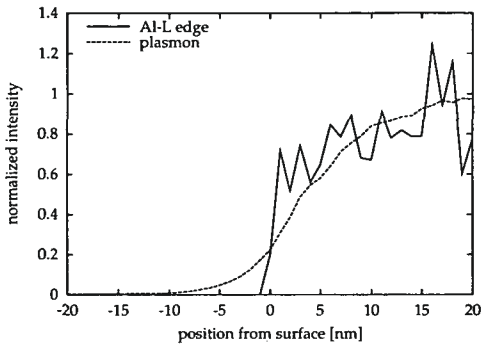

Figure 3.7: Jump ratio profile of the Al-L edge. For comparison the bulk plasmon profile is added, too.

3.1.3 Experimental Results using EFTEM

Another possibility to measure the delocalization is using EFTEM. From plasmon mapping we know that sharp structures as interfaces or surfaces are never reproduced sharply. This is not a problem of focus but of delocalization. It is therefore impossible to know where the interface or surface is located exactly. For the ALILE produced specimens the exact thickness of the alumina membrane cannot be measured via plasmon imaging. Usually the membrane thickness is between 3 and 10 nm. The delocalization is in the range of 10 nm for each side. Obviously, thickness measurements of such a thin structure cannot be performed in this way.
In figure 3.8 a jump-ratio image and a plasmon map of the hole in the Al grain (shown in fig. 3.2) are shown. The hole was enlarged with the electron beam between the two measurements (STEM and EFTEM) to be sure that no contamination from STEM is influencing the measuremnts.

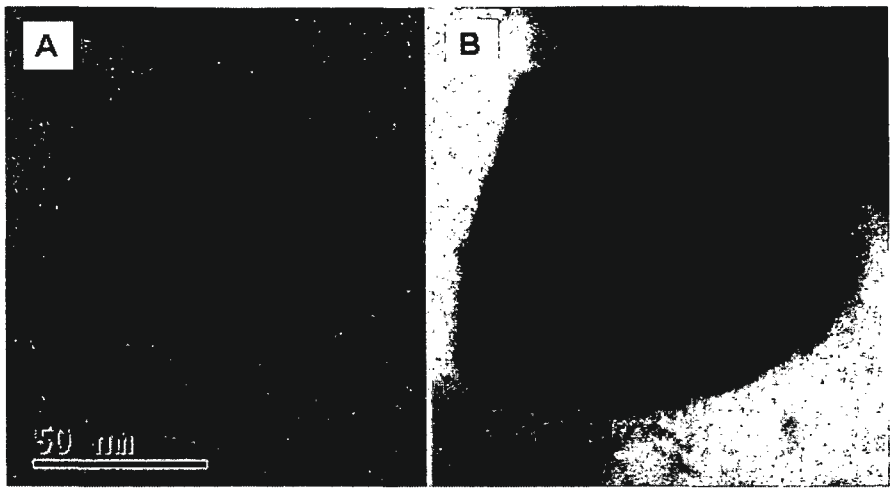

Figure 3.8: EFTEM images of the in-situ prepared hole in an Al grain. A) shows the jump ratio image of the Al-L edge and B) is the plasmon filtered image at 15 ± 0.5 eV. The hole was enlarged with the electron beam between the two measurements (STEM and EFTEM) to be sure that no contamination from STEM is influencing the EFTEM recordings.

Drawing a gray-scale profile across the border of the hole at the same position for both images in figure 3.8 and scaling them to same hight, the delocalization can be compared and measured quite well. The distance within which the 15 eV signal can be detected is dificult to measure, becasue of worse SNR for positions far off the surface, but it can be estimated with at least 13 nm. This is much more as the calculated impact parameter from Eq. 3.2 shown in table 3.1.

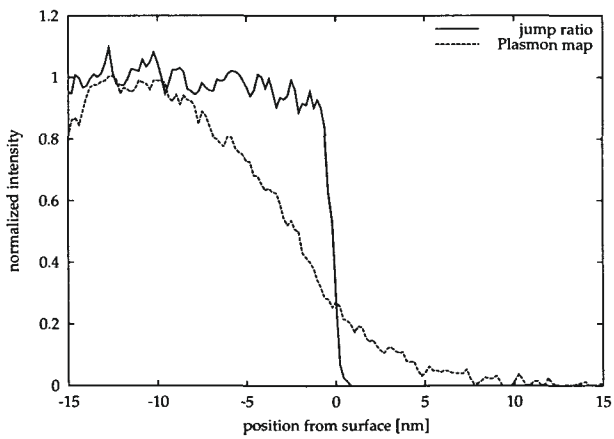

Figure 3.9: Normalized intensity profiles of the Al-L edge jump ratio image and the bulk plasmon map. The delocalization for the plasmon is found to be in the range of 12 nm, the L-edge signal is localized within 1 nm.

The reason for the assymetric shape of the Al-bulk plasmon profile is that oscillator strength is transferred to the surface plasmons as shown in section 3.1.2.

3.2 Delocalization of the Electron Probe

In [10] multi slice calculations for beam propagation in Si (110) were carried out at different atomic positions. Due to the fact that the electrons channel along the crystal axes, beam spreading is not very large, if the potentials are strong enough. Chrisitian Dwyers et al. [52] calculated beam spreading for other positions, too. The one we used for EELS measurements was not published, therefore the beam distribution according to increasing thickness [53] is shown here (figure 3.10). Due to the fact that the ratio between the atomic distance and the minimum beam size in the TECNAI F20 our case can be treated similar to the one shown in calculations for the 0.7 Å probe at the position B1 in [52] which is half the way between two atomic columns in (100) orientation, a similar spreading can be estimated. The *max* values given in figure 3.10 give the maximum intensity within a circle of 0.2 Å diameter around the beam position. Due to the fact that for the 0.7 Å probe, which is the most comparable one, the maximum is only 0.2 per cent of the incoming intensity for a thickness of 50 nm and that for the on atom measurement we would have 13.7 per cent (see [52]). Furthermore most signal would come in any case from the atomic positions, therefore the difference in the EELS spectrum cannot be very large.
The extent of the volume from which the EELS signal originates has been considered in some detail by Rafferty and Pennycook [54]. Using the inelastic matrix element given by Maslen and Rossouw [55], and assuming incoherent conditions, Rafferty and Pennycook [54] calculated K-shell EELS object functions for various atomic numbers and collector apertures. Using these calculations as a guideline, the width of the Gaussian K-shell EELS object function for silicon has been estimated to be $\approx$ 25 Å for a 100 keV electron beam and a 20 mrad collector aperture. In Dwyer's approach, he makes the further simplification of assuming the object function to be a top-hat function, not a Gaussian, and he chooses the width of this function to be 0.4 Å.

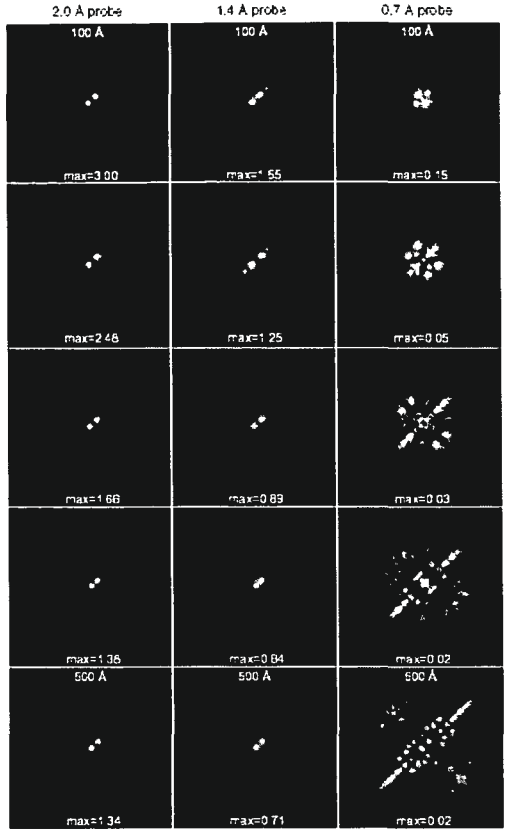

Figure 3.10: Real space intensity maps vs.crystal thickness for 2.0 Å (left column), 1.4 Å (middle column) and 0.7 Å (right column) probes between two columns in Si (111). The intensity is mapped for crystal thicknesses up to 500 Å at 100 Å intervals (increasing from top to bottom).The size of each cell is 32.6 Å 32.6 Å (from [52]).

On the other hand, recently a work [56] was published showing single atom detection. In this work beam spreading was not such a problem. The experiment was carried out using a C_s corrected VG STEM with a minimum spot size of 0.13 Å at a convergence angle of 25 mrad. Figure 3.11 shows the fantastic result.

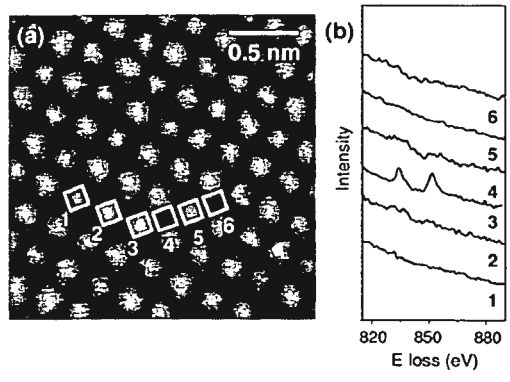

Figure 3.11: (a) Z -contrast image with (b) EELS spectra showing spectroscopic identification of a single La atom at atomic spatial resolution, with the same beam used for imaging. The $M_{4,5}$ lines of La are seen strongly in spectrum 3 obtained from the bright column at $2x10^7$ magnification and a total collection time of 30 s. Other spectra from neighboring columns show much reduced or undetectable La signal. These spectra were obtained with collection times of 20 s, and are shown normalized to the pre-edge intensity and displaced vertically for clarity (from [56]).

As shown, the discussion is very controversary. However, experimental results show that EELS nano-analysis is not as limited as simulations would let us expect.

3.3 EELS Nano-Analysis using STEM mode

Since the advent of spectroscopy in transmission mode [57] spatial resolution has been improved tremendous. Nowadays transmission electron microscopes (TEM) and scanning TEMs (STEM) combined with electron energy loss spectrometers (EELS) can provide information of the electronic states of single atoms [56, 58]. This opens the door to the question, if differently localized states - as the s- and p-states - can be detected in the EELS signal with spatial differences on the sub-nm scale. But one has to take care when interpreting the energy loss near edge structure (ELNES) of such measurements, because, as discussed later, for the p-states a change in parity will play a dominant role. However, highly spatially resolved EELS signal can only be achieved in scanning transmission geometry [59, 60]. Simultanously the specimen can be imaged with atomic resolution using an annular dark field (ADF) detector. Resolution can be improved when using a C_s-corrector as described elsewhere [61, 10, 62, 63]. In an uncorrected system, the probe size, determined by the spherical abberation (C_s), limits the instrumental resolution. Lupini and Pennycook [64] report that the probe size can be reduced to the size of 1-s like Bloch states when using a C_s-corrector. It is proposed that the ultimate resolution limit will then be the extent of those states [61]. But in principle the resolution is limited by the probe size independent of the usage of a C_s-corrector [65]. For special materials as diamond or GaAs the 1-s state approach breaks down, because the atomic distances are smaller than the extension of the 1-s states [66]. But for Si it is still valid.
For measuring differently delocalized states the following considerations suggested in [64] must be un-

derstood and are therefore mentioned briefly at this point. A simple incoherent model is used for comparison of elastic and inelastic scattering. The elastic image is described as a convolution of the effective probe with an object function which itself consists of an array of δ-functions at the atomic positions in the crystal lattice. Due to the fact that the intensity in an ADF image and the low angle scattered intensity must be constant (i.e. the probe intensity before transmission through the specimen), the intensity in the EELS signal can be modelled. When having total localization, the inelastic object function is also a δ-array. For total delocalization it will be a constant. The EELS intensity in the described cases will then be

$$I_{EELS}(R) = [O(R) \otimes P^2_{eff}(R)] \cdot [1 - \delta(R) \otimes P^2_{eff}(R)]$$

with $P^2_{eff}(R)$ denoting the effective probe and $O(R)$ the object function of inelastic scattering. The first set of brackets will resemble the ADF-image with maxima at the atomic positions if a fully localized scattering event is assumpted ($O(R) = \delta(R)$). Whereas the second set of brackets represents the total intensity entering the spectrometer. But when inserting a fully delocalized object function for the inelastic scattering event ($O(R) = const$), implying that the delocalization is significantly larger that the atomic spacings, the maximum intensity will lie in between the atomic column positions. Theoretical calculations showed that the localization of the inelastic object function can be appreciated by the geometrical extent of the core electron orbital [54]. In Fig. 3.12 the projected potential of two dumbbells in [110] orientation are shown. The 3s and 3p orbitals, which are the valence states of Si, are inserted at the atomic positions.

The inelastic image for K-shell ionisation is given by the atomic potentials and is peaked at the atomic positions. For L-shell ionisation delocalization is expected to be more pronounced for the dipole transitions.

Delocalization of the beam is not influenced by a small tilt of the specimen out of the optical axis, because channeling forces the electrons to funnel along the potentals [67]. Using a not abberation corrected TEM/STEM as the TECNAI F20 ST the minimum probe diameter is determined by $d = C_s \cdot \alpha^3$ where α is the convergence angle and C_s represents the spherical abberation constant of the objective lens, which is 1 mm in the described electron microscope. Using an angle of 5 mrad, the minimum beam diameter would be 1.5 Å. This is not small enough to resolve the dumbbells in Si (110) properly, but good enough to position the beam either on an atomic column or inbetween two pairs of dumbbells. Figure 3.13 shows an unprocessed high resolution STEM (HRSTEM) image acquired with an high angle ADF (HAADF) detector. The black circles mark the positions of EELS measurements. The left and middle position are on top of atomic columns, whereas the right one is inbetween two pairs of dumbbells. Beam broadening is in this case not a limiting factor because plane-wave multislice calculations [10] show that the probe propagates along the atomic column as shown above. The collected information will be very localized. The limitation of resolution is the convolution of the probe function with the inelastic object function.

Specimen drift was minimized by inserting the sample into the TEM three days before the measurements were done. This guaranteed that specimen and TEM were in thermal equilibrium. Morover, the experiment was performed during the night to have no mechanical vibrations due to traffic or human beings from inside the building nor having influences from moving elevators or underground trains which pass the laboratory building less than 300 m away during the day. As shown above the more localized the inelastic object function is, the higher would be the EELS intensity at the atomic column position. The more delocalized the inelastic object function is, the higher would be the EELS

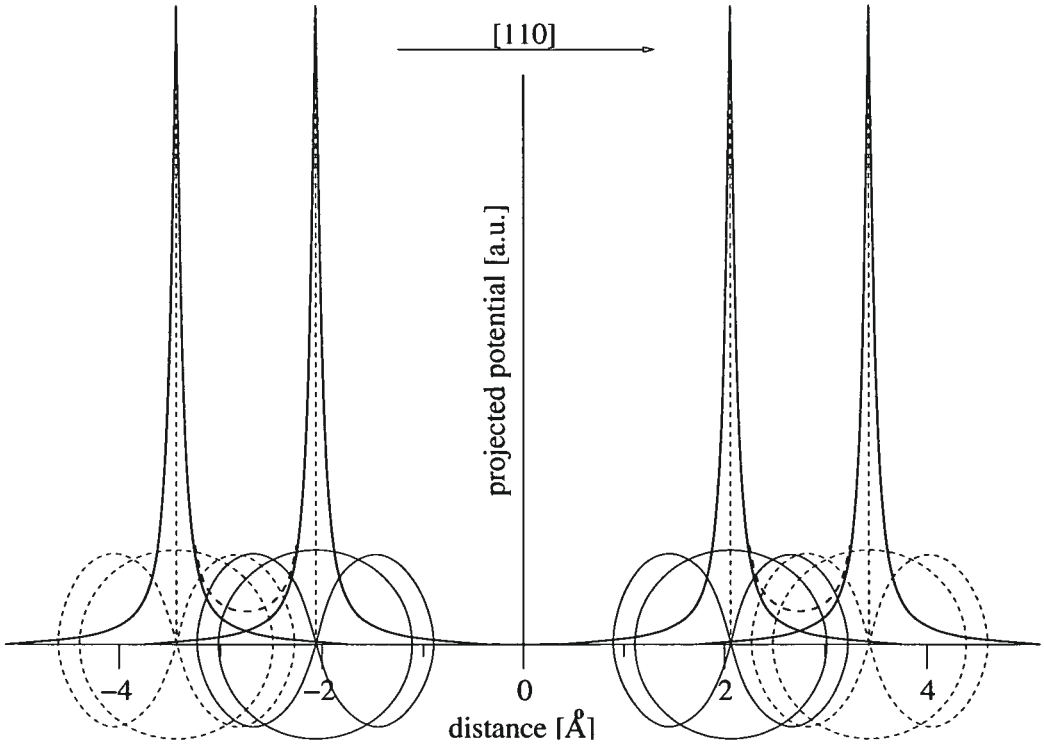

Figure 3.12: Projected potentials of two Si dumbbells in [110] oreintation. The extension of the 3s and 3p states are also shown as circles and dumbbells, respectively.

intensity between the atomic column positions. The shell radius of Si 3s states is 0.951 Å and for the 3p states the radial extent of the electron orbital is 1.151 Å. For the Si-L_2 edge this means that the monopole transitions at 99 eV energy loss should be more pronounced at the atomic column positions. The EELS intensities at 120 eV where we observe predominantly dipole transitions should therefore be higher between the atoms.

But much stronger should be the effect of parity change in the Si-L_2 edge [68, 69]. As a direct consequence of parity conservation "scatterer + probe electron" a transition with wave vector transfer q shifts the phase of the electron in the opposite direction than one with $-q$. Since dipole allowed transitions undergo a change in parity of the atom, the probe electron is also forced to. A plane wave coming down the optical axis has even parity with respect to the axis, after exciting a dipole allowed transition its parity is odd, leading to destructive interference of wavelets along the symmetry axis. This would lead to a ring shaped inelastic image of a Si atom in the 120 eV energy loss using a large collection aperture [70].

For the experiment the above described conditions were chosen, this means that the probe size was 1.5 Å and the collection angle β was set to be 19.52 mrad which can be applied when the 2 mm spectrometer entrance aperture is inserted and a camera length of 30 mm is used. Figures 3.14 and 3.15 show the EELS spectra after background subtraction using a power-law fit. Table 3.2 gives the ratios of the intensities at 100 eV and 102 eV and the intensity value at 120 eV.

The Si-$L_{2,3}$ edge can be calculated with the *Wien2k* code [71]. Unfortunately, due to numerical lim-

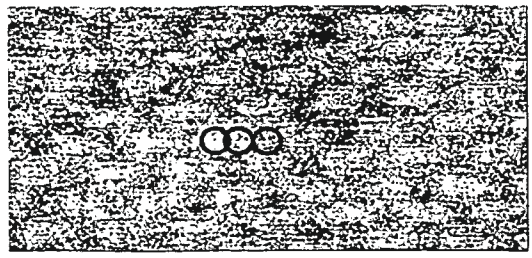

Figure 3.13: Unprocessed HRSTEM image of Si (110) acquired with the TECNAI F20 ST (without C_s corrector). The three different kinds of positions for EELS measurements are marked with black circles.

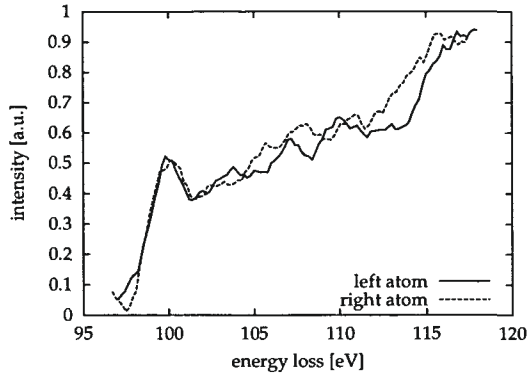

Figure 3.14: Si-L_2 edge of left and right atom of a dumbbell in Si (110) after background subtraction. The spectra are identical. The intensity ratio of the peak at 100 eV and the minimum at 102 eV is 1.45 ± 0.05.

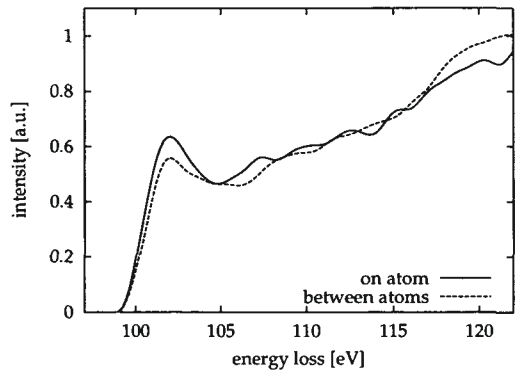

Figure 3.15: Si-L_2 edge of an Si atom and from inbetween two pairs of dumbbells after background subtraction using $\beta = 19.52$ mrad. The spectra show differences in the 100 eV energy loss peak. The ratio of the peak at 100 eV and the minimum at 102 eV of the EELS recording between the atoms is 1.3 ± 0.21.

Table 3.2: Ratio of intensities at 100 eV (a) and 102 eV (b) and the intensity of the 120 eV energy loss for the different positions of measurement using $\beta = 19.52$ mrad. The spectra were normalized so that the 120 eV value (I_{120}) is 1 for the recording from inbetween the atomic columns.

position	a/b	I_{120} [eV]
left atom	1.40 ± 0.05	0.93 ± 0.005
right atom	1.40 ± 0.05	0.93 ± 0.005
between atoms	1.3 ± 0.21	1.00 ± 0.005

itation within the dipole approximation where the initial 2p statesare not completely confined within the atomic spheres (AS), the program would lead to unphysically large monopole contributions when calculating the overlap integral between the radial parts of the initial (2p) and final (p) wave functions within the AS [72].

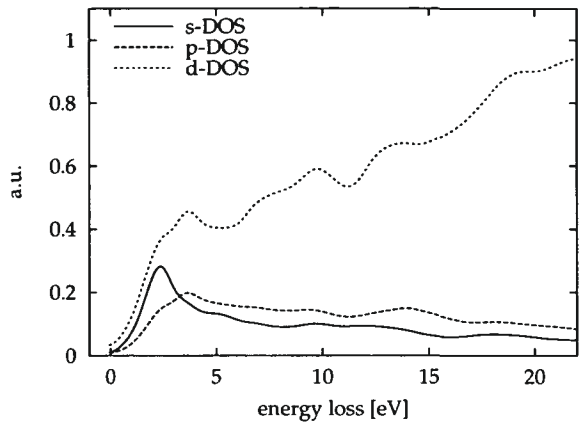

Figure 3.16: s-, p-, and d-DOS of silicon with 0 eV as the Fermi level. The p-DOS representing the monopole transitions is scaled to fit the experiment best.

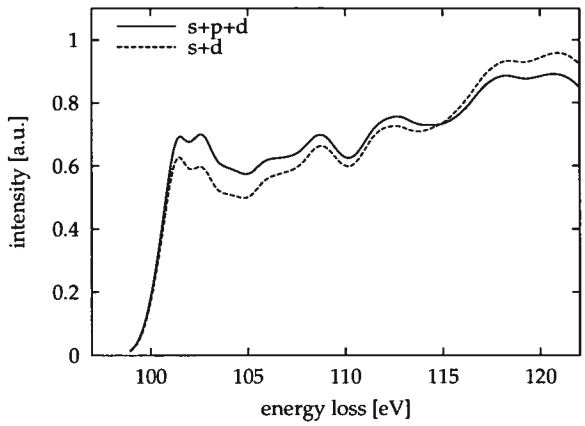

Figure 3.17: Si-$L_{2,3}$ edge simulation using the s- and d-DOS (dipole terms), and the s-, p- (monopole term), and d-DOS. Only the tendency is directly comparable with fig. 3.15

However the Si-$L_{2,3}$ edge can be calculated within the dipole approximation and the correct ratio between the two dipole contributions 2p → s and 2p → d retrieved. Fig. 3.16 shows the s-, p-, and d-DOS. The s- and d-DOS were scaled to their respective contributions in the dipole allowed ELNES. The p-DOS was scaled to an arbitary value giving good agreement with the experiment recorded on atomic sites (figs. 3.15 and 3.17). The monopole transitions represented by the p-DOS of course increase the peak at 99 eV energy loss but on the other hand when matching both curves at 115 eV the intensity ratio at 120 eV has changed.

From the above text it is clear that with the chosen collection angle two effects play a major role on the ELNES of the Si-L edge: (1) the localization effect and (2) the parity change of the probe electron. When increasing the collection angle β the localization effect will also increase [64] but the parity effect will decrease [68] and the other way round. This means that the localization effect can be

effectively supressed when using a small spectrometer entrance aperture. Only the parity effect will influence the result. When selecting a larger β, the parity effect can be reduced. This was done in Fig. 3.18. When reducing the collection angle β from 19.53 to 5.81 mrad the signal-to-noise ratio (SNR) increases significantly, since the total incoming intensity is reduced by a factor of 0.09. Therefore the spectra recorded with small β in Fig. 3.18 are very noisy. On the other hand increasing the size of the spectrometer entrance aperture leads to a decrease of energy resolution. Therefore the spectra were deconvolved using the method described in [48]. This assures that the spectra can be compared directly. In Fig. 3.18 spectra from the atomic column positions and from in between the

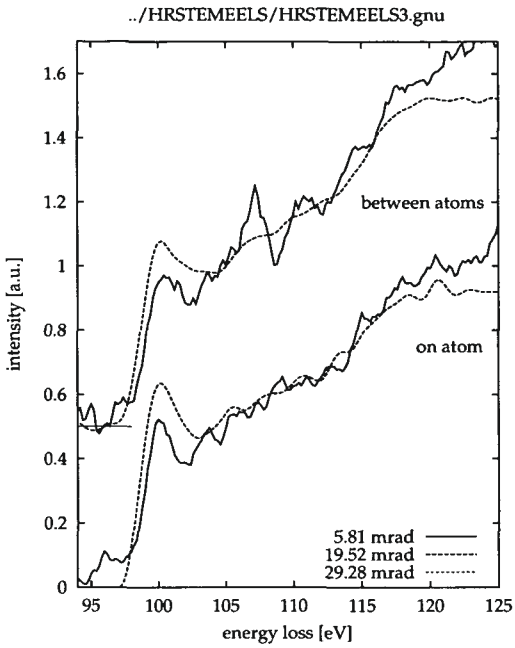

Figure 3.18: Si-L_2 edge of an Si atom and from in between two pairs of dumbbells after background subtraction using different values of β.

atomic columns are shown. The tendency is clear: decreasing β leads to a stronger increase of the 120 eV signal than for the 100 eV signal. This means that even with uncorrected STEMs, atomically resolved EELS measurments can be obtained. Even if delocalization would lead us to suspect to equal out any differences in EELS spectra recorded on and off atomic sites the parity conservation of the "probe + scatterer" system can lead to strong differences in the observed ELNES. Therefore ELNES interpretation of atomically resolved EELS spectra will be even more difficult for EELS acquisitions using a C_s-corrected STEM as for conventional energy loss investigations.

Chapter 4

Model for the Layer Exchange Process

The Aluminium induced layer exchange (ALILE) process is the basis on which this special method of solar cell production is based upon. Therefore it is necessary to analyze how this process works. As described in chapter 1.2.3, the layers exchange their positions during heat treatment. We can subdivide the ALILE process into four parts: (a) the solution of amorphous Si by Al, (b) diffusion of Si in the Al layer, (c) crystallization and (d) diffusion of Al out of the lower layer.
In this chapter all four parts are discussed and experimental observations are shown. First a look is taken at the Si solution in Al, under consideration of Hiraki's "screening model" [73]. Next a discussion on several diffusion processes taking place during layer exchange is added leading to crystallization and further to the final question: how does the Al go to the top layer?

4.1 The Screening Model

The diffusion of Si atoms trough the metal of a simple eutectic metal/Si system and subsequent crystallisation have widely been accepted as the basic process of metal induced crystallisation [74]. Nevertheless, little is known about the actual dissociation mechanism of the amorphous silicon by the metal. The overall driving force behind crystallisation is the reduction of Gibbs energy by the transformation of amorphous to crystalline silicon (0.1 eV/atom [75]). However, the covalent Si-Si bond is relatively strong with about 2 eV per bond. The activation energy of solid state phase crystallisation (SPC) of pure a-Si material is very high and amounts to about 3-4 eV [76]. This causes formation of poly-Si by SPC to be slow even at temperatures above 600C. It further shows that aluminum induced crystalization is of a significantly different nature than SPC. In contrast, crystallisation of a-Si when in contact with Al occurs at much lower temperatures, is faster and has a lower activation energy. The reported activation energy varies between 0.8 eV and 1.2 eV [77]. The activation energy of the ALILE process is 1.3 eV as determined in [74].
The question is therefore, how the metal reduces the energy required to break the Si-Si bonds prior to any diffusion process. There are two main models that propose a dissociation mechanism of the amorphous silicon in spite of the covalent Si bonding, Tu's "interstitial model" [78], and Hiraki's "screening model" [73]. Tu's model is based on an interstitial intermixing of the metal and silicon atoms at the

interface. It is proposed that the metal jumps into the Si, forming metal interstitials. But there is no physical reason for jumping, it must be random like. Therefore the present investigations focussed on an experimental verification of Hiraki's "screening model". It postulates that weakening of Si-Si bonds at the metal/Si interface is due to the ability of the metal to screen the Colomb interaction by its mobile free electrons. This screening effect results in a non-metal to metal-like bonding of the adjacent semiconductor material over the region of some monolayers. Hiraki's model is based on calculations showing a band closure of the energy bandgap of semiconductors applying manybody techniques to interface calculations [79].

4.1.1 Metal induced gap states

In section 2.3 the accuracy of bandgap measurements was shown with the instrumental set-up of Vienna University of Technology. Therefore EELS investigations for proving Hiraki's "screening model" were performed. For this purpose the electronic point of view is interesting, when looking at a metal/Si interface, because this is the well known Schottky contact. During the past decades the understanding of Schottky barriers at the metal-semiconductor interface has made considerable progress [80, 81, 82]. It is well known that, when a contact is made between a metal and a semiconductor, there is a potential barrier Φ. The Fermi level E_F at the surface of the semiconductor lies in the energy gap at a point ξ above the top of the valence band [83].

$$\Phi = E_g - \xi \tag{4.1}$$

with [80]

$$\xi = \xi_0 + 0.13(\phi_{sc} - \phi_m) \tag{4.2}$$

where ϕ_{sc} and ϕ_m are the workfunctions of the semiconductor and the metal, respectively. The remarkable thing is, that ξ is constant to within 0.2 eV. Furthermore, ξ is roughly a constant fraction 0.3 of the energy gap. For the system Al-Si ξ is therefore 0.3415 eV. In figure 4.1 the definition of Φ and ξ at a metal-semiconductor junction are shown.

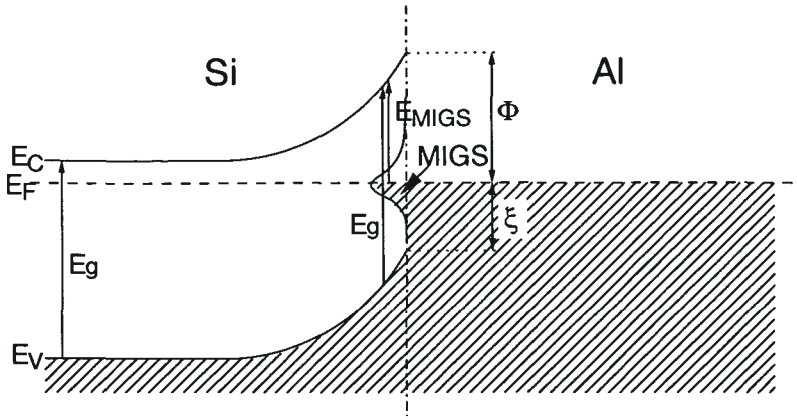

Figure 4.1: Band structure of a Schottky contact between Si and Al. Φ represents the barrier height and ξ defines the position of the Fermi level with respect to the upper most valence band of Si.

Values for the barrier height Φ can be found in [84, 85] where they have been determined theoretically and experimentally to be 0.76 eV and 0.7 eV, respectively. For an energy E in the gap of the semiconductor, the solutions of the Schrödinger equation will decay exponentially in the semiconductor but propagate as Bloch states on the metal side of the junction to form the volume states of the metal [86]. This follows from a simple consideration of matching the two wave functions at the boundary. More detailed explanation is given in [80]. The Fermi momenta of Al and Si are nearly equal ($k_{F,m}/k_{F,sc} = 0.97$) [80], therefore the charge density $\rho(E)$ in the semiconductor tails of the metal wave functions can be estimated. Under more realistic assumptions [80], the maximum of $\rho(E)$ is located close to the center of the gap. The charge density distribution calculated in this way represents the metal induced gap states, located around E_F, filled below and empty above the Fermi energy. Moreover the length of the tails increase with decreasing gap width and is estimated to be 8 Å for the Al-Si junction. This leads to the conclusion that metal-semiconductor-metal devices cannot be reduced to half a dozen monolayers of the semiconducting material, because semiconducting properties will be lost with decreasing thickness. Today's analytical instruments can reach such a spatial resolution, so that an atomistic verification of the MIGS model can be performed. This was first done by measurements of the silicon $2p_{3/2}$ core absorption as a function of position near the Al/Si(111) interface [87]. There the core transitions to the unoccupied metal induced gap states above Fermi energy have been detected (see Fig. 4.2). Nevertheless the metal induced gap states were not observed directly before, implying that the reduction of gap with by ξ was not detected in dependence of distance from the Al/Si interface before. With todays' energy resolution and deconvolution methods, the transitions from the metal induced gap states (MIGS) to the lower conduction band of the semiconductor can be observed very close to the interface. The energy loss in this case is defined in figure 4.1 as E_{MIGS} which is roughly equal to Φ.

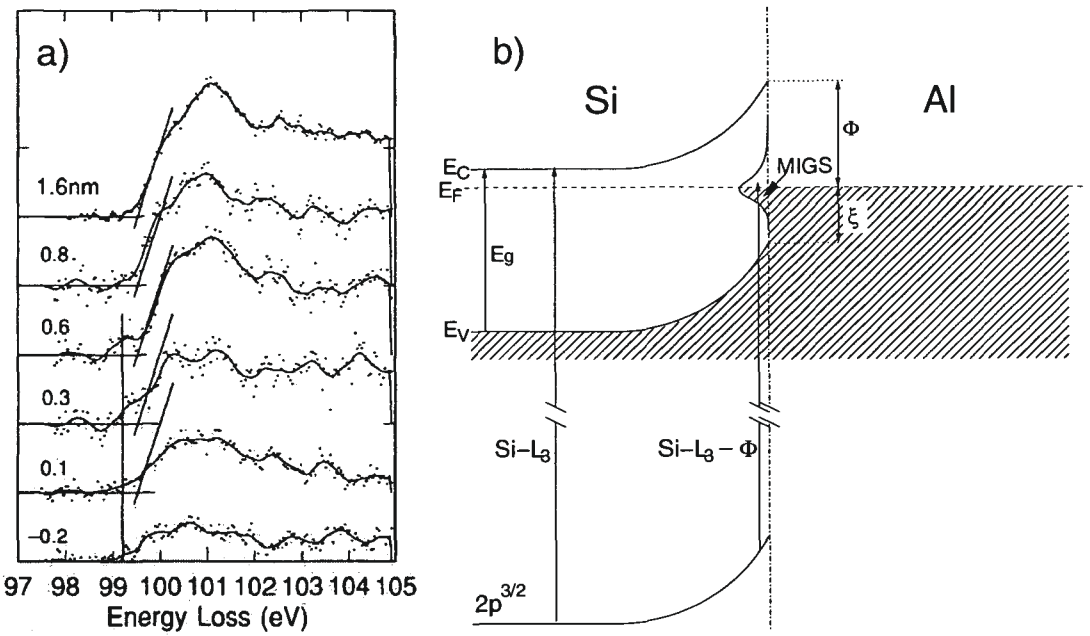

Figure 4.2: a) EELS results from [87]. The Si L_3 edge has been measured at several distances from the Si/Al interface. b) band scheme and the observed transitions for this case.

The instrument used for low loss detection was a TECNAI F20 transmission electron microscope (TEM) with scanning unit (STEM) operated at 200 kV acceleration voltage. The extraction voltage of the field emission gun (FEG) was reduced to 3 kV for decreasing the energy resolution of the energy loss spectrum. The spot size was chosen to be 4.3 Å. This is a compromise for detecting the MIGS between spatial resolution and supplying enough intensity for a good deconvolution of the elastic peak (see section 2.3). The used convergence half-angle was 10 mrad, the spectrometer collection half-angle was 4.4 mrad giving an energy resolution of 0.7 eV full width at half maximum (FWHM) in the zero loss peak (ZLP). The difficulty is not to measure the value of the edge onset from the MIGS-to-conduction band transition because the ZLP is so close. The main problem is stemming from the tails of the ZLP. Accuracy can only be assured when the shape of the ZLP in the spectrum is very precisely equal to the one measured separately in a hole of the specimen under the same conditions (see again section 2.3). Experiments were performed in STEM mode and in nanoprobe mode. Both leading to the same results as shown later on in Fig. 4.6.
The investigated specimens were produced by means of aluminium induced layer exchange (ALILIE). This means that first a polycrystalline Al layer is deposited onto a glass substrate. After a short time of oxidation amorphous Si is deposited on top. During the following heat treatment the Al and Si layers change positions keeping the oxidised Al as a membrane in between. This process is described more detailed elsewhere [74, 88] and is used as a step in solar cell production [89]. When the layer exchange process is stopped during heat treatment, two polycrystalline layers are formed containing both, Al and Si as small grains with some 100 nm in size. For the presented investigations many such interfaces were investigated having no preferential orientation. Using energy filtered TEM (EFTEM) the flatness of the interface was determined. All selected interfaces could be oriented nearly parallel to

the electron beam of the microscope using the α-tilt only, because a single tilt holder was used. This guaranteed no specimen drift during acquisition. Nevertheless a spatial extinction of the MIGS cannot be determined this way.

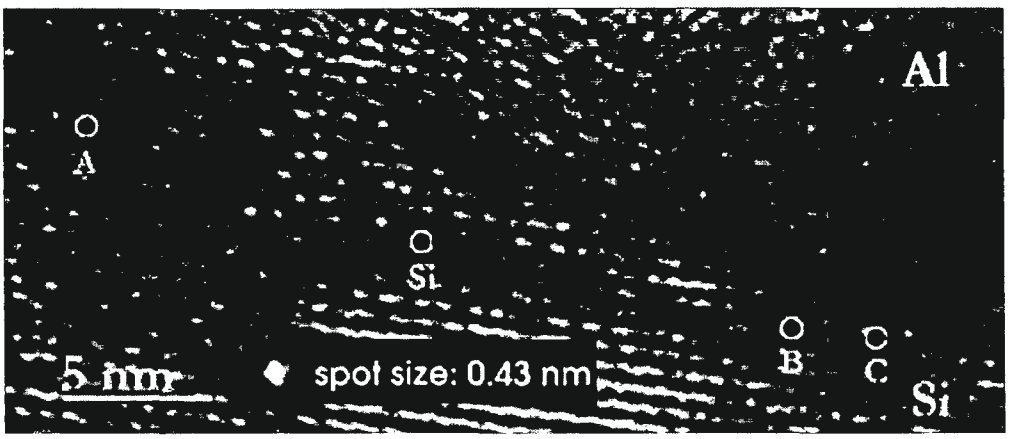

Figure 4.3: Positions of measurement for bandgap determination. The inset shows the spot used for EELS investigations.

Figure 4.3 shows the positions of measurement during the work in nanoprobe mode. The distance between the measurements and the interface must be smaller than 8 Å, otherwise no MIGS could be observed, but it is impossible to measure the distance exactly. This is because the interface is not flat on an atomic scale as is was not produced for such investigations. But from the position of the plasmon maximum, we can estimate, that position C is closest to the interface and position A is most distant (see table 4.1).

Table 4.1: Energy values of the maxima in the plasmon loss from measurement positions shown in Fig. 4.3. The theoretical value from [84] fits the experiments best. Very similar values can be found in [85].

position nr.	plasmon energy [eV]	gap width (measured/theory) [eV]
Si	16.70	1.15/1.12
A	15.10	0.82/0.76
B	15.05	0.81/0.76
C	15.00	0.81/0.76
Al	14.95	– / –

The plamon peak maxima of A, B, C are very close to the value found for pure Al. This is due to the delocalisation phenomenon described in [90, 36]. Because the Al-plasmon is a very sharp feature in the EEL spectrum compared to the Si-plasmon, even a small contribution to the superimposed spectrum shifts the maximum strongly close to the maximum value of Al-plasmons. The given values of the gap width were determined by linear fits in the edge onset and have an accuracy of ± 0.05 eV.
The EELS spectra in Fig. 4.4 are pertaining to the positions shown above. One sees an increase of the first feature starting at 0.8 eV from A to C. In measurement A only a small fracture is coming from

MIGS because the interface is far off from being oriented parallel to the beam. Therefore the cross section for the MIGS is rather small and most of the signal is related to pure Si.

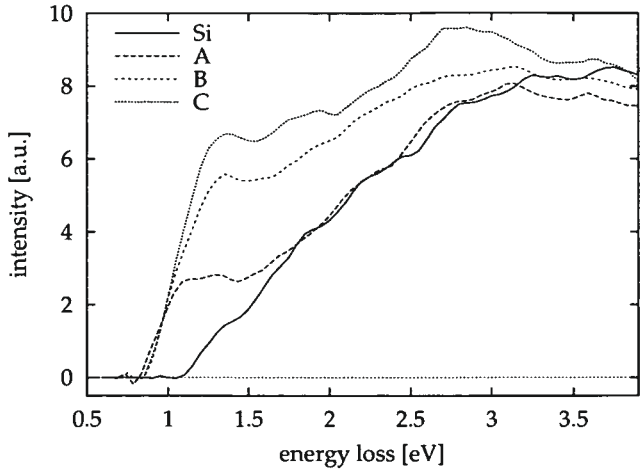

Figure 4.4: ZLP deconvolved low loss spectra from positions Si, A, B and C as described in Fig. 4.3. The edge onset at 0.8 eV, which is exactly the Schottky barrier height Φ, increases with decreasing distance from the interface.

The edge onset at 0.8 eV can only be found very close to the interface and is therefore identified as metal induced gap states. It corresponds exactly to Φ in Fig. 4.1. Because EELS maps the unoccupied density of states above the Fermi level, the transitions from the occupied gap states below E_F to the bended conduction band of the semiconductor are observed. When subtracting all contributions from the region of the specimen containing no MIGS - and due to the fact that the dimension of the spot is 4.3 Å in diameter and the interface is not flat the signal contains such contributions - only the transitions from metal induced gap states to the conduction band can be shown. This is done in Fig. 4.5.

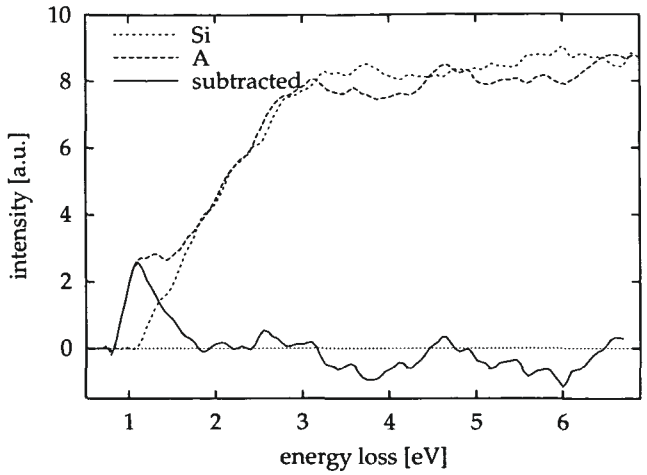

Figure 4.5: The subtraction of the Si post bandgap signal from the EEL spectrum acquired at position *A*

As a proof of the accuracy of the measurements, Fig. 4.6 shows a repetition of the experiment on a different day, with a different specimen produced with ALILE, too, and in STEM mode.

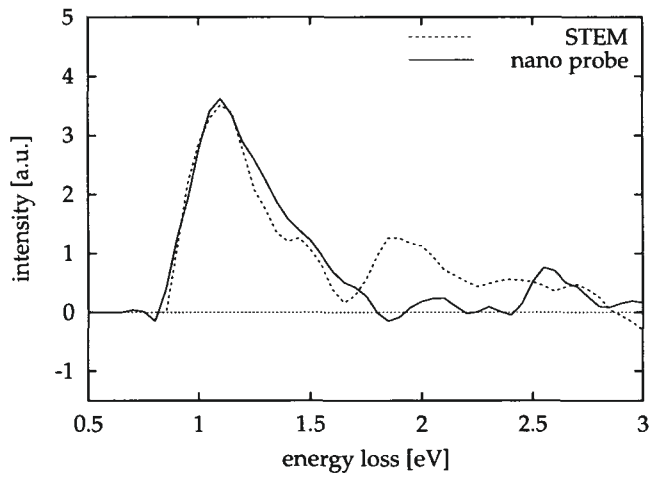

Figure 4.6: Comparison from different measurements from different specimens, acquired at different days with different TEM operation modes but both with a spot size of 4.3 Å and equal gun lens and filter settings.

Concluding one can state, that Batson's research [87] and the present work can be seen as supplementary investigations of the MIGS at the Al/Si Schottky contact, because Batson probes the $2p_{3/2}$ to metal induced gap states above E_F transitions and in this paper the MIGS below E_F to conduction band transitions in Si are investigated. The barrier height of the contact is measured in both works to be in the range of 0.69 - 0.82 eV. The extinction of the MIGS cannot be measured with the used setup but an upper limit can be given with 10 Å, because measurement *Si* in Fig. 4.3 is not far off

the interface.

4.2 Nucleation and Crystal Growth

Besides diffusion processes, nucleation of Si in Al must be studied. It is not aim of this work to deal with nucleation, because it would go beyond the scope of this thesis, nevertheless a short description for this problem is given below.
Solid state phase transformations are generally the outcomes, both for isothermally and non-isothermally conducted annealings, of two often simultaneously operating mechnaisms: nucleation and growth. One strives for determination of the kinetic parameters of theses processes from the overall kinetics. Let us therefore first consider different nucleation and growth models. Four such models are illustrated in Fig. 4.7.

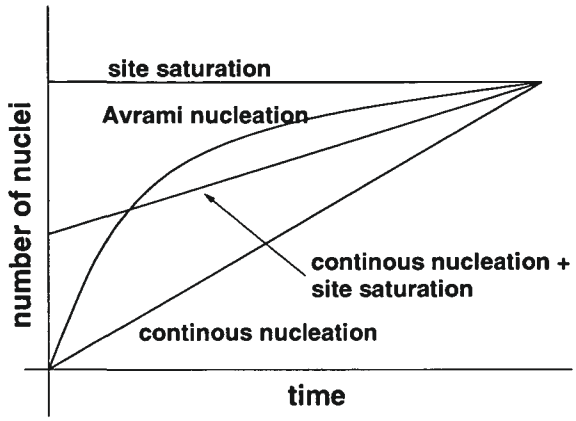

Figure 4.7: Schematic diagram of the number of nuclei as a function of time at a constant temperature for four different nucleation models.

From observation of growth during the ALILE process by using the light microscope at HMI Berlin, the site saturation model can be excluded. The number of new grains increases with time. It was found, that the number of new nuclei decreases with time so that the Avrami nucleation model [91, 92, 93] seems to be fitting the present case best.
The main difference between this model and the ALILE process is that the influence of the membrane cannot easily be included. The time where nucleation starts is strongly dependent on the membrane thickness and its compactness. Furthermore, the membrane undergoes a phase transformation from the amorphous to the crystalline phase (see section 5.1.2). But from that point on, when diffusion of Si through the membrane is regulated, a modified Avrami model can be applied.
During the classical crystal growth process more atoms arrive at a nucleus than are leaving it. The growth velocity can be written as $v_w = A \cdot exp(-Q/k_BT)$, with Q the energy needed for entering the nucleation compound and A is a proportionality factor. If x is the crystallized fraction and therefore $(1-x)$ is the fraction that is not crystallized and r is the length of a nucleus, it follows that $x = A \cdot r^3$. If the growth of the nucleus is diffusion dominated then one has $r = B \cdot \sqrt{t}$, and the nucleation growth

velocity can be written as $dr/dt = C \cdot (1-x)/\sqrt{t}$, where A, B, and C are proportionality constants. For time dependent crystallization one finds

$$\frac{dx}{dt} = \frac{dx}{dr} \cdot \frac{dr}{dt} = 3Ar^2 \cdot C \cdot \frac{(1-x)}{\sqrt{t}}. \tag{4.3}$$

If the following two assumptions are made : (a) nucleation rate is either zero (i.e. crystallization accurs due to growth of pre-existing nuclei) or constant, and (b) isotropical growth rate is proportional to either time t or $t^{0.5}$ (depending wether the crystallisation is interface or diffusion controlled), then the klassical Kolmogorov-Johnson-Mehl-Avrami (KJMA) equation can be derived to be

$$x = 1 - e^{-(K\cdot(t-\tau))^n} \tag{4.4}$$

with x denoting the volume fraction transformed at the time t, τ is the incubation time and n is the Avrami exponent which reflects the nucleation rate and/or the growth morphology. K is the kinematic parameter depending on the annealing temperature, nucleation rate and growth rate. The curve $x = f(t)$ is s-shaped (see Figs. 4.8).
In the ALILE case τ, n, and K strongly depend on the nature of the membrane. Detailed work on this can be found in [94] which is presently in progress and will be submitted to *Thin Solid Films*.

4.3 Diffusion Processes involved in ALILE

The next step in the ALILE process after Si solution is diffusion. In this section it is shown which diffusion processes are characteristic for the further seeding layer formation. We must distinguish between some different diffusion processes:

1. diffusion of dissolved Si atoms through the membrane
2. diffusion of Si atoms along the Al/membrane interface
3. diffusion of Si atoms at Al-Al grain boundaries (GBs)
4. diffusion of Si atoms at Si grain/Al interfaces
5. diffusion of Si atoms in Al grains

As one sees, the situation is very complex. For some diffusion processes only general statements can be made. One of those statements concerns the diffusion of dissolved Si atoms through the membrane. It is driven by the Si-concentration gradient between the Si and the Al layer. The latter has of course a lower concentration value throughout the whole exchange process. The retardation parameter for this process is clearly the consistency of the membrane. This will be dicussed later on in section 5.1.2.

4.3.1 A brief Introduction to Diffusion Theory

Let us first consider the flux of particles of a certain species in a one dimensional system with a concentration $c(\vec{x},t)$. One assumes that in the presence of a concentration gradient $\partial c/\partial x$, a flux of particles is established, directed along the (negative) concentration gradient, and that the flux of atoms is proportional to the concentration gradient:

$$J = -D\frac{\partial c}{\partial x} \tag{4.5}$$

where D is the diffusion coefficient or diffusivity. This law is called Fick's law and can easily be generalized for three dimensions using

$$\vec{J} = -\vec{D}\nabla\vec{c} \tag{4.6}$$

This law must be generalized if the flux is time dependent. Up to now it is only valid, if the flux is constant. In the time-dependent case Fick's law must be combined with an equation of material balance. For species which obey a conservation law, this is the equation of continuity:

$$\frac{\partial J}{\partial x} = -\frac{\partial c}{\partial t} \tag{4.7}$$

Inserting Eq. 4.7 into Eq. 4.5 one gets

$$\frac{\partial c}{\partial t} = \frac{\partial}{\partial x}\left(D\frac{\partial c}{\partial x}\right). \tag{4.8}$$

This can easily be generalized for three dimensions and be reduced to

$$\frac{\partial c}{\partial t} = D\nabla c. \tag{4.9}$$

If the overall ALILE process shall be described the second Fick's law can be solved using the following initial and boudary conditions:
We consider a constant surface concentration (which can be rectified, due to the fact that during the process always new Si material is placed at the disposal. For $t = 0$, the Si concentration in the Al layer vanishes: $c(x,0) = c_0 = 0$. During the whole process ($t > 0$) we have at position $x = 0$ a concentration $c(0,t) = c_s$. We can calculate

$$\frac{c}{c_s} = erfc(x/2\sqrt{Dt}). \tag{4.10}$$

where "erfc" is the complementary error function ($erfc = 1 - erf$) with

$$erf(z) = \frac{2}{\sqrt{\pi}} \cdot \int_0^z e^{-u^2} du \tag{4.11}$$

as the error integral of Gauss.
This model is discussed in detail in [74] but only describes the overall layer exchange process. But as mentioned in the introduction of this chapter, several different diffusion processes participate in the layer exchange process. A statistical approach is useful in this connection. If atoms impinge on a surface or interface, (the latter is the the case for the membrane/Al interface), the last distance before incorporation into a nucleus must be overcome in some way. This usually happens by means of diffusion. Therefore diffusion is the most important transport mechanism for the ALILE process.

Since diffusion is a stochastic process it is strictly connected to the Brown movement of atoms. Considering that a Brownian particle moves along a lattice distance a forward or backward in a short time range τ, the distance l covered after N time steps is:

$$l = \sum_{i=1}^{N} a\epsilon_i \tag{4.12}$$

with $\epsilon_i = \pm 1$ distributed randomly describing forward or backward steps of the particle, respectively. Therefore it is senseless to think in detail about an ϵ_i separately. But the expectation value is of interest. It is

$$\begin{aligned} < \epsilon_i >= 0 \\ < \epsilon_i \epsilon_j >= \delta_{i,j} \end{aligned} \tag{4.13}$$

and therefore

$$\begin{aligned} < l >= 0 \\ < l^2 >= a^2 \sum_i \sum_j \delta_{i,j} = Na^2 \end{aligned} \tag{4.14}$$

For movement in positive or negative direction during the time $t = N\tau$ we can calculate the mean distance from its starting point $\bar{l} \equiv \sqrt{< l^2 >}$. One therefore gets

$$\frac{\bar{l}(t)^2}{t} = \frac{a^2}{\tau} \tag{4.15}$$

as a relation independent of N. An increase of the distance between the origin of the movement and the present state by a factor of two therefore needs four times longer. This relation is not restricted to a one- or two- dimensional case but is valid in all dimensions since the fluctuation of atoms in all directions is independent of each other. The above described method (Eqs. 4.12 - 4.15) is a very common approach to deal with disorder. In principle it is based on the consideration that no correlation is present between the variables ϵ_i out in the time interval τ.

4.3.2 Si Diffusion at the Membrane/Al interface

Much more information is provided for the diffusion along the membrane/Al interface which is a hetero-interface. This process is the driving force for nucleation, because nucleation starts at this hetero-interface. A proof by means of focussed ion beam (FIB) imaging can be found in [74].
Nucleation can only start at points where the Si concentration is high enough. If too few Si atoms are accumulating, instable nuclei are formed which are dissolving again. Due to this fact we can consider a mean nucleation length l_n which is half the distance between two stable nuclei. From observation of the exchange process in the optical microscope the nucleation density and therefore the mean nucleation length can be measured. With this knowledge and other fundamental measurable values the hetero-interface diffusion can be described completely. The observables needed are nucleation density, temperature and time. Then the following model can be constructed:

$$l_n^4 = D_i/J \tag{4.16}$$

with D_i as the diffusion constant for the interface diffusion and J as the flux of Si atoms per unit area and time through the membrane. J can be calculated with

$$J = J_0 \cdot \xi \tag{4.17}$$

with J_0 as a virtual flux (which would be the total exchange of the whole volume within one second) and ξ as the temperature dependent parameter. J_0 is the Si concentration per cubic micrometer times the thickness of the layer d to be exchanged per second ($J_0 = 5 \cdot 10^{10} \cdot d$; $[\mu m^{-2} s^{-1}]$). In the crystallized fraction diagramme Figs. 4.8 ξ is represented by the increase of the curves in the linear range.

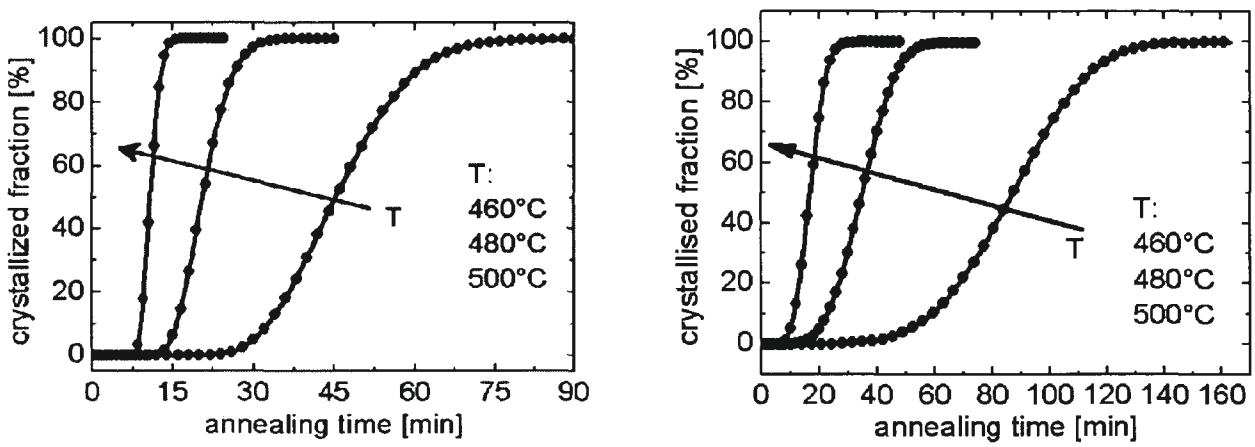

Figure 4.8: Crystallized fraction (CF) diagrams from specimen A02-093-3 and A04-103-1. Note the different time scales.

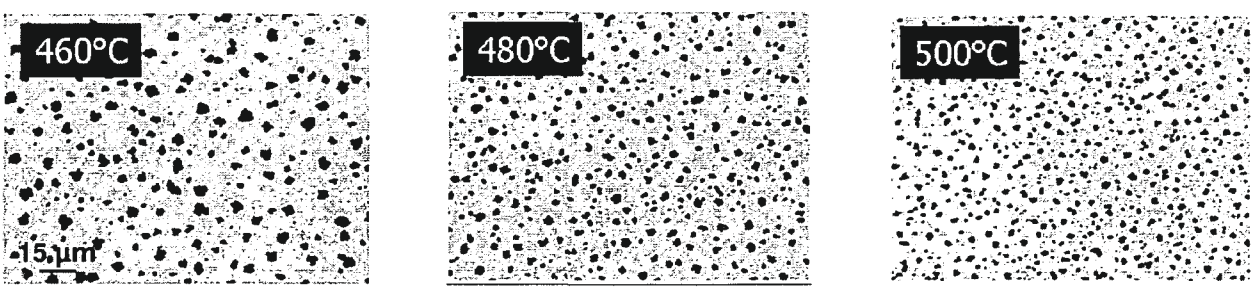

Figure 4.9: Images showing the nucleation density of specimen A04-103-1 at different temperatures.

l_n can be calculated from the images shown in figure 4.9. It can be shown that only for some time nucleation can be observed. After this time no new nuclei start to grow. This is because from then on always a nucleus can be reached from any positions beneath the membrane within the distance l_n. Due to the fact that the diffusion constant for interface diffusion can be written as

$$D_i = D_0 \cdot e^{-E/k_B T} \tag{4.18}$$

the activation energy E can be calculated from two curves in the CF-diagramme.

$$E = ln\left(\frac{(\frac{1}{2}\cdot\sqrt{\frac{A}{N_1}})^4\cdot J_0\cdot\xi_1}{(\frac{1}{2}\cdot\sqrt{\frac{A}{N_2}})^4\cdot J_0\cdot\xi_2}\right)\cdot\frac{k_B T_1 T_2}{T_1 - T_2} \tag{4.19}$$

One immediately sees that the virtual flux of Si atoms through the membrane cancels. It does not influence the diffusivity of the Si atoms in the hetero-interface. This seems very logical. In table 4.2 and 4.3 the experimental and calculated values are summed up for these two specific specimens. Further a mean capture time for nucleation t_c and a mean velocity of Si atoms in the interface v_i can be defined with

$$t_c = l_n^2/D_i \tag{4.20}$$

$$v_i = l_n/t_c = D_i/l_n \tag{4.21}$$

Table 4.2: Characteristic values of specimen A 02-093-3

$T(°C)$	$A(\mu m^2)$	ξ	N	$l_n(\mu m)$	$t_c(s)$	$v_i(\mu m s^{-1})$	$D_i(cm^2 s^{-1})$	$E(eV)$
460	10000	0.0537	148	4.11	0.88	4.661	19.174	
480	10000	0.1388	204	3.50	0.47	7.452	26.082	0.599
500	10000	0.3174	277	3.00	0.28	10.76	32.315	

Table 4.3: Characteristic values of specimen A 04-103-1

$T(°C)$	$A(\mu m^2)$	ξ	N	$l_n(\mu m)$	$t_c(s)$	$v_i(\mu m s^{-1})$	$D_i(cm^2 s^{-1})$	$E(eV)$
460	91000	0.0152	249	9.56	0.58	16.53	158.01	
480	91000	0.0595	416	7.24	0.26	27.97	202.49	0.451
500	91000	0.1361	613	6.09	0.16	38.47	234.31	

Comparing the tables above one finds that the activation energy E has decreased but the crystallisation time in the CF-diagramme has increased dramatically (fig. 4.8) by nearly a factor of two. The reason for this increase is the quality of the membrane. Which - as noted before - is retarding the flux and regulating nucleation. If the quality of the membrane could be controlled, the quality of the seed layer can be manipulated. This would lead to a higher density of (100)-oriented Si grains. This is discussed in detail in section 5.1.2. The decrease of the activation energy can be attributed to the vacancy concentration at the interface. This topic is treated in section 5.1.1.
For verification of this model, specimens were produced at which the layer exchange was stopped after some time. When cooling fast enough, a non negligible Si concentration underneath the membrane should be detectable in EFTEM. Figure 4.10 shows three elemental maps for oxygen, aluminium and silicon, respectively. The brighter the image features, the higher the concentration of the mapped element. This means that in the oxygen map only the alumina membrane is visible. Whereas in the Si map the a-Si layer and the diffusion path below the membrane is bright. Some brightness can be

found inside the membrane, too, coming from the L_1 edge of Al. This map can therefore not be used for Si quantification. The Al map shows the Al layer and the membrane relatively bright and a small diffusion zone of Al on top of the membrane. The Si diffusion zone below the membrane is dark in the Al map.

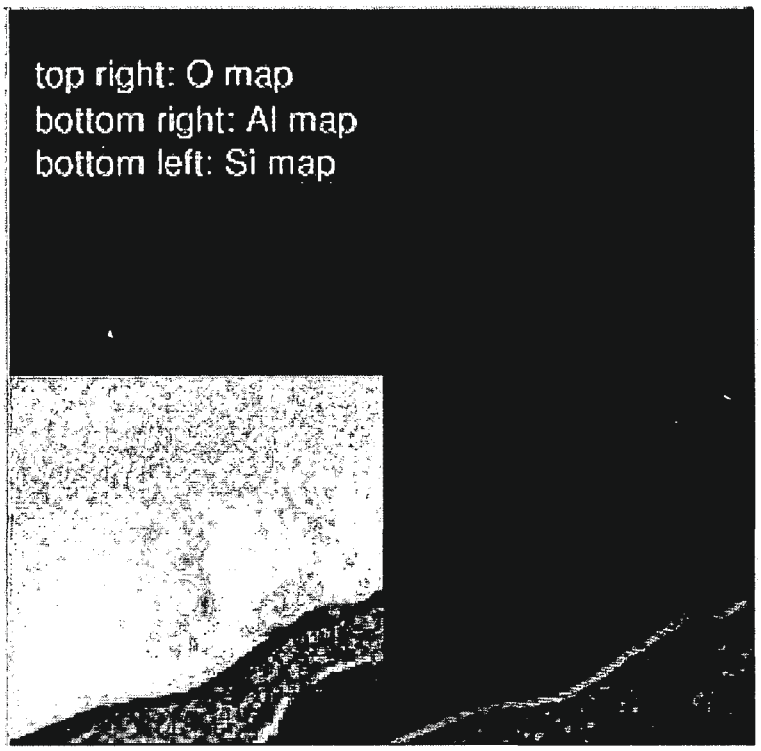

Figure 4.10: The three images show elemental maps for oxygen, aluminium and silicon. The Si map shows a high concentration below the membrane whereas the Al map shows a high concentration on top of the membrane. One sees, that Si is diffusioin at the Al/membrane interface whereas Al is diffusion along the membrane/a-Si interface.

Furthermore an EELS-line scan was acquired across such an interface to obtain a concentration profile. Figure 4.11 shows the position of measurement. Using ELNES separation the overlapping edges of Al, Al_2O_3 and Si were separated. Afterwards Si was quantified using the edge intensity compared with a Si-bulk spectrum acquired close by. This had to be done because all conditions (beam, column of the TEM and specimen thickness) had to be the same. The inset shows an elemental map of this position with Si (green), Al (red) and glass (blue), the line marks the position of the EELS line scan.

Figure 4.11: HAADF STEM image of the seeding layer of a specimen where the exchange process was stopped. The bad spatial resolution in the HAADF image is because of the fact that Al and Si are neighbours in the periodic table. There is nearly no Z-contrast. The inset shows an elemental map and the line across the interface denotes where the EELS line scan was recorded.

4.3.3 Si Diffusion at Al-Al Grain Boundaries

Describing the diffusion at Al-Al grain boundaries (GBs) is much more difficult because there are no direct observables. From the literature it is known that the activation energy for this process is a combination between GB-diffusion and bulk diffusion. This is because both are contributing to the overall diffusion in a small grained system. For the present grain sizes, which are of the order of 100 - 200 nm diameter, the mean activation energy is 0.8 eV. [95]. Our experimental efforts on the study of GB-diffusion was condemned to fail, because the setup for the layer exchange has not the possibility to freeze the exchange process at a given time. The only possibility is to cool down the sample before the layer exchange has finished. This cooling is not fast enough so that the atoms have enough time to nucleate. The concentration of dissolved Si atoms in the Al layer (crystals and GBs) is strongly dependent on the temperature of the system.
The nucleation during the cooling process takes place at the GBs. Easier at positions where three or four boundaries meet in a single point. When looking at such a nucleus, as done in Fig. 4.12.

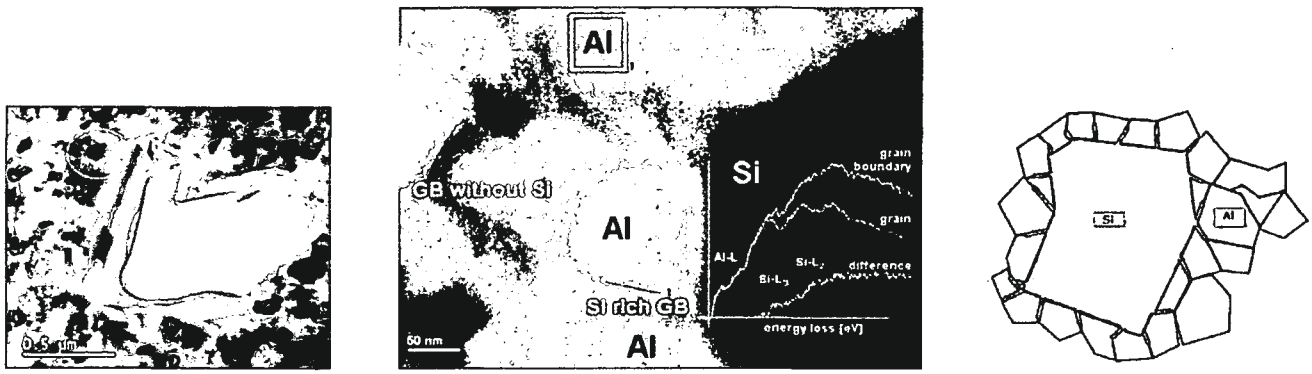

Figure 4.12: TEM bright field image (left), HAADF image (middle) and shcematic model (right) of a Si nucleus. In the HAADF image the lines where an EELS line scan was recorded are shown. The square marks the Al grain wherefrom the Al spectrum was acquired.

Several GBs were investigated by means of EELS. Only the GBs touching the Si nucleus, which arises from Si soluton during the cooling process, contain Si within the detection limits of EELS. The other GBs do not. The inlay of the HAADF image shows the spectra of the marked GB, the one from the Al grain and the scaled difference between them using ELNES separation. The Si-$L_{2,3}$ edge is clearly visible in the separated spectrum. Such GBs still contain Si.

4.4 Limitations for ALILE

The limits for the ALILE process can be subdivided into two parts: the limitations of the supply of Si atoms and the limitation on the removal of Al atoms.

4.4.1 Limitations due to the Supply with Si

In this subsection we demonstrate that the ALILE process when using a membrane is driven by the supply of Si through the membrane. In analogy to Eq. 4.18 the flux can be written as

$$J = J_0 \cdot e^{-E_j/k_B T} \tag{4.22}$$

with E_j is the activation energy for the flux of Si atoms through the membrane. Inserting Eq. 4.18 and 4.22 into Eq. 4.16 one finds a temperature dependency of l

$$l(T) = \left(\frac{D_0}{J_0}\right)^{1/4} \cdot e^{\{-1/4k_B T \cdot (E_D - E_j)\}}. \tag{4.23}$$

If $E_D > E_j$ the exponent will be negative and vice versa. This means that the layer exchange process is driven by the diffusion of Si, or the other way round, respectively. In the present situation — as described in tables 4.2 and 4.3 — when plotting l one sees that $l(T)$ decreases with increasing

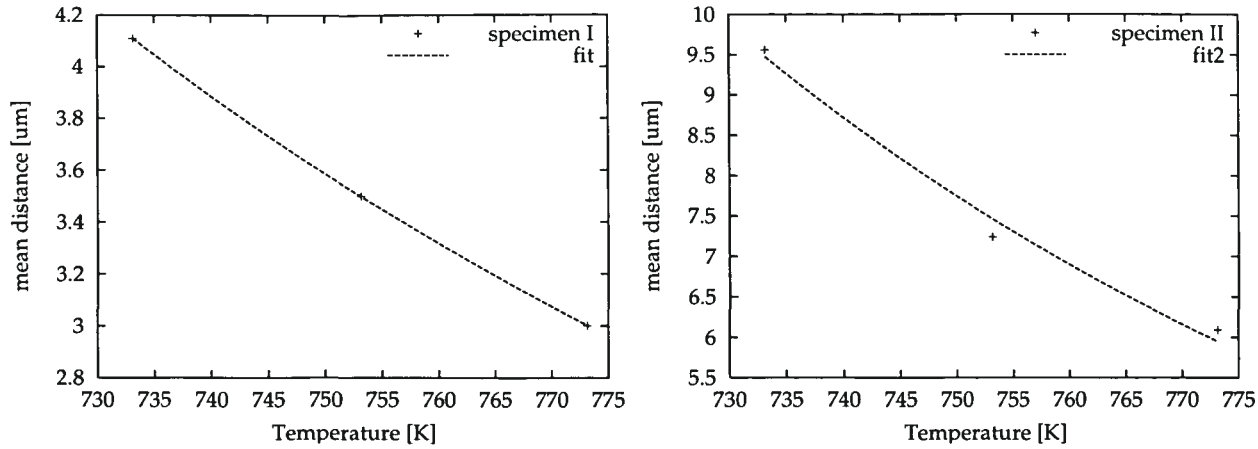

Figure 4.13: Temperature dependences of l_n.

temperature. Figure 4.13 shows the RMS-fits through the data points for the mean distance between two nuclei using Eq. 4.23. The energy difference $E_D - E_j$ in the exponent of Eq. 4.23 is -1.44 eV for specimen I and -2.14 eV for specimen II, respectively. This means that E_D is smaller than E_j and the ALILE process is driven by the supply of Si, which is the flux through the membrane, because diffusion is faster than the supply.

4.4.2 Limitations due to Diffusion of Al

Since Al moves into the upper layer its diffusion may also be described with an equation similar to Eq. 4.18.

$$D_{Al} = D_{Al,0} \cdot e^{-E_{Al}/k_B T} \tag{4.24}$$

Using this description, four possibilities arise for the ALILE process as illustrated in figure 4.14.

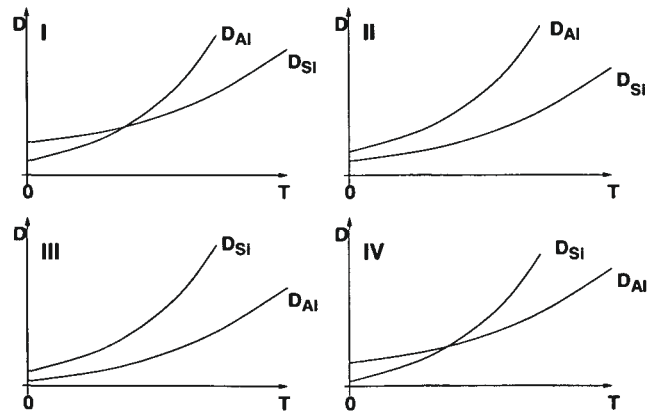

Figure 4.14: Different cases for comparison of Al and Si diffusion in the Al layer.

The parameters of the four cases which can be distinguished are listed in table 4.4.

Table 4.4: Parameters for the four cases illustrated in Fig. 4.14.

case	$D_{Si,0}$, $D_{Al,0}$	E_{Si}, E_{Al}
I	$D_{Si,0} > D_{Al,0}$	$E_{Si} < E_{Al}$
II	$D_{Si,0} < D_{Al,0}$	$E_{Si} < E_{Al}$
III	$D_{Si,0} > D_{Al,0}$	$E_{Si} > E_{Al}$
IV	$D_{Si,0} < D_{Al,0}$	$E_{Si} > E_{Al}$

From figure 4.14 it is clear that in case IV the ALILE process would not work, because the Al atoms would move slower than the Si atoms. This would lead to a compact crystalline layer directly below the membrane stopping any further layer exchange. The same problem would appear in case III above a certain temperature (where the graphs for the diffusion constants cross each other). In case I and II the ALILE process would work, unlimited in case II and limited by a minimum temperature in case I, respectively. Observations showed that ALILE works best immediately after layer deposition. If the tempering process is performed after some time lag of a view days the layer exchange works not so well, leaving much Al islands in the seed layer. This indicates that the layer exchange process starts even at room temperature. Since the diffusion velocities are too slow for a complete exchange, a small portion of Si diffuses in forming an additional crystalline diffusion barrier below the membrane. From these observations it seems that case II or case I with the crossing point below room temperature are the realistic ones. This of course needs further investigation.

4.5 Influences of Diffusion on the Exchange Process

As shown in the previous chapters, diffusion plays a major role in the ALILE process. Several diffusion paths are contributing dominantly to the layer exchange. A major role is played by the membrane. Alltogether the tendency for improvement of the ALILE process goes to adding impurities into the Al-layer during its deposition by using a worse base pressure. This leads to a higher defect concentration in the grain boundaries and at the interface between the Al-layer and the membrane which increases the velocity of diffusion along these paths.

4.6 ALILE on a Mo back contact

Another important experiment for solar cell construction was to perform ALILE on a polycrystalline Mo back contact. In the following section, the results of TEM investigations are shown. For this purpose a specimen was prepared by etching the Al layer off and then a TEM cross section was grinded and ion milled. Using Z-contrast conditions (HAADF-STEM) one sees that the layer system after layer exchange is not glass/Mo/pc-Si/membrane/Si islands. Instead we find a interlayer between Mo and pc-Si containing Al with a little bit of Mo (see figure 4.15).

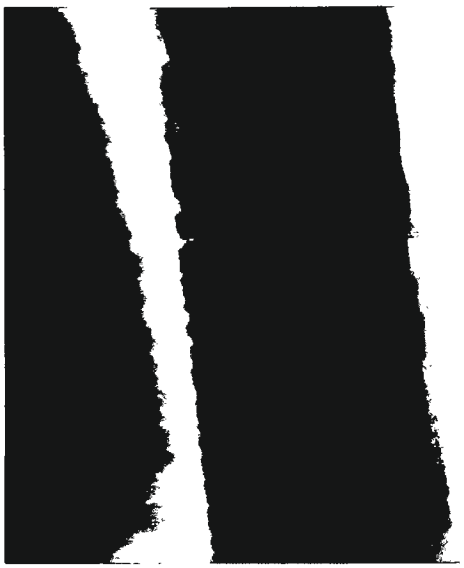

Figure 4.15: Z-contrast image of the "ALILE on Mo" specimen.

EELS investigations showed that the maximum of the Al plasmon of the interlayer is shifted up to 15.6 eV energy loss. Furthermore, Z-contrast shows a brighter contrast as for the Si layer but Al is a little bit lighter than Si. Therefore one would expect the inverse contrast. But due to the fact that the Al-layer is not pure Al but some kind of Al-Mo alloy, the brightness of this layer is higher as the one of the Si layers. On the other hand, the Al_2O_3 membrane seems to keep stable, even if the Al(Mo) alloy surface it rather rough. Having a closer look (figure 4.16) one sees that the membrane is cracked in many positions. This does not constitute a serious problem, because the surface would be flattened by means of chemical-mechanical-polishing (CMP).

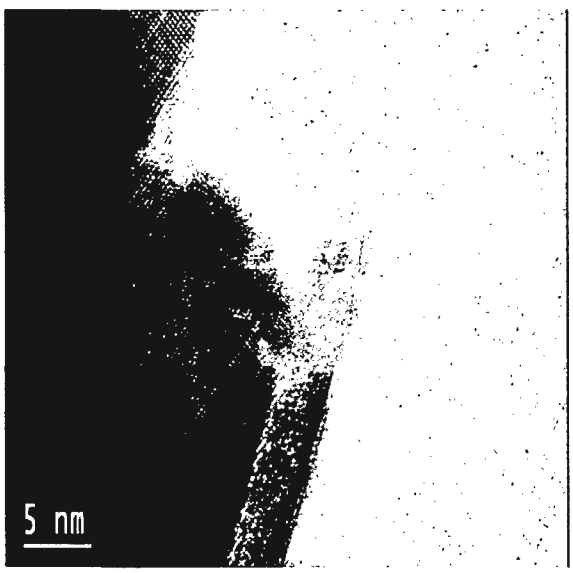

Figure 4.16: HRTEM image of the membrane. It is crystalline at the investigated region.

More problematic is the fact that strong twinning occurs in this layer, because of the roughness of the Al(Mo) alloy. In section 5.2.4 more detailed information is given about these defects.
When looking detailed at the Mo/Al(Mo) interface, one sees a lot of small crystals penetrating from the Mo layer into the Al(Mo) alloy. Using EFTEM these crystals can be identified as pure Mo, as shown in figure 4.17.

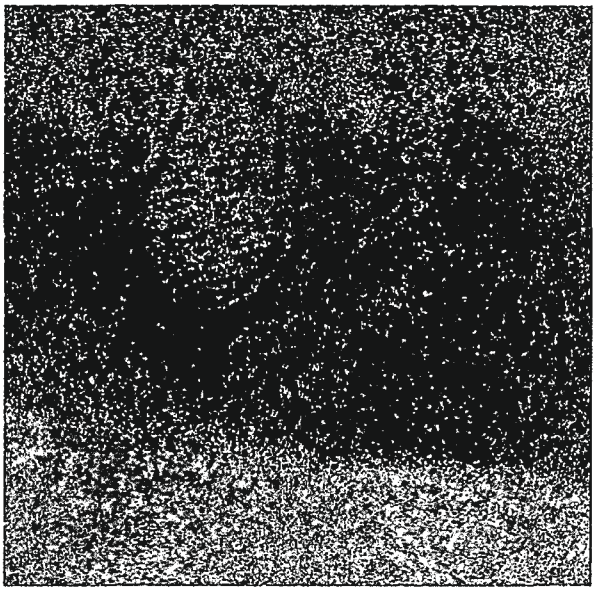

Figure 4.17: elemental map of the Mo/Al(Mo) interface (blue:Mo, red:Al, green:Si).

Chapter 5

The Structure of the Solar Cells

5.1 The Seedinglayer

5.1.1 Influence of the Al Layer on Si Grain Size

The Al layer has two different possibilities to influence the seeding layer. One is the Al grain size, the other one is the defect concentration. With the Al grain size the Si-diffusion within the Al layer can be controlled (the larger the Al grains, the worse the ratio GBs/grains, which means that diffusion is retarded). With the latter possibility the diffusion at the hetero-interface, at GBs and inside the grains is influenced. The influence of course is largest at the hetero-interface and smallest inside the grains, because defect states like vacancies tend to accumulate at GBs and surfaces. Therefore a higher defect density reduces the activation energy for hetero-interface diffusion of Si. Comparing the calculated activation energies in tables 4.2 and 4.3 one sees that specimen A 04-103-1 has a higher defect concentration. And indeed the base pressure during the Al deposition was $3.7 \cdot 10^{-7}$ mbar for the first specimen and $7 \cdot 10^{-7}$ mbar for the latter one.

5.1.2 Influence of Membrane on Si Grain Size

In the thesis of O. Nast [74] the activation energy for the ALILE process is given with 1.3 ± 0.1 eV (using a further developpement of Eq. 4.10). When we do the same calculation as described there for specimen A 04-103-1 we find 1.44 ± 0.15 eV. Has the activation energy increased? When taking a closer look it gets clear that this value is not the activation energy for the ALILE process and the conclusion that mixed diffusion for pc-Al is the dominant process is therefore not justified. The activation energy for mixed diffusion in pc-Al is strongly dependent on the ratio of GBs to grains. The value of 1.3 eV is valid for large sized grains having a diameter of a view micrometers [96]. In the present case the diameter of the Al grains does not exceed 200 nm. The activation energy should be much lower and in the range of 0.8 eV [95] because there are more grain boundaries relative to the grains as in larger grained layers. But it is true that mixed diffusion is a dominant process in ALILE. Only the value of 1.3 eV describes not this process. It describes the porosity of the membrane. The higher the value,

the more dens is the membrane.
From figure 4.8 we learned that the increase of the curve strongly depends on the membrane. Under the assumption that the flux of atoms through the membrane is dominated by its porosity, the ratio of ξ-values of table 4.2 and 4.3 gives the ratio of porosities of the two membranes. But we learn more from this. In table 5.1 we see, that for 460° this ratio differs from the other temperatures.

Table 5.1: Comparison of ξ from samples A 02-093-3 and A 04-103-1 at several temperatures with ξ_1 from table 4.2 and ξ_2 from table 4.3.

$T(°C)$	ξ_1/ξ_2
460	3.533
480	2.333
500	2.333

This difference can be lead back to a transformation in the membrane at higher temperatures.
But there is another factor which influences the ALILE process very strong, or, better, it dominates the layer exchange: the thickness of the membrane. If it is too thin, too many holes are in the membrane and the exchange process starts during a-Si deposition. This was observed via plasmon filtered imaging. Here delocalization in the inelastic signal plays a minor role, because no extreme spatial resolution is required. Figure 5.1 shows the EFTEM image.

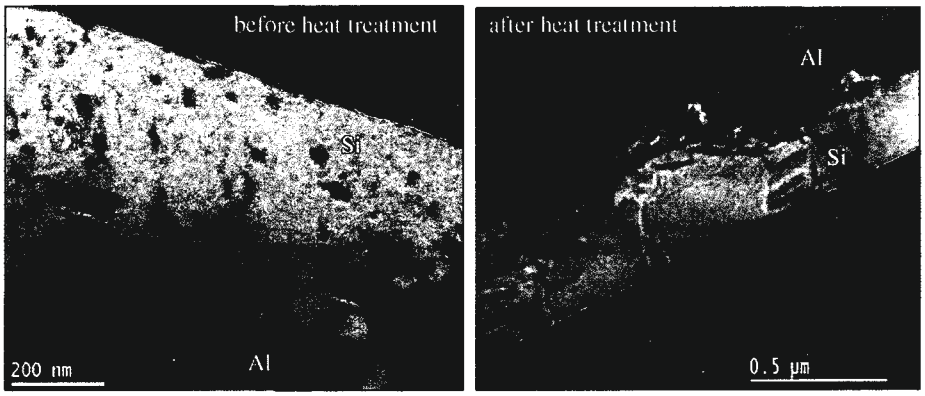

Figure 5.1: Plasmon filtered image of a "pc-Al/a-Si" layer system with 8 minutes oxidation of the Al layer before a-Si deposition. Due to the bad membrane, layer exchange and crystallisation start during the a-Si deposition.

The size of the Si crystals after layer exchange is very small. Table 5.2 gives an overview of the correlation between oxidation time and final Si-grain size.

Figure 5.2: Plasmon filtered image of a "pc-Al/a-Si" layer system with 120 minutes oxidation of the Al layer before a-Si deposition. Due to the good membrane no layer exchgange can be observed before heat treatment. The crystal size of the final seeding layer is much larger as in figure 5.1.

Table 5.2: Grain sizes for several oxidation times before and after heat treatment.

oxidation time	Si gr. size (after)	Al gr. size (before)	Si (before)
0 min	500 nm	500 nm	pc
2 min	–	500 nm	pc
8 min	500 nm	300 nm	pc + amorphous
10 min	1000 nm	–	–
60 min	3000 nm	2500 nm	amorphous
120 min	10000nm	1500 nm	amorphous

Measuring the thickness of the membrane

When measuring the thickness of the membrane there are three possibilities. One is acquiring a plasmon filtered image. Here delocalization plays an important role. The measured thickness without consideration of delocalization would be 4.5 nm (distance between the two dashed lines inlay of figure 5.3.

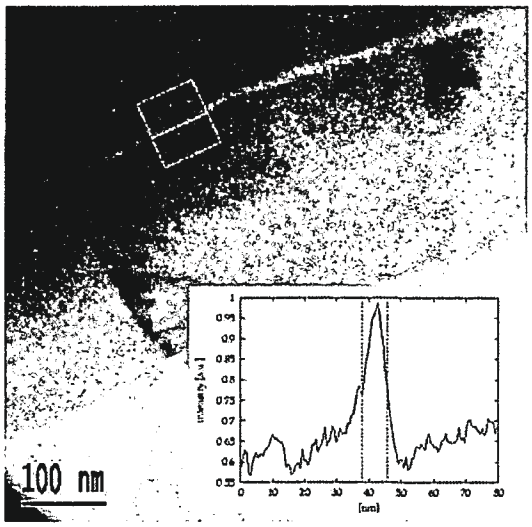

Figure 5.3: EFTEM image acquired at 40 ± 2.5 eV. The inset shows the line profile of the marked region. The measured membrane thickness is 4.5 nm.

Another possibility is to acquire an elemental map as shown in the inset of figure 4.11. The last possibility is to acquire an HRTEM image in Fresnel contrast conditions. In Scherzer focus one never has the chance to distinguish between the amorphous membrane and the amorphous Si, therefore Fresnel conditions are neccessary. This is shown in figure 5.4. Again the inset shows the gray scale profile. The distance betwen the two maxima is only 1.7 nm which is the true value for the membrane thickness.

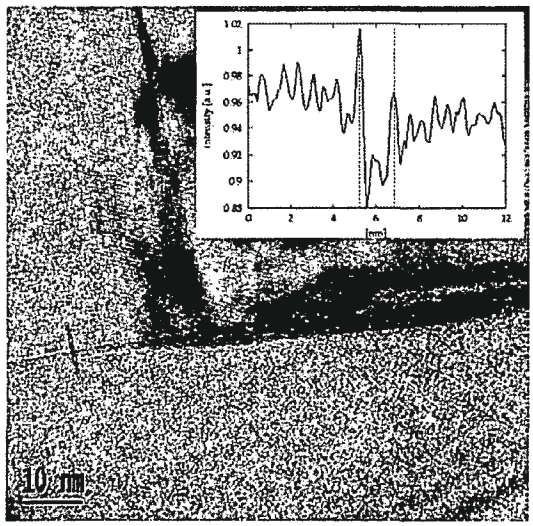

Figure 5.4: HRTEM image in Fresnel contrast conditins. The inset shows the brightness profile across the interface. The dashed lines limit the membrane. The thickness measured with this method is 1.7 nm.

5.1.3 Crystal Growth

From the crystal maker's point of view only grains with (100) planes parallel to the glass substrate are of interest, because low temperature epitaxy can only be applied successfully on such grains. Therefore the layer exchange parameters should be chosen in such a way that preferential (100) oriented grains can grow. From the prior experience we now can draw a flow-chart including all requirements for large sized and (100) oriented Si crystals. This is done in figure 5.5.
Of main importance for large sized crystals are long nucleation lengths l_n which are controlled by the flux through the membrane and the defect concentration in the Al/membrane interface. The flux should be small, the defect concentration should be high.
For (100) oriented grains a low flux within the Al layer is neccesary. This means that the concentration gradient of Si must not be too large. A small concentration gradient $\frac{dc}{dx}$ can be achieved either by a large diffusion constant (this means high defect concentration) or low temperature. Summing up low temperature and high defect concentration will guarantee highest yield in (100) oriented crystals. Too fast crystallization would lead to a preferential (111) orientation [97].

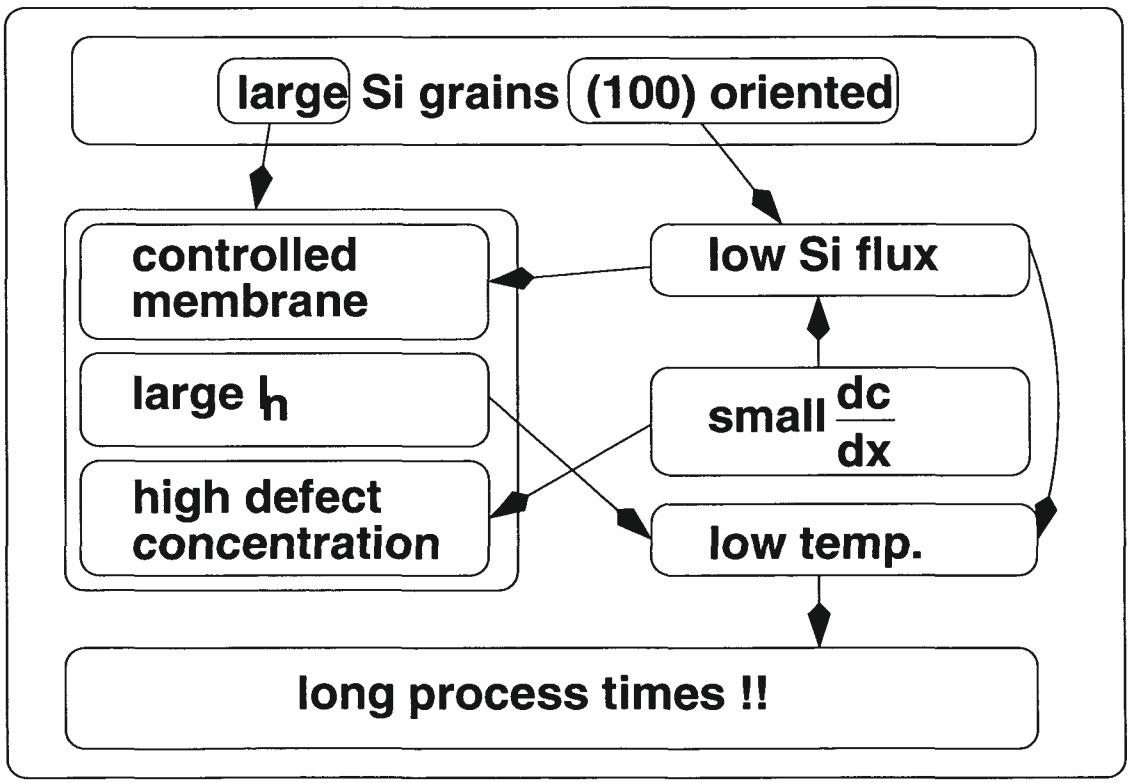

Figure 5.5: Flowchart for (100)-oriented crystal growth in ALILE.

5.2 The Epitaxial Growth on the Seedinglayer

After the seeding layer is formed by means of ALILE, the covering Al layer (which inludes Si islands due to the oversupply of Si before the layer exchange) is removed by chemical etching. The Si islands stay stable during this process but the membrane - if not protected by an Si island - is removed, too. Therefore the next step is a polishing procedure. For this purpose a chemical-mechanical-polishing (CMP) procedure was selected. This has the advantage that the residual surface after CMP treatment is flat, even on the atomic scale. Figure 5.6 shows an interface seed layer/EPI-layer.

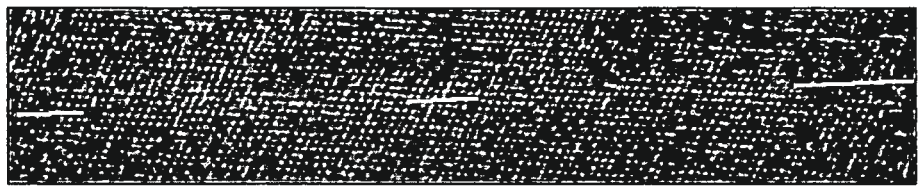

Figure 5.6: HRTEM image of the interface seed layer/EPI-layer. The interface is so perfect, that low temperature epitaxy can be performed without complications. The white lines mark the position of the interface.

The difficulty for epitaxial growth (EPI- growth) at low temperatures is that the mobility of the atoms is not very high due to the low temperature. That's why an atom takes one of the first locations for implementing itself into the layer. This leads to many differently formed defects. At higher temperatures, EPI-growth is not so problematic. Even grains with other orientations than the [100] orientation are reproduced very well [98].
But for first studies of low temperature epitaxy Si wafers with a very flat (100) and (111) oriented surface were used.

5.2.1 Pyramides in EPI-layers on Si(100) wafer substrates

In plane view projection all polycrystalline defects have a squared shape and consist of needle-like crystals. The diffraction pattern in figure 5.12 shows that the orientation of the matrix is (100). The borders of the defects in the shadow image are perpendicular to the (220) diffraction spot, therefore the squared shape of the defect are in (110) orientation with respect to the matrix. The needles long axes are perpendicular to the thin film-substrate interface (figure 5.8c). At the edges of the defect, lines with an angle of 35.4° to the surface normal can be identified which is the (111) direction. These lines are due to microtwins that are shown in detail in figure 5.8d. A small impurity like a lattice defect of the substrate or an atom of a foreign species can be the reason.
In figure 5.8 electron diffraction images of the matrix from the left (a) and right (b) hand side of a defect (c) are shown. The typical features for microtwinning like the additional diffraction spots at each third of the distance and the streaks connecting the diffraction spots are clearly visible. A high-resolution acquisition (d) shows the microtwins on the right hand side of the defect (marked with B in image c). The microtwins have a thickness of 3-5 monolayers and are oriented in the (111) planes of the matrix.

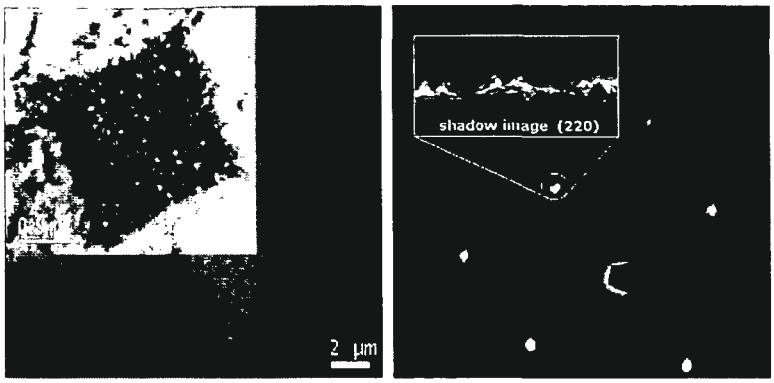

Figure 5.7: TEM micrograph of the defects (left). The polycrystallinity can be seen easily. And a diffraction pattern and shadow image of the plan view sample (right).

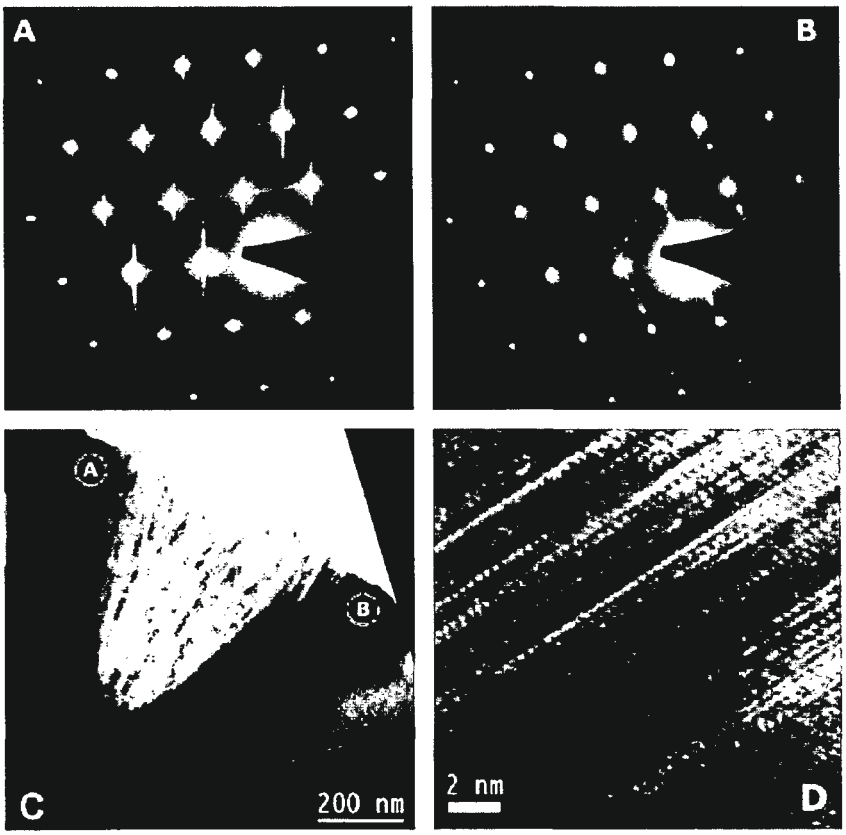

Figure 5.8: (a) diffraction pattern from the left hand side of the defect shown in (c), (b) diffraction pattern from the right hand side of the defect shown in (c) and (d) HRTEM image of the nanotwins.

5.2.2 Pyramides in EPI-layers on Si(111) wafer substrates

From results presented in chapter 5.12 it is clear, that low temperature epitaxy works well on Si(100) wafer substrates. Only a few defects occur. Before we try to find the reason for defect formation (see section 5.2.3) we take a look at epitaxy on a differently oriented Si wafer substrate, which is a Si(111) wafer substrate. In figure 5.9 a TEM cross section specimen is shown. In the diffraction pattern in figure 5.9 the typical diffraction spots of nanotwins can be identified. A light polycrystalline ring structure can also be observed coming from the upper part of the selected area (white circle in the bright field image). We can therefore conclude that polycrystalline layer growth in low temperature epitaxy starts with nanotwinning on Si(100) and Si(111) substrates.

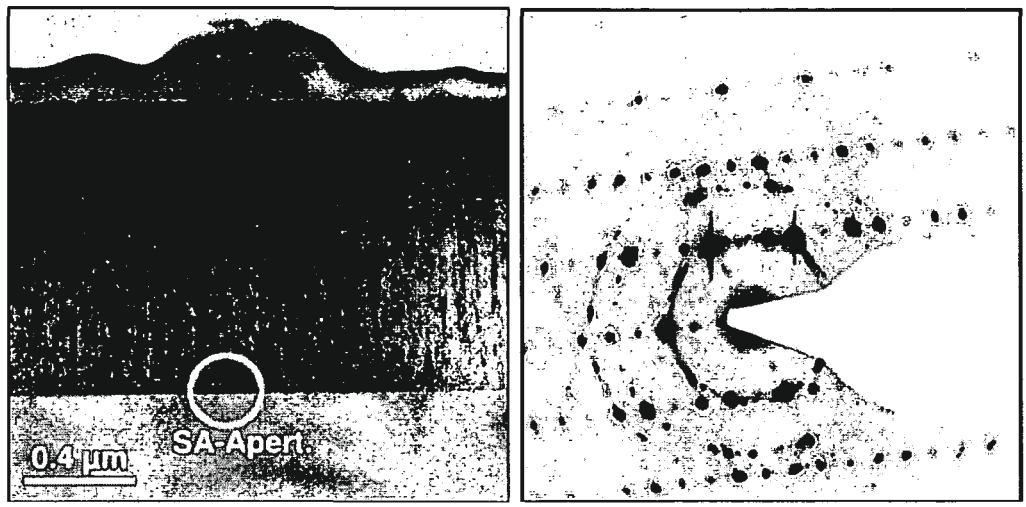

Figure 5.9: TEM micrograph of the "epitaxially" grown layer (left). The polycrystallinity can be seen easily. The position of the selected area aperture is marked with a white circle. The diffraction pattern (right) shows the typical features of nanotwinning.

For quantification of these twins an HRTEM image was recorded at the substrate/layer interface. Please notice that the image is upside down, which means that in figure 5.10 the wafer is on top and the layer is at the bottom side of the image. The crystallographic orientations and the interface are annotated. It now becomes clear that the wafer substrate is not parallel to the (111) lattice planes. However, epitaxy seems to work for the first few tens of monolayers due to the fact that nanotwins are coming up to reduce stress. One clearly sees that the turn down of the (110) lattice planes is along the (111) planes.

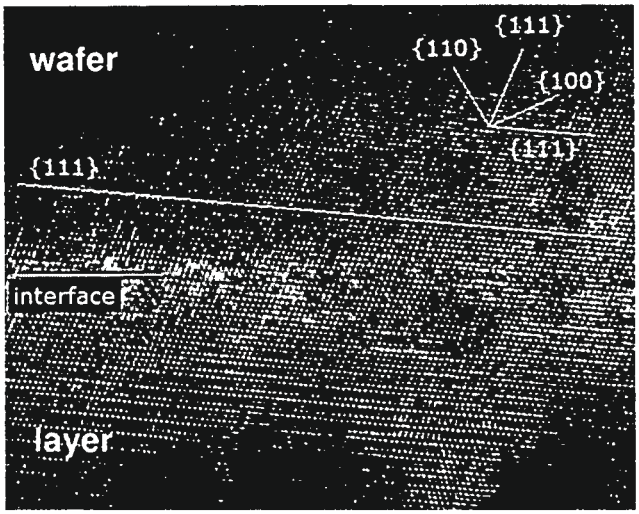

Figure 5.10: HRTEM image of the wafer substrate (top)/layer (bottom) interface.

This image proves that epitaxy on Si(111) works nearly not. It is therefore justified to conclude, that epitaxy is not possible, as observed by Rau et al. [99].

5.2.3 Polycrystalline Layers and their Cause

In the previous two sections it was found that low temperature epitaxy is very difficult to achieve because it is so sensitive to the crystal orientation of the substrate. Therefore it is neccesary to go into detail of epitaxial growth.
The driving force for epitaxial growth is the dependence of the interfacial energy on the crystalline orientation of a film with respect to its single crystal substrate. As this dependence is a universal phenomenon, epitaxial growth, in principle, is a also universal phenomenon. The only essential conditions being that at the temperature needed for sufficient mobility of the growing material no interdiffusion or even melting takes place. In low temperature epitaxy these conditions are met automatically. This means that defect growth in epitaxy is only influenced be defect formation on the substrate surface or incorporation of foreign material during Si deposition. The main problem in Si(111) is that the dangling bonds are all normal to the surface, whereas in Si(100) orientation the dangling bonds are tilted pairwise. This seems to be better from the energetic point of view. Furthermore, if a lattice defect (such as a vacancy or a foreign atom) appears on the Si(111) surface, a three-fold dislocation grows. It is therefore nearly impossible to achieve good epitaxy. That's why industry prefers Si(100) oriented surfaces but with many teraces. These teraces should not be too high, otherwise there can be an overgrowth of terraces. In figure 5.10 one sees that the surface is not parallel to the (111) direction. The teraces are very high due to the large tilt angle.
Another fundamental problem is the cleanliness of the surface. If dirt lies on the surface, epitaxy breaks down immediately. If the terraces are high there is much place for foreign atoms to hide and to escape the cleaning process. For low temperature epitaxy it is therefore necessary to provide an

extremely clean surface. Maybe an additional cleaning step must be added before epitaxial growth. Foreign atoms therefore are the nucleation center of defects. The lattice constant of the surrounding matrix is changed a little bit, meaning that the bond lengths are enlarged. This can be measured in an electron microscope equipped with a pre-specimen energy filter. Measurements were therefore performed in a pc-Si region, in a highly twinned region close to a pyramid like defect (see Fig. 5.8), and in a perfect monocrystalline region (wafer substrate). This experiment was repeated with another specimen, finding the same changes of the energy shift in the ionisation edge. Figure 5.11 shows three typical spectra of the wafer (left), the pc-Si (middle) and the nano twins (right) shifted by 0.2 eV and 0.3 eV, respectively, with respect to the Si-L edge onset of the spectrum recorded in the wafer.

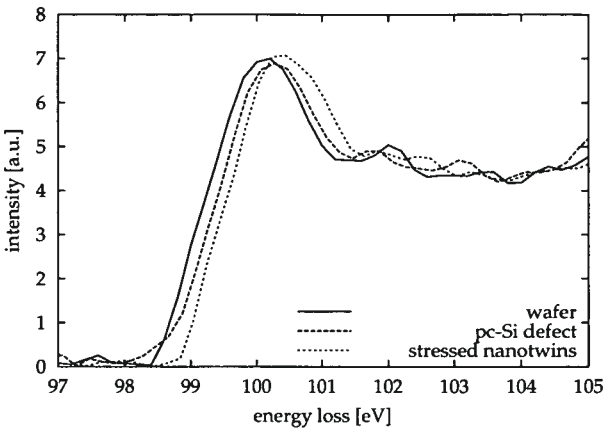

Figure 5.11: Si L_3 edges of the wafer, the pc-Si defect region and the stressed nano twin region. There is a core level shift due to increasing bond lengths.

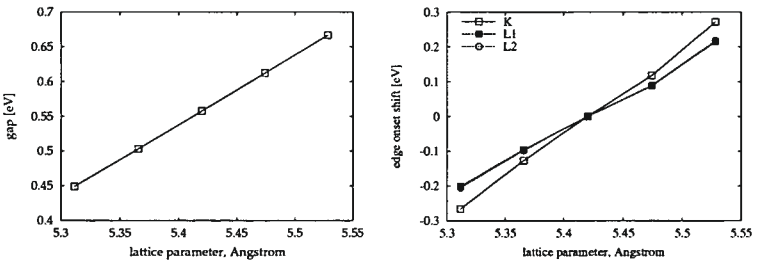

Figure 5.12: Simulations of the relative change in the bandgap (left) and the core edges of Si (right) in dependenc of a relative change in the bond length calculated with the *Wien2k*-code.

From the presented measurements it is clear, that in the selected areas an increase of bond length is the reason for the core level shift. All other influences like charge transfer due to chemical bonding or other environmental contributions were checked and can be excluded.

5.2.4 Defect Analysis of the Seedinglayer

As shown in the previous section, the quality of the seeding layer for epitaxial thickening is of main importance. Defect analysis is therefore neccessary. Up to now we know that Si grains with (100) surface planes are good for low temperature epitaxy. But the grains of the seedinglayer have many stacking faults, like nanotwins. In the secondary electron microscope (SEM) image in figure 5.13 some grains show traces lying perpendicular to each other. It are these grains that have a (100) surface orientation!

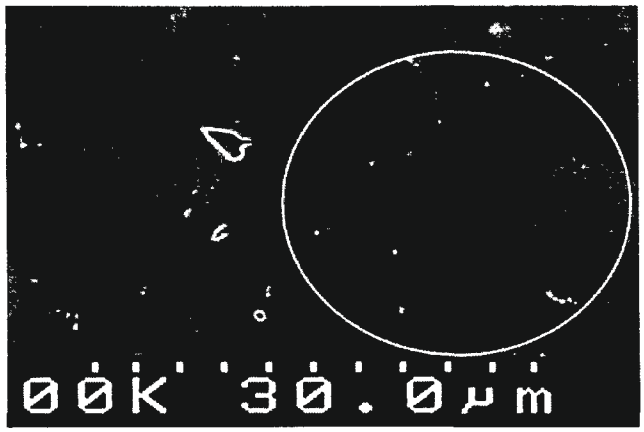

Figure 5.13: SEM image of a seed layer. The circle marks grains with traces perpendicular to each other.

Figure 5.14 shows a cross section preparation of a seed layer grain. The shadow image proved that its surface plane is in (100) direction. The corresponding diffraction paterns from the left hand-side, a middle position and the right hand-side of the grain are shown in figure 5.15. All diffraction pattern show twinning. The left one shows only little of it, the one in the middle indicates that this region is heavily twinned whereas the right one indicates twinning only in one direction.

Figure 5.14: TEM cross section image of the seed layer. The long dark grain at the bottom side of the cross sectin has a (100) surface plane proved by shadow imaging. (This proof is not shown here.)

Twinning in a diffraction pattern can be identified as small intensity maxima dividing the distance of the main diffraction spots inte three equal parts if looking in a (110) crystal direction. Depending on the (111) mirror plane additional spots in the (111) directions can be found from mirroring a (110) spot of the original lattice.

Figure 5.15: Diffraction pattern of the grain in fig. 5.14 from areas on the left hand-side, the middle and the right hand-side.

Looking at such a grain in TEM having a plane view preparation, a shadow image proves that the lines are along the (110) axes, as shown in figure 5.16.

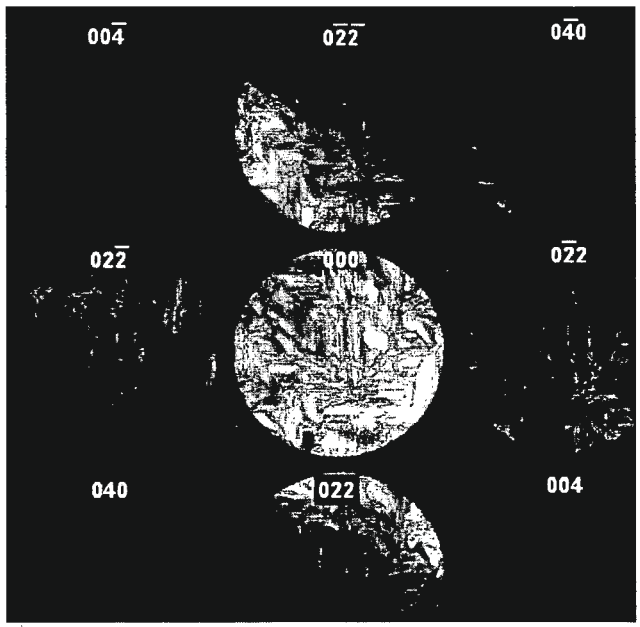

Figure 5.16: Diffraction pattern with shadow images of a plane view prepared specimen. The traces are clearly in (110) directions.

From these investigations we can consider that the traces visible in figure 5.13 can be attributed to heavily twinned regions. Figure 5.17 makes it easier understandable.

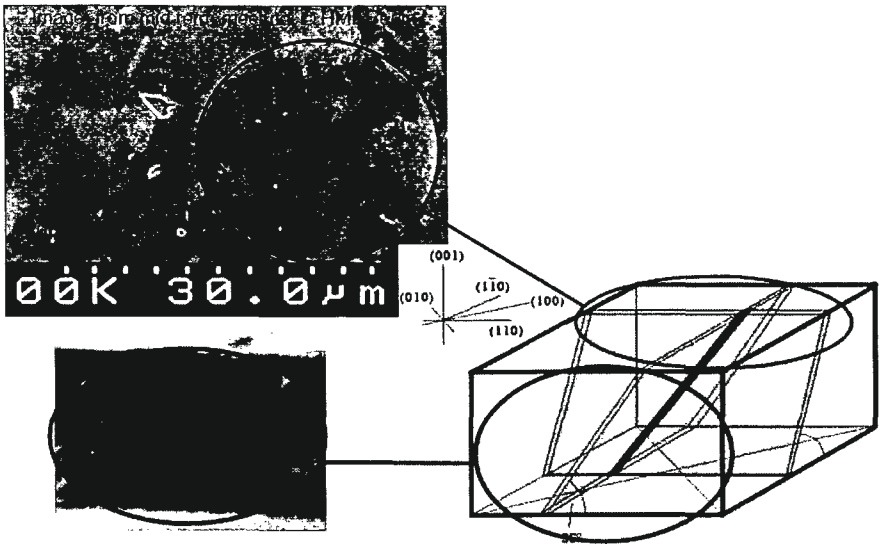

Figure 5.17: Model for the traces visible in the SEM micrograph.

5.2.5 Epitaxy on the Seedinglayer as Substrate

Since we have now performed two case studies, first epitaxial layers were grown onto seeding layer substrates. In this case epitaxy will partly fail and partly succeed. Figure 5.18 shows a typical overview of such a layer system. The diffraction pattern acquired at the marked positions (white circles) are all equal and shown in the inset. The thickness of polycrystalline regions is 421 nm whereas epitaxially grown regions only have a thickness of 400 nm. This means that pc-Si has a need of 5% more volume than monocrystalline Si.

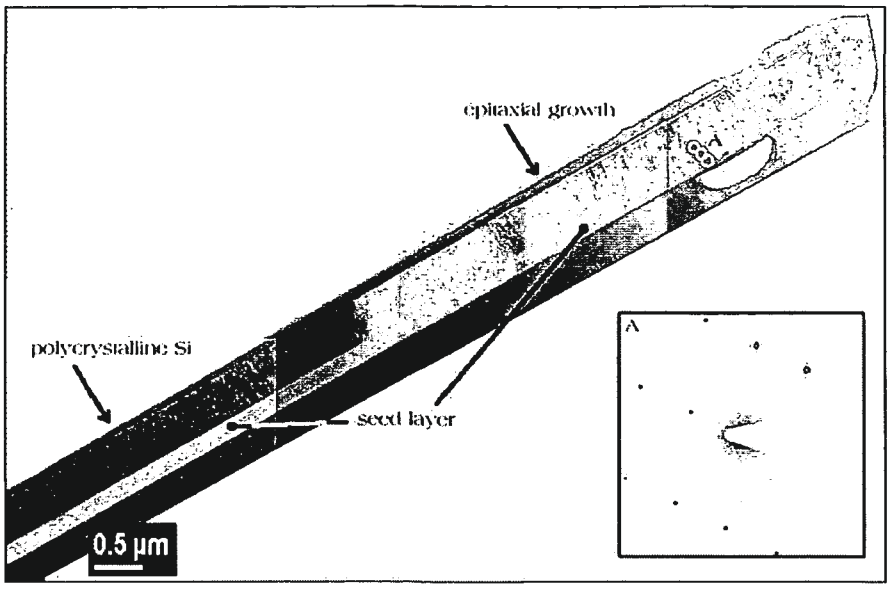

Figure 5.18: Epitaxially thickened layer (ASE005). Partly there is epitaxial growth observable and partly pc-Si was produced.

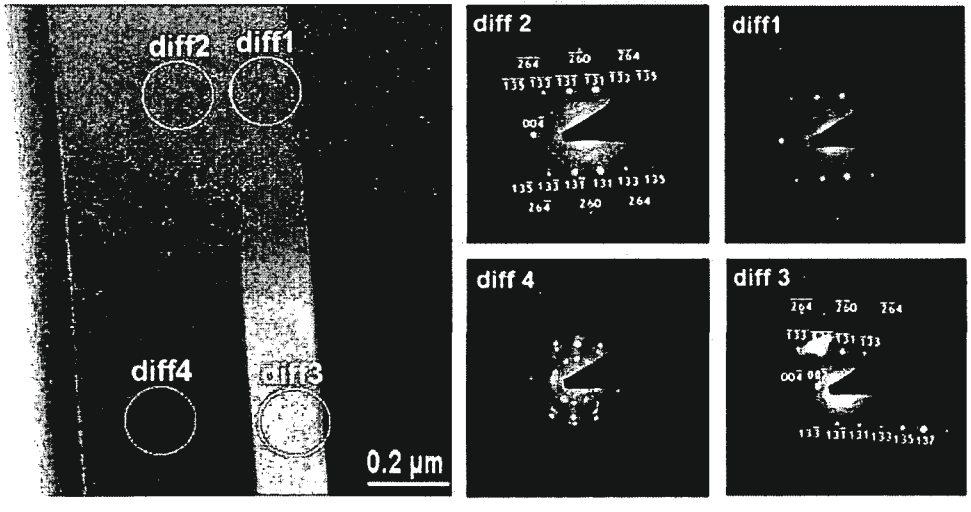

Figure 5.19: Magnification of the region where pc-Si and epitaxial growth meet. The inlays show diffration patterns acquired at the positions marked with white circles.

When taking a closer look, as done in fig. 5.19, one sees the reason of breakdown of epitaxy. The diffraction patterns *diff1* and *diff2* are absolutely equal. The layer was thickened perfectly epitaxial. Comparing *diff1* and *diff3* a slight tilt of 7.8° can be observed. It seems that this tilt is enough to from a too high nanotwin density leading to an early breakdown of epitaxy.
On the other hand we know from OIM (Orientation Imaging Microscopy), which is based on an elec-

tron backscattering diffraction (EBSD) technique, that a tilt of a few degrees (up to 10°) towards the (111) direction does not disturb epitaxial growth (figure 5.20). Before OIM investigations of the seed layer were performed, the surface was flattened using a chemical-mechanical-polishing routine (CMP). The epitaxial layer has a thickness of approximately 400 nm and was deposited at 585°C.

In Fig. 5.20 two OIM images and their corresponding reduced pole figures are shown. The upper image was recorded from the seed layer before epitaxial thickening and the lower one was acquired after epitaxy. The corresponding pole figures (PF) (so called reduced PFs) have all data points stemming from (100) orientation in the left corner, in the right bottom corner data points are stemming from (110) oriented areas and areas with (111) orientation give data points in the top right corner. The distance between the (100) and (110) corner is a linear scale of 45° and the distance between (100) and (111) is a linear scale of approx. 54°, which is the tilt angle between (100) — (110) and (100) — (111), respectively.

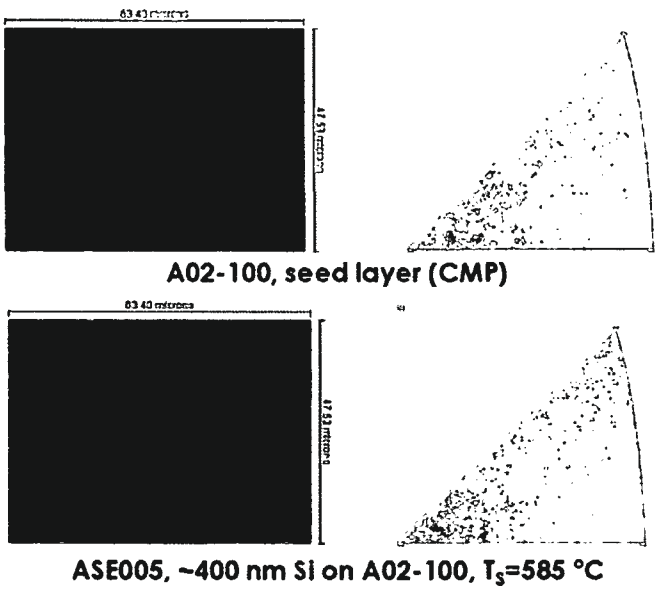

Figure 5.20: OIM image of an area before and after epitaxial thickening. From the comparison of the two inverse pole figures it can be shown which orientations are reproduced while epitaxy.

Low temperature epitaxy is not trivial on seed layers produced by ALILE. First results as shown in figure 5.20 are quite promising for further developement of this technique.

Chapter 6

Conclusion

English version

This mainly experimental work can be devided into two parts. Part one deals with the limits of electron energy loss spectrometry (EELS) as to spatial and energy resolution. Energy resolution can be improved by an order of magnitude when using a monochromated TEM. Improvement is nearly an order of magnitude. With such an electron source, fine structures in the ionisation edges can be observed, that would otherwise be hidden from observation and only be accessible for ELNES simulations.
Within this thesis the ELNES separation method was developped employing ELNES of two phases of one and the same material. This method was tested with several materials, such as copper and chromium, and under different conditions (with and without monochromator, in plane view and at interfaces). With this method, chemical shifts can be measured directly, as shown for chromium and chromium oxide. Another application of this method was the investigation of oxidation states of silicon at the Si-membrane interface in the specimens of the METEOR project (cont. nbr. ENK-5-CT-2001-00543) of te European Commission.
Furthermore, investigations of the delocalization phenomenon were performed for parallel and focussed illumination (TEM and STEM mode of the microscope). It is now easier to interpret plasmon filtered images since delocalization in plasmon losses is in the range of 10 nanometers. A surprising result was found when measuring the monopole and dipole transitions of Si atoms in HRSTEM. The conditions for such measurements are rather bad, because of beam spreading and delocalization. But nervertheless a non-negligible effect can be observed when measuring on and between the atoms.
The second part of the present thesis deals with the ALILE layer exchange and the further epitaxial thickening of the ALILE produced seed layers. Investigations of band structure at the Si-Al interface were performed finding the metal induced gap states (MIGS) the first time directly by means of EELS. A simple model describing diffusion of Si along the Al-membrane interface during the layer exchange was developed. Using this model, the activation energy for this process can be determined in dependence of defect concentration in the pc Al-layer which itself depends on the base pressure during Al deposition. Furthermore, it was found with this model that the membrane is transformed during heat treatment which was confirmed later on.

TEM investigations of epitaxially grown layers are presented. Different test specimens were produced for studies of epitaxial growth on several substrates with different orientations. All tests show the same reason for breakdown of epitaxy: due to stress nanotwinning occurs. If the density of nanotwins is too high, epitaxy breaks down and polycrystalline growth starts. The probability for twinning depends on the substrate orientation, which is the orientation of each grain in the seed layer. Therefore effort must be taken for influencing the crystal growth during ALILE in such a way, that the major orientation of grains is the (100) orientation. The can be done by increasing the process time as shown in figure 5.5.

Deutsche Fassung

Diese hauptsächlich experimentelle Arbeit ist in zwei Teile zu unterteilen. Im ersten Teil werden die Grenzen der experimentellen Elemtronenenergieverlustspektrometrie (EELS) erprobt in Bezug auf Orts- und Energieauflösung. Die Energieauflösung kann unter Zuhilfenahme eines mit einem Monochromator bestückten TEM um beinahe eine Größenordnung verbessert werden. Dadurch ist es möglich, Strukturen in der ELNES zu beobachten, die einem sonst experimentell verborgen blieben und nur rechnerisch zugänglich wären.
Die ELNES-Seperationsmethode, die im Rahmen dieser Dissertation entwickelt wurde, um Messsignale von inhomogenen Proben zu untersuchen, wurde an Hand von einigen Materialien überprüft und selbst bei Benützung des Monochromatormikroskops der TU Delft kann die ELNES der unterschiedlichen Phasen sehr genau getrennt werden. Chemische Ionisationskantenverschiebungen können damit präzise gemessen werde, wie es hier für Chrom gezeigt ist. Eine Anwendung der ELNES Separation war die Untersuchung der Oxidationsstufe von Silizium an den Aluminiumoxidmembranen in den Solarzellenproben aus dem METEOR Projekt (Contr.Nr. ENK-5-CT-2001-00543) der Europäischen Kommission.
Untersuchungen der Delokalisierung von Energieverlusten wurden für parallele Beleuchtung und STEM angestellt (TEM und STEM Modus des Mikroskops). Damit ist es möglich, Plasmonengefilterte Bilder genauer zu interpretieren. Erstaunlich ist, dass im STEM Modus die ELNES von Silizium so genau gemessen werden kann, dass die unterschiedlich intensiven Anregungen der Monopol- und Dipolübergänge auf und zwischen den einzelnen Atomen gemessen werden kann.
Der zweite Teil dieser Dissertation beschäftigt sich mit dem ALILE-Schichtaustauschprozess und der weiteren epitaktischen Verdickung der Schichten. Es wurden Untersuchungen der Bandstruktur von Si an einer Si-Al Grenzschicht durchgeführt, die das Abschirmungsmodell von Hiraki bestätigen sollten. Dabei konnten erstmals die metallinduzierten Bandlückenzustände (MIGS - metal induced gap states) direkt mittels EELS nachgewiesen werden.
Weiters wurde ein einfaches Modell zur Siliziumdiffussion entlang der Al-Membran Grenzschicht entwickelt. Damit kann die Aktivierungsenergie in Abhängigkeit von der Defektkonzentration ermittelt werden. Weiters wurde daraus abgeleitet, dass sich die Membran während des Schichtaustauschen kristallographisch transformieren muss, was später auch experimentell mittels Nano-Beugung nachgewiesen wurde.
Zum Schluß finden sich noch die TEM-Untersuchungen der epitaktisch verdichten Schichten. Verschiedene Tests auf unterschiedlichen Substraten zeigen alle die selbe Ursache für den Zusammenbruch der Epitaxie: auf Grund von Spannungen entstehen Nanoverzwilligungen im Kristallgitter. Wenn die Dichte der Verzwilligungen zu groß wird, bricht die Epitaxie zusammen. Die Wahrscheinlichkeit der Verzwilligung ist stark von der Substratorientierung abhängig, sprich von der Orientierung der jeweiligen Si-Körner der Saatschicht. Es müssen daher Bestrebungen laufen, die Orientierung der Saatschichtkörner zu kontrollieren und in (100) Orientierung auszurichten. Dafür muss aber die Prozesszeit des Schichtaustausches verlangsamt werden, wie in Abbildung 5.5 dargestellt.

Bibliography

[1] M Stöger, J Schneider, Zandbergen H W, S Gall, and P Schattschneider. Investigation of bonding at an aluminium (iii) oxide membrane using elnes separation. *IoP Conf. Ser.: Microsc. Semicond. Mat.*, 180, 2003.

[2] M Stöger, C Hébert, E C Karl-Rückert, P Schattschneider, B Rau, S Gall, and H W Zandbergen. Investigation of core level states in epitaxial grown si layers by eels. *IoP Conf. Ser.: Microsc. Semicond. Mat.*, 180, 2003.

[3] M Stöger, P Schattschneider, J Schneider, and S Gall. The elnes separation applied to oxidation states of interfaces. *6th Multinat. Congr. on Microsc., 1-5 June 2003, Pula, Croatia*, 2003.

[4] M Stöger, C Hébert, P Schattschneider, H W Zandbergen, B Rau, and S Gall. Sub-ev core level shifts in si grain boundaries and nanotwins. *6th Multinat. Congr. on Microsc., 1-5 June 2003, Pula, Croatia*, 2003.

[5] M Stöger, P Schattschneider, C Hëbert, and H W Zandbergen. Unexplained thickness dependence in the si loss function at 0.14 ev energy resolution. *6th Multinat. Congr. on Microsc., 1-5 June 2003, Pula, Croatia*, 2003.

[6] R.F. Egerton. Electron energy-loss spectroscopy in the electron microscope. *Plenum Press NY, ISBN 0306452235*, 2nd Ed., 1996.

[7] S Clair. Eels feinstrukturen der cu-l2,3 ionisationskante in cuni legierungen. *Diplomathesis, Vienna University of Technology*, 1999.

[8] M Stöger. Tem and eels microanalysis of pc- si thin films for solar cells. *Diploma Thesis, Vienna Univ. of Technology*, 1999.

[9] B Schaffer, W Grogger, and F Hofer. Width determination of sio2-films in si-based devices using low-loss eftem: image contrast as a function of sample thickness. *Micron*, 34 (1):1–7, 2003.

[10] P M Vojles, J L Grazul, and D A Muller. Imaging individual atoms inside crystals with adf-stem. *Ultramicroscopy*, 96:251–273, 2003.

[11] Bergmann-Schäfer. *Festkörper*, 8.ed.:551–556, de Gruyter, Berlin 1992.

[12] O A Neumueller. *Rmpps Chemie-Lexikon*, 6. ed., Frankh'sche Verlagshandlung, Stuttgart 1975.

[13] J H Werner, R Bergmann, and R Brendel. The challenge of crystalline thin film solar cells. *Advances in Solid State Physics*, 34:115, 1995.

[14] R Brendel, R Bergmann, P Lolgen, M Wolf, and J H Werner. Ultrathin crystalline silicon solar cells on glass substrates. *Appl.Phys.Lett.*, 70:390, 1997.

[15] K Yamamoto, M Yoshimi, Y Tawada, Y Okamoto, A Nakajima, and S Igari. Thin-film poly-si solar cells on glass substrate fabricated at low temperature. *Appl.Phys. A*, 69:179, 1999.

[16] R. Bergmann. Crystalline si thin-film solar cells: a review. *Appl.Phys. A*, 69:187, 1999.

[17] Y Wang, O van der Biest, C Ornaghi, and G Roebben. Metal induced crystallization. *METEOR Meeting Leuven, Belgium*, 2003.

[18] C. Scheu, G. Dehm, H. Müllejans, R. Brydson, and M. Rühle. Electron energy-loss near-edge structure of metal-alumina interfaces. *Microsc. Microanal. Microstruct.*, 6:19–31, Feb. 1995.

[19] C Scheu. Reliability of interfacial electron energy-loss near-edge structures determined by the spatial difference technique. *Dreiländertagung f. Elektronenmikroskopie, Innsbruck*, Sept. 2001.

[20] J. Bruley, V. J. Keast, and D. B. Williams. Measurement of the localized electronic structure associated with bismuth segregation to copper grain boundaries. *J. Phys. D: Appl. Physics*, 29:1730–1739, 1996.

[21] H. Müllejans and J. Bruley. Improvements in detection sensitivity by spatial-difference electron energy-loss spectroscopy at interfaces in ceramics. *Ultramicroscopy*, 53:54–70, 1994.

[22] H. Müllejans and J. Bruley. Electron energy-loss near-edge structure of internal interfaces by spatial difference spectroscopy. *Journal of Micoscopy*, 180:12–21, 1995.

[23] C. Scheu, G. Dehm, and M. Rühle. Electron energy-loss spectroscopy studies of cu-$\alpha - al_2o_3$ interfaces grown by molecular beam epitaxy. *Philosophical Magazine A*, 78/2:439–465, 1998.

[24] P Schattschneider and G Sölkner. A comparison of techniques for the removal of plural scattering in energy loss spectroscopy. *Journ. Microsc.*, 134:73–87, 1984.

[25] R.F. Egerton. *Electron Energy Loss Spectroscopy in the Electron Microscope.* Plenum Press, New York, London, 1986.

[26] DS Su, P Jonas, and P Schattschneider. The multiple-scattering problem in electron compton scattering on solids. *Phil. Mag.*, B66:405–418, 1992.

[27] M. Stöger, P. Schattschneider, C. Hébert, and B. Jouffrey. Separation of pure elemental and oxygen influenced signal in elnes. *Ultramicroscopy*, submitted.

[28] J. Bruley. Spatially resolved electron energy-loss near edge structure analysis of a near $\sum = 11$ tilt boundary in sapphire. *Microsc. Microanal. Microstruct.*, 4:23–39, 1993.

[29] P. Schattschneider, M. Stöger, C. Hébert, and B. Jouffrey. The separation of surface an bulk contributions in elnes and exelfs spectra. *Ultramicroscopy*, submitted.

[30] M. Stöger. Elnes of surface oxidized thin films. *PICS meeting, Vienna*, June 2001.

[31] J. Luitz, M. Maier, C. Hébert, P. Schattschneider, P. Blaha, K. Schwarz, and B. Jouffrey. Partial core hole screening in the cu l_3 edge. *European Physical Journal B*, accepted.

[32] P. Blaha, K.H. Schwarz, and J. Luitz. Wien97, a full potential linearized augmented plane wave package for calculating crystal properties. *WIEN97 User's Guide, VUT*, 1997.

[33] M Stöger-Pollach, P Schattschneider, J Schneider, S Gall, and H W Zandbergen. Investigation of bonding at an al2o3 membrane in silicon using elnes separation. *Microscopy of semiconductiong materials*, 2003.

[34] I Alexandrou, AJ Papworth, GAJ Amaratunga, CJ Liely, and LM Brown. Calculation of the electronic structure near the bandgap using eels. *MSM XIII - Conference*, A8, 2003.

[35] P Schattschneider. Fundamentals of inelastic scattering. *Springer-Verlag*, ISBN 3-211-81937-1, 1986.

[36] P E Batson. Silicon l2,3 near-edge fine structure in confined volumes. *Ultramicroscopy*, 50:1–12, 1993.

[37] S Lazar, GA Botton, M-Y Wu, FD Tichelaar, and HW Zandbergen. Materials science applications of hreels in the near edge structure analysis and low energy loss spectroscopy. *Ultramicroscopy*, 96:535–546, 2003.

[38] A Gutirres-Soza, U Bangert, and AJ Harvey. Bandgap related energies of threading dislocations and quantum wells in group-iii nitride films as derived from electron nergy loss spectroscopy. *Phys. Rev. B*, 66:035302 1–10, 2002.

[39] B Rafferty, SJ Pennycook, and LM Brown. Zero loss peak deconvolution for bandgap eel spectra. *Journal of Electron Microscopy*, 49(4):517–524, April 2000.

[40] D W Johnson and Spence J C H. Determination of the single scattering probability distribution from plural scattering data. *J.Phys. D*, 7:771–780, 1974.

[41] R F Egerton and P A Crozier. A compact parallel recording detector for eels. *J.Microsc.*, 148:305–312, 1988.

[42] H Touir and P Roca i Cabarrocas. Optical dispersion relations for crystalline and microcrystalline silicon. *Physical Review B*, 65:155330, 2002.

[43] H Kobayashi, Y Yamamashita, T Mori, Y Nakato, T Komeda, and Y Nishioka. Interface states for si-based mos devices with an ultrathin oxide layer: X-ray photoelectron spectroscopic measurements under biases. *Jpn. J. Appl. Phys*, 34:959–964, 1995.

[44] A J Williamson, R Q Hood, R J Needs, and G Rajagopal. Diffusion quamtum monte carlo calculations of the excited states of si. *Phys. Rev. B*, 57 (19):12140, 1998.

[45] M Rohlfing, P Krueger, and J Pollmann. Quasiparticle band-structure calculations for c, si, ge, gaas, and sic using gaussian-orbital basis sets. *Phys. Rev. B*, 48:17791, 1993.

[46] H Ehrenreich, H R Philipp, and J C Phillips. Interband transitions in group 4, 3-5 and 2-6 semiconductors. *Phys. Rev. Lett.*, 8:59–61, 1962.

[47] L Hedin. New method for calculating the one-particle green's function with application to the electron-gas problem. *Phys. Rev.*, 139:A796, 1965.

[48] M Stöger-Pollach, C Hébert, P Schattschneider, S Rubino, and H W Zandbergen. Direct measurements of bandgaps in eels. *J.Phys.: Cond. Mat.*, submitted, 2004.

[49] A Dimoulas. Moleculaar beam epitaxy of high-k dielectrics for advanced cmos. *EUROMAT 2003*, A1, Lausanne, CH, 2003.

[50] D A Muller and J Silcox. Delocalization in inelsatic scattering. *Ultramicroscopy*, 59:195–213, 1995.

[51] N Bohr. *Phil. Mag.*, 25:10, 1913.

[52] C Dwyer and J Etheridge. Scattering of å-scale electron probes in silion. *Ultramicroscopy*, 96:343–360, 2003.

[53] C Dwyers. *private communications.*

[54] B Rafferty and S J Pennycook. Towards atomic column-by-column spectroscopy. *Ultramicroscopy*, 78:1999, 141-151.

[55] V W Maslen and C J Rossouw. Implications of (e,2e) scattering for inelastic electron diffraction in crystals. 1. theoretical. *Philos.Mag.A*, 47:119, 1983.

[56] M Varela, S D Findlay, A R Lupini, H M Christen, A Y Borisevich, N Dellby, O L Krivanek, P D Nellist, M P Oxley, L J Allen, and S J Pennycook. Spectroscopic imaging of single atoms within a bulk solid. *Phys. Rev. Lett.*, 92(9):095502, 2004.

[57] G E Leithäuser. Über den geschwindigkeitsverlust, welche kathodenstrahlen beim durchgang durch dünne metallschichten erleiden und über die ausmessung magnetischer spektren. *Ann. d Phys.*, 15:283, 1904.

[58] A Bleloch, U Falke, and M Falke. High spatial resolution electron energy loss spectroscopy and imaging in an abberation corrected stem. *Microsc. Conf. Proc.*, MC 2003 Dresden:40–41, 2003.

[59] N D Browning, M F Chisholm, and S J Pennycook. Atomic-resolution chemical analysis using a stem. *Nature*, 366:143–146, 1993.

[60] P E Batson. Simultanous stem imaging and eels with atomic-column sensitivity. *Nature*, 366:727–728, 1993.

[61] P D Nellist and S J Pennycook. Incoherent imaging using dynamically scattered coherent electrons. *Ultramicroscopy*, 78:111–124, 1999.

[62] L J Allen, S D Findlay, A R Lupini, M P Oxley, and S J Pennycook. Atomic-resolution electron energy loss spectroscopy imaging in abberation corrected scanning transmission electron microscopes. *Phy. Rev. Lett.*, 91:105503, 2003.

[63] C J Russouw, L J Allen, S D Findlay, and M P Oxley. Channelling effects in atomic resolution stem. *Ultramicroscopy*, 96:299–312, 2003.

[64] A R Lupini and S J Pennycook. Localization in elastic and inelastic scattering. *Ultramicroscopy*, 96:313–322, 2003.

[65] E M James and N D Browning. Practical aspects of atomic resolution imaging and analysis in stem. *Ultramicroscopy*, 78:125–139, 1999.

[66] G R Anstis, D Q Cai, and D J H Cockayne. Limits on the s-state approach to the interpretation of sub-angstrom resolution electron microscope images and microanalysis. *Ultramicroscopy*, 94:309–327, 2003.

[67] T Yamazaki, M Kawasaki, K Watanabe, I Hashimoto, and M Shiojiri. Effect of small crystal tilt on atomic-column high-angle annular dark field stem imaging. *Ultramicroscopy*, 92:181–189, 2002.

[68] P Schattschneider, M Nelhiebel, H Souchay, and B Jouffrey. The physical significance of the mixed dynamic form factor. *Micron*, 31:333–345, 2000.

[69] P Schattschneider and B Jouffrey. Channeling, localization and the density matrix in elastic electron scattering. *Ultramicroscopy*, 96:453–463, 2003.

[70] P Schattschneider, C Hébert, and B Jouffrey. Localization of low energy losses and the mixed dynamic form factor. *Microsc. Microanal.*, 8 Suppl.2:636CD – 637CD, 2002.

[71] *http://www.wien2k.at.*

[72] C Hébert, J Luitz, and P Schattschneider. Improvement of energy loss near edge structure calculation using wien2k. *Micron*, 34:219–225, 2003.

[73] A Hiraki. Initial formation process of metal/silicon interfaces. *Surf. Sci*, 168:74, 1986.

[74] O Nast. The aluminium-induced layer exchange formin polycrystalline silicon on glass for thin-film solar cells. *PhD Thesis, Marburg*, 2000.

[75] C Spinella, S Lombardo, and F Priolo. Crystal grain nucleation in amorphous silicon. *J. Appl. Phys.*, 84:5383, 1998.

[76] U Köster. *Phys. Stat. Sol.*, 48:313, 1978.

[77] T J Konno and R Sinclair. Structure and corrosion properties of fe/zr multilayers. *Phil. Mag. B*, 66:749, 1992.

[78] K N Tu. Selective growth of metal-rich silicide of near-noble metals. *Appl. Phys. Lett.*, 27:221, 1975.

[79] J C Inkson. The electron-electron interaction near an interface. *Surf. Sci.*, 28:69, 1971.

[80] V Heine. Theory of surface states. *Phys. Rev.*, 138:A1689, 1965.

[81] S G Louie and M L Cohen. Electronic structure of a metal-semiconductor interface. *Phys. Rev. B*, 13:2461, 1976.

[82] S B Zhang, M L Cohen, and S G Louie. Interface potential changes in schottky barriers. *Phys. Rev. B*, 32:3955, 1985.

[83] J Bardeen. Surface states and rectification at a metal semi-conductor contact. *Phy. Rev.*, 71:717, 1947.

[84] J Tersoff. Schottky barrier heights and the continuum of gap states. *Phys. Rev. Lett.*, 52:465–468, 1984.

[85] A Thanailakis and A Rasul. Transition-metal contacts to atomically clean silicon. *J. Phys. C*, 9:337, 1976.

[86] V Heine. Some theory about surface states. *Surf. Sci.*, 2:1–7, 1964.

[87] P E Batson. Silicon $p_{2,3}$ core absorption obtained at the buried al/si(111) interface. *Phys. Rev. B*, 44:5556, 1991.

[88] J Platen, B Selle, I Sieber, S Brehme, U Zeimer, and W Fuhs. Low-temperaure epitaxial growth of silicon by electron cyclotron resonance chemical vapor deposition. *Thin Sol. Films*, 381:22–30, 2001.

[89] S Gall, J Schneider, J Klein, M Muske, B Rau, E Conrad, I Sieber, W Fuhs, C Ornaghi, D Van Gestel, G Beacarne, J Poortmans, M Stöger-Pollach, P Schattschneider, J Bernardi, and O Van der Biest. Crystalline silicon thin-film solar cells on foreign substrates: the european project meteor. *EPVSEC Conference, Paris*, submitted, 2004.

[90] P Schattschneider and B Jouffrey. Localization and correlation of band transitions from electron energy loss spectrometry. *EPJ B*, accepted, 2003.

[91] M Avrami. Kinetics of phase change 1 (general theory). *J. Chem. Phys.*, 7:1103–1112, 1939.

[92] M Avrami. Kinetics of phase change 2 (transformation.time relation for random distribution of nuclei). *J. Chem. Phys.*, 8:212–224, 1940.

[93] M Avrami. Kinetics of phase change 3 (granulation, phase change, and microstructure). *J. Chem. Phys.*, 9:122–184, 1941.

[94] K Bryla, A Montgermont, M Stöger-Pollach, C Eisenmenger-Sittner, J Schneider, and S Gall. under construcion. *Thin Sol. Film.*, submitted, 2004.

[95] J O McCaldin and H Sankur. Diffusivity and solubility of si in the al metallization of integrated circuits. *Appl. Phsy. Lett.*, 19:524, 1971.

[96] G J van Gurp. Diffusion-limited si precipitation in evaporated al/si films. *J. Appl. Phys.*, 44:2040, 1973.

[97] B Rau, J Schneider, J Klein, M Muske, I Sieber, M Stöger-Pollach, P Schattschneider, and S Gall. Epitaxial growth of silicon by low temperature ecrcvd for si thin film solar cells on glass substrates. *HMI-Klausurtagung Jänner 2004*, Berlin, Germany, 2004.

[98] C Ornaghi, M Stöger, G Beaucarne, J Poortmans, and P Schattschneider. Thin film polycrystalline silcon solar cel on ceramics with a seeding layer formed via aluminium-induced crystallisation of amorphous silcon. *IEEE Proc.-Circuits Devices Styst.*, 150:287–292, 2003.

[99] B Rau, I Sieber, B Selle, S Brehme, U Knipper, S Gall, and W Fuhs. Homo.epitaxial si absorber layers grown by low-temperature ecrcvd. *Thin Solid Films*, 451-452:644–648, 2004.

Curriculum Vitae

Personal Data

Name:	Michael Stöger-Pollach
Born:	[redacted]
Nationality:	[redacted]
Martial Status:	[redacted]

Education

[redacted]

Studies

1992 - 1999	Physics Student at the Vienna University of Technology
Oct. 1996 - Feb. 1997	EARSMUS student at the Friedrich-Schiller Universtity of Jena, Germany
Oct. 1998 - May 1999	Diploma Thesis "*TEM and EELS microanalysis of polycristalline silicon thin films for solar cells*" by Prof. Peter Schattschneider, Institute of Solid State Physics [1]
1998, 1999	short time research stays at Ecole Centrale Paris, France
1999	short time research stay at Humboldt-Universtity of Berlin, Germany
June 1999	Final examination, academic title: "Diplom Ingenieur"
since Oct. 2000	PhD studies at Vienna University of Technology
2001	short time research stay at Ecole Centrale Paris, France
Feb. 2002 - Nov. 2002	Research Fellowship at Delft University of Technology at Prof. H.W. Zandbergen's Group
since July 2004	member of USTEM staff

Publications 1999-2004

Journals

1. *EELS microanalysis of pc-Si thin films for solar cells grown at low temperatures*
   M. Stöger, M. Nelhiebel, P. Schattschneider, V. Schlosser, A. Breymesser, B. Jouffrey
   Solar Energy Materials & Solar Cells 63 (2000) 177-184

2. *TEM and EELS microanalysis of pc-Si thin film solar cells deposited by means of HWCVD*
   M. Stöger, P. Schattschneider, V. Schlosser, R. Schneider, H. Kirmse, W. Neumann
   Solar Energy Materials & Solar Cells 70 (2001) 39-47

3. *Separation of pure elemental and oxygen influenced signal in ELNES*
   M. Stöger, P. Schattschneider, L.Y. Wei, B. Jouffrey, C. Eisenmenger-Sittner
   Ultramicroscopy 92 (2002) 285-292

4. *The separation of surface and bulk contributions in ELNES spectra*
   P. Schattschneider, M. Stöger, C. Hébert, B. Jouffrey
   Ultramicroscopy 93 (2002) 91-97

5. *Thin film polycrystalline silcon solar cel on ceramics with a seeding layer formed via aluminium-induced crystallisation of amorphous silcon*
   C. Ornaghi, M. Stöger, G. Beaucarne, J. Poortmans, P. Schattschneider
   IEEE Proc.-Circuits Devices Syst. 150 (2003) 287-292

6. *Direct measurements of the Si bandgap in EELS*
   M. Stöger-Pollach, C. Hébert, S. Rubino, P. Schattschneider, H.W. Zandbergen
   J.Phys.:Cond. Mat. accepted (2004)

7. *Direct observation of metal induced gap states with nm-resolution*
   M. Stöger-Pollach, P. Schattschneider
   Phys. Rev. B submitted (2004)

8. *Low-temperature Si epitaxy on large-grained polycrystalline seed layers by electron-cyclotron resonance chemical vapor deposition*
   B. Rau, I. Sieber, J. Schneider, M. Muske, M. Stöger-Pollach, P. Schattschneider, S. Gall, W. Fuhs
   submitted to: Journal of Crystal Growth

9. *Thickness dependent loss function of Si with 0.14 eV energy resolution*
   M. Stöger-Pollach, C. Hébert, P. Schattschneider, H.W. Zandbergen
   Advanced Engeneering Materials VCH Verlag Zürich 2004

Conference Proceedings and Book Contributions

1. *Investigation of impurity enrichment and electronic properties of microcrystalline silicon thin films*
   M. Stöger, P. Schattschneider, V. Schlosser, A. Breymesser
   IoP Conf. Ser. 169 (2001) 391-394

2. *ELNES Separation on Cr-$L_{2,3}$ Edges Influenced by Oxygen*
   M.Stöger, P.Schattschneider, H.W.Zandbergen
   Proc.15th Inernational Congress of Electron Microscopy pp. 851 - 852 **ISBN: 0-620-29294-6**

3. *Investigations of core level states in epitaxially grown Si layers by EELS*
   M. Stöger, E.C. Karl-Rückert, C. Hébert, B. Rau, H.W. Zandbergen, P. Schattschneider, S. Gall
   IoP Conf. Ser. 180 (2003)

4. *Investigations of bonding at an aluminium (III) oxide membrane in Si using ELNES separation*
   M. Stöger, J. Schneider, H.W. Zandbergen, P. Schattschneider, S. Gall
   IoP Conf. Ser. 180 (2003)

5. *Low-temperature epitaxial Si absorber layers grown by Electron-Cyclotron Resonance CVD*
   B.Rau, B.Selle, U.Knipper, S.Brehme, I.Sieber, M. Stöger, P. Schattschneider, S.Gall, W.Fuhs
   Proc. 3rd World Conf. on Photovolt. Energy Conversion,in Press

6. *The ELNES separation applied to oxidation states at interfaces*
   M. Stöger, P. Schattschneider, J. Schneider, S. Gall
   Conference Proceedings MCM6, Pula, Croatia pp.169-170

7. *Sub-eV core level shifts in grain boundaries and nanotwins*
   M. Stöger, C. Hébert, P. Schattschneider, H.W. Zandbergen, B. Rau, S. Gall
   Conference Proceedings MCM6, Pula, Croatia pp.171-172

8. *Unexplained thickness dependence in the Si loss function at 0.14 eV energy resolution*
   M. Stöger, P. Schattschneider, C. Hébert, H.W. Zandbergen
   Conference Proceedings MCM6, Pula, Croatia pp.400-401

9. *Epitaxial Si growth on polycrystalline Si seed layers at low teperature*
   B. Rau, J. Schneider, M. Muske, I. Sieber, S. Gall, M. Stöger-Pollach, P. Schattschneider, W. Fuhs
   Conf. Proc. 19th Europ. Photovolt. Solar Energy Conf., Paris, France

10. *Crystalline Si thin film solar cells on foreign substrates: the European project METEOR*
    S. Gall, J. Schneider, J. Klein, M. Muske, B. Rau, E. Conrad, I. Sieber, W. Fuhs, C. Ornaghi, D. Van Gestel, I. Gordon, K. Van Nieuwenhysen, G. Beaucarne, J. Poortmans, M. Stöger-Pollach, J. Bernardi, P. Schattschneider
    Conf. Proc. 19th Europ. Photovolt. Solar Energy Conf., Paris, France

11. *Aluminum-induced crystallization of Silicon on high temperature substrates for thin-film silicon solar cells*

G. Beaucarne, D. Van Gestel, I. Gordon, L. Carnel, C. Ornaghi, K. Van Nieuwenhysen, J. Poortmans, M. Stöger-Pollach, P. Schattschneider
Conf. Proc. 19th Europ. Photovolt. Solar Energy Conf., Paris, France

Oral Presentations

1. *Investigation of impurity enrichment and electronic properties of microcrystalline silicon thin films*
   M. Stöger, P. Schattschneider, V. Schlosser, A. Breymesser
   Microscopy of Semiconducting Materials XII 25-29 March 2001, Oxford, UK

2. *ELNES of surface oxidized thin films*
   M. Stöger
   *PICS Meeting, Vienna University of Technology*28 - 29 June 2001, Vienna, Austria

3. *ELNES separation - an introduction*
   M. Stöger
   Seminar on EELS, Delft University of Technology 18th July 2001, Delft, The Netherlands

4. *ELNES separation on surfaces and interfaces*
   M. Stöger
   Seminar on EELS, Delft University of Technology 19th November 2002, Delft, The Netherlands

5. *Study of metal-induced crystalisation*
   M. Stöger, P. Schattschneider, J. Bernardi
   METEOR-Meeting, Vienna University of Technology, 9-10 January 2003, Vienna, Austria

6. *Study of epitaxial deposition*
   M. Stöger, P. Schattschneider, J. Bernardi
   METEOR-Meeting, Vienna University of Technology, 9-10 January 2003, Vienna, Austria

7. *Investigations of bonding at an aluminium (III) oxide membrane in Si using ELNES separation*
   M. Stöger, J. Schneider, H.W. Zandbergen, P. Schattschneider, S. Gall
   Microscopy of Semiconducting Materials XIII 31st March - 3rd April 2003, Cambridge, UK

8. *The ELNES separation applied to oxidation states at interfaces*
   M. Stöger, P. Schattschneider, J. Schneider, S. Gall
   6^{th} *Multinational Congress on Microscopy* 1st-5th June 2003, Pula, Croatia

9. *Sub-eV core level shifts in grain boundaries and nanotwins*
   M. Stöger, C. Hébert, P. Schattschneider, H.W. Zandbergen, B. Rau, S. Gall
   6^{th} *Multinational Congress on Microscopy* 1st-5th June 2003, Pula, Croatia

10. *TEM investigations of EPI and MIC specimens*
    M. Stöger-Pollach, P. Schattschneider, J. Bernardi
    METEOR-Meeting, IMEC Leuven, 26-27 June 2003, Leuven, Belguim

11. *The layer exchange process: first clues*
M. Stöger-Pollach, E.C. Karl-Rückert, P. Schattschneider, J. Bernardi
METEOR-Meeting, IMEC Leuven, 26-27 June 2003, Leuven, Belguim

12. *EELS at novel Si thin film solar cells*
M. Stöger-Pollach
Seminar of the Institute of Solid State Physics, Vienna University of Technology, 15 October 2003, Vienna, Austria

13. *TEM studies of epitaxial growth*
M. Stöger-Pollach, P. Schattschneider
METEOR-Meeting, HMI Berlin, 8-9 January 2004, Berlin, Germany

14. *Influences on the ALILE process*
M. Stöger-Pollach, P. Schattschneider
METEOR-Meeting, HMI Berlin, 8-9 January 2004, Berlin, Germany

15. *Epitaxy - Reasons for success and failure*
M. Stöger-Pollach
METEOR Workshop on Low-Temperature Epitaxy, 30 March 2004, Berlin, Germany

16. *Insights into the ALILE process*
M. Stöger-Pollach
METEOR Workshop on Aluminium Induced Layer Exchange, 31 March 2004, Berlin, Germany

17. *Charactarisation methods in the TEM (+SIMS)*
M. Stöger-Pollach
METEOR Workshop on Aluminium Induced Layer Exchange, 31 March 2004, Berlin, Germany

18. *Crystalline Si thin film solar cells on foreign substrates: the European project METEOR*
S. Gall, J. Schneider, J. Klein, M. Muske, B. Rau, E. Conrad, I. Sieber, W. Fuhs, C. Ornaghi, D. Van Gestel, I. Gordon, K. Van Nieuwenhysen, G. Beaucarne, J. Poortmans, M. Stöger-Pollach, J. Bernardi, P. Schattschneider
19th European Photovoltaic Solar Energy Conference, 7-11 June 2004, Paris, France

19. *Aluminum-induced crystallization of Silicon on high temperature substrates for thin-film silicon solar cells*
G. Beaucarne, D. Van Gestel, I. Gordon, L. Carnel, C. Ornaghi, K. Van Nieuwenhysen, J. Poortmans, M. Stöger-Pollach, P. Schattschneider
19th European Photovoltaic Solar Energy Conference, 7-11 June 2004, Paris, France

20. *Influences on the ALILE process*
M. Stöger-Pollach, P. Schattschneider
METEOR-Meeting, TU Vienna, 24-25 June 2004

21. *Defects in epitaxially growth thin films*
M. Stöger-Pollach, P. Schattschneider, K. Mayerhofer
METEOR-Meeting, TU Vienna, 24-25 June 2004

Poster Presentations

1. *Untersuchungen an mittels Hot Wire CVD Verfahren hergestellten Solar-Silizium Schichten*
   M. Ramadori, V. Schlosser, A. Breymesser, M.Stöger, P. Schattschneider, D. Peiro, C. Voz, J. Bertomeu, J. Andreu, B. Jouffrey
   Frühjahrestagung der Deutschen Physikalischen Gesellschaft, 22-26 March 1999, Münster, Germany

2. *TEM- und EELS- Mikroanalyse von mittels Hot Wire CVD hergestellten polycristallinen Siliziumsolarzellen*
   M. Stöger, M. Nelhiebel, P. Schattschneider, V. Schlosser, R. Schneider, H. Kirmse, W. Neumann
   Jahrestagung der Österreichischen Physikalischen Gesellschaft, Innsbruck, 1999

3. *Analyse par MET et EELS de cellules solaires en silicium polycristallin obtenues par HW-CVD*
   M. Stöger, M. Nelhiebel, C. Hébert, P. Schattschneider, V. Schlosser, R. Schneider, H. Kirmse, W. Neumann
   JEELS 99, 17-20 October 1999, Autrans, France

4. *Investigations on microstructure and microchemistry of polycrystalline silicon materials for solar cells*
   M. Stöger, P. Schattschneider, V. Schlosser, R. Schneider, H. Kirmse, W. Neumann
   16th European Photovoltaic Solar Energy Conference and Exhibition, May 2000, Glasgow, UK

5. *Can the electron microscope replace a synchrotron?*
   M. Stöger, C. Hébert, L.M. Brown, P.Schattschneider, M. Willinger, B. Jouffrey
   16th International Conference on X-ray Optics and Microanalysis, 2 - 6 July 2001, Vienna, Autria

6. *Separation of surface and bulk signals in the ELNES of oxidized materials*
   M. Stöger, C. Hébert, P. Schattschneider, B. Jouffrey, G. Hug, C. Eisenmenger-Sittner
   Dreiländertg. für Elektronenmikroskopie, 9 - 14 September 2001, Innsbruck, Austria

7. *Improvement of bulk-surface ELNES separation by use of a monochromator*
   M. Stöger, H.W. Zandbergen, C. Hébert, P. Schattschneider
   SALSA 2002, 5-9 May 2002, Guadelupe, French West Indies

8. *ELNES separation on Cr $L_{2,3}$-edges influenced by oxygen*
   M. Stöger, H.W. Zandbergen, P. Schattschneider
   ICEM 15, 2-6 September 2002, Durban, South Africa

9. *Investigations of core level states in epitaxially grown Si layers by EELS*
   M. Stöger, E.C. Karl-Rückert, C. Hébert, B. Rau, H.W. Zandbergen, P. Schattschneider, S. Gall
   Microscopy of Semiconducting Materials XIII, 31st March - 3rd April 2003, Churchill College, Cambridge, UK

10. *Low-temperature epitaxial Si absorber layers grown by Electron-Cyclotron Resonance CVD*
    B. Rau, B. Selle, U. Knipper, S. Brehme, I. Sieber, M. Stöger, P. Schattschneider, S. Gall, W. Fuhs
    3rd World Conference on Photovoltaic Energy Conversion, 11-18 May 2003, Osaka, Japan

11. *Unexplained thickness dependence in the Si loss function at 0.14 eV energy resolution*
M. Stöger, P. Schattschneider, C. Hébert, H.W. Zandbergen
6th Multinational Congress on Microscopy, 1st-5th June 2003, Pula, Croatia

12. *ELNES separation: a method to improve the detection limit of oxides at interfaces*
M. Stöger-Pollach, P. Schattschneider, C. Ornaghi
EUROMAT 2003, 1-5 September 2003, Lausanne, Switzerland

13. *Epitaxial Growth of Silicon by Low-Temperature ECRCVD for Si Thin Film Solar Cells on Glass Substrates*
B. Rau, J. Schneider, J. Klein, M. Muske, I. Sieber, M. Stöger-Pollach, P. Schattschneider, S. Gall
HMI Klausurtagung, 19-21.1.2004, Templin, Germany

14. *Metal induced gap states at a c-Si/Al Schottky barrier*
M. Stöger-Pollach, P. Schattschneider
European Microscopy Conference EMC 2004,22-27 August 2004, Antwerp, Belgium

15. *Epitaxial Si growth on polycrystalline Si seed layers at low teperature*
B. Rau, J. Schneider, M. Muske, I. Sieber, S. Gall, M. Stöger-Pollach, P. Schattschneider, W. Fuhs
19th European Photovoltaic Solar Energy Conference, 7-11 June 2004, Paris, France

16. *Adhesion Promotion of Copper-Coatins to Carbon Surfaces by Plasma Treatment and Molybdinum Interlayers*
B. Schwarz, C. Schrank, C. Eisenmenger-Sittner, M. Stöger-Pollach, M. Rosner, E. Neubauer
16th International Vacuum Congress IVC16, 28 June - 2 July 2004, Venecia, Italy

Diploma Thesis

1. *TEM and EELS microanalysis of polycristalline silicon thin films for solar cells*
M. Stöger
Vienna University of Technology 1999